Detection of the First Observed Outburst of DW Cancri

Photometric light curve from all AAVSO *V* filter observations of DW Cnc between 2006 December 24 and 2007 February 04.

Also in this issue...

- Discovery and Observations of the Optical Afterglow of GRB 071010B

- On the Connection Between CWA and RVA Stars

- Studying Variable Stars Discovered Through Exoplanet-Transit Surveys

Complete table of contents inside...

JAAVSO

The Journal of
The American Association
of Variable Star Observers

Page Charges

Unsolicited papers by non-Members will be assessed a charge of $15 per page.

Instructions for Submissions

The *Journal* welcomes papers from all persons concerned with the study of variable stars and topics specifically related to variability. All manuscripts should be written in a style designed to provide clear expositions of the topic. Contributors are strongly encouraged to submit digitized text in LATEX+POSTSCRIPT, MS WORD, or plain-text format. Manuscripts may be mailed electronically to journal@aavso.org or submitted by postal mail to *JAAVSO*, 49 Bay State Road, Cambridge, MA 02138, USA.

Manuscripts must be submitted according to the following guidelines, or they will be returned to the author for correction:

Manuscripts must be:
1) original, unpublished material;
2) written in English;
3) accompanied by an abstract of no more than 100 words.
4) not more than 2,500-3,000 words in length (10–12 pages double-spaced).

Figures for publication must:
1) be camera-ready or in a high-contrast, high-resolution, standard digitized image format;
2) have all coordinates labeled with division marks on all four sides;
3) be accompanied by a caption that clearly explains all symbols and significance, so that the reader can understand the figure without reference to the text.

Maximum published figure space is 4.5" by 7". When submitting original figures, be sure to allow for reduction in size by making all symbols and letters sufficiently large.

Photographs and halftone images will be considered for publication if they directly illustrate the text.

Tables should be:
1) provided separate from the main body of the text;
2) numbered sequentially and referred to by Arabic number in the text, e.g., Table 1.

References:
1) References should relate directly to the text.
2) References should be keyed into the text with the author's last name and the year of publication, e.g., (Smith 1974; Jones 1974) or Smith (1974) and Jones (1974).
3) In the case of three or more joint authors, the text reference should be written as follows: (Smith *et al.* 1976).
4) All references must be listed at the end of the text in alphabetical order by the author's last name and the year of publication, according to the following format:
Brown, J., and Green, E. B. 1974, *Astrophys. J.*, **200**, 765.
Thomas, K. 1982, *Phys. Report*, **33**, 96.
5) Abbreviations used in references should be based on recent issues of the Journal or the listing provided at the beginning of *Astronomy and Astrophysics Abstracts* (Springer-Verlag).

Miscellaneous:
1) Equations should be written on a separate line and given a sequential Arabic number in parentheses near the right-hand margin. Equations should be referred to in the text as, e.g., equation (1).
2) Magnitude will be assumed to be visual unless otherwise specified.
3) Manuscripts may be submitted to referees for review without obligation of publication.

Journal of the American Association of Variable Star Observers
Volume 36, Number 1, 2008

Period Change in the Semiregular Variable RU Vulpeculae

Matthew Templeton
AAVSO, 49 Bay State Road, Cambridge, MA 02138

Lee Anne Willson
Department of Physics and Astronomy, Iowa State University, Ames, IA 50014

Grant Foster
Island Data Corporation, 2386 Faraday Ave., Suite 280, Carlsbad, CA 92008
and
AAVSO, 49 Bay State Road, Cambridge, MA 02138

Abstract   The well-observed semiregular variable RU Vulpeculae has undergone a substantial change in period over the past fifty-five years. The discovery period of ~155 days has undergone a continuous change to its current value of 108 days. The amplitude and stability of the light curve have changed as well; the pulsations are much less regular and have a lower amplitude now than at the time of RU Vul's discovery and classification. The character of the period change is quantitatively similar to that of the well-studied Mira variable T Ursae Minoris, and we argue that RU Vul may be a semiregular analog of Mira variables undergoing dramatic period changes. We place RU Vul in the context of other AGB stars exhibiting similar behavior, and discuss possible explanations for its period change.

1. Introduction

The Templeton *et al.* (2005) study of 547 well-observed Mira variables found that about 1.5 percent of Mira stars exhibit large, easily detectable changes in pulsation period. One possible explanation for these changes is that they are due to *thermal pulses*, which are rapid, helium-shell burning events predicted to occur in asymptotic giant branch (AGB) stars. These pulses and their aftereffects last for a few thousand years, and their occurrence is confirmed observationally by the presence of the short-lived isotope technetium in the spectra of many AGB stars. The energy generated in these pulses would act to change the equilibrium structure of the star, resulting in a substantial change in pulsation period detectable on observable timescales. The fraction of stars with large period changes is consistent with the ratio of the durations of thermal pulses (around 10^3 y) to the time between pulses (around 10^5 y) predicted by stellar evolution models. However, it is unclear whether thermal pulses are responsible for any or all of the observed cases of period changes in Miras,

and whether such changes are potentially observable in all pulsating AGB stars, including the semiregular variables.

Formally, the Mira and semiregular variables differ in amplitude (Miras have amplitudes above 2.5 magnitudes by definition; semiregulars, below 2.5) and period (Miras have periods above 100 days; semiregulars can have a range of periods up to and beyond 100 days). However, there is substantial overlap between the two classes, with some Miras exhibiting striking irregularities, and some semiregulars appearing quite regular in comparison to others in the same class. Wood *et al.* (1999) showed that the LMC Miras and semiregulars are concentrated on separate parallel tracks on the period-luminosity diagram; this implies that they are physically similar objects pulsating in different radial modes. The fact that some semiregular stars lie on the period-luminosity relation for Mira variables in the solar neighborhood (Bedding and Zijlstra 1998) suggests some overlap between the two. This and other observational information point to Miras as fundamental mode pulsators, while the semiregulars are predominantly overtone pulsators with a few being fundamental mode pulsators. Whether there is an evolutionary progression from one to the other isn't clear, but it is a reasonable assumption that as stars slowly increase in luminosity, progressively lower-order modes become excited, until they become Miras pulsating in the fundamental mode (see Marigo and Girardi 2007). One major difference between Miras and semiregulars is known to be the mechanism of driving. Christensen-Dalsgaard *et al.* (2001) and Bedding *et al.* (2005) showed that there are spectral signatures of stochastic behavior in the semiregular stars, whereas Miras are comparatively more stable. Recent work by Kiss *et al.* (2006) on the supergiant semiregulars shows similar behavior, along with the presence of low-frequency *red noise*—another signature of stochastic behavior. Many semiregular stars are known to be multiperiodic, with more than one pulsation mode excited at a given time. This could explain the irregularity observed in some but not all of these objects. Semiregulars in general appear to be less chemically evolved than Miras. Lebzelter and Hron (2003) found that most semiregulars lack Technetium, but many Mira stars also lack Technetium.

It is a given that as a star moves through the AGB instability strip, pulsation modes will become excited or damped, and pulsations may become regular or irregular. Miras themselves show significant cycle-to-cycle variations, and the semiregular phenomenon may simply be an extreme example of this behavior. Or, conversely, the Miras (or fundamental mode pulsators generally) may be driven to such high limiting amplitudes that they overcome the instability inherent in the semiregular variables of higher overtone. Individual stars may transition from one type to the other during their AGB lifetimes, and such transitions may be especially rapid during thermal pulses.

RU Vul (AAVSO 2034+22A, HIP 101888; R.A. $20^h 30^m 52.69^s$, Dec. $+23°$ 15' 31.2", J2000) is an M3e oxygen-rich semiregular variable. Its distance (and hence absolute magnitude) is unknown (Perryman *et al.* 1997), but RU Vul is believed to be a part of the thick disk population of the Milky Way

(Mennessier *et al.* 2001). The changing period of RU Vul has been known for some time, and four different period epochs are noted in the *General Catalogue of Variable Stars* (GCVS) fourth edition (Kholopov *et al.* 1985). Percy and Au (1999) described these variations in terms of a linear period change, while Kiss *et al.* (1999) explained them with multiperiodicity. Later, Zijlstra and Bedding (2002) used a time-frequency analysis to show that the period variation is best described in terms of a *continuous period change*, from about 155 days at the time of its discovery to about 108 days currently.

In this paper, we analyze the most current available data to quantify the rate of period change, and attempt to place RU Vul in context of the Mira variables exhibiting similar behavior.

2. Data and results

We used the 6,230 visual observations of RU Vul taken from the AAVSO International Database, spanning JD 2427820.6–2454312.6 (1935 January 18–2007 July 31). These data were averaged into ten-day wide bins, yielding 1,788 averaged data points (Figure 1). These were then analyzed for time evolution of the pulsation period using the *weighted wavelet Z-transform WWZ* (wwz) developed by Foster (1996). The wwz algorithm is analogous to a discrete Fourier transform using a Gaussian weighting function for the data. The time center and width of the Gaussian window are adjustable, and may be moved along a given set of data to measure the time evolution of the variability. We used the procedure outlined in Templeton *et al.* (2005) to measure the time-frequency behavior of RU Vul. The dominant signal's period, amplitude, and mean magnitude as functions of time are shown in Figure 2.

The period of RU Vul has clearly changed over the course of recorded observations, as have the amplitude (also clearly seen in the light curve in Figure 1) and the mean magnitude. To determine the rate of period change dP/dt, we fit a line through the time-period measurements between JD 2435000 and 2454000, and obtained a rate of period change of -2.5×10^{-3} d/d (= -0.91 d/y) from the slope of the line. For comparison with the Mira stars given in Templeton *et al.* (2005), this rate of period change yields a fractional rate of period change $d\ln P/dt = -7.11 \times 10^{-3}$ y^{-1}. This is the second-largest fractional period change among all of the AGB stars with known period changes, with only that of T UMi being larger, at -8.4×10^{-3} y^{-1}. For most Mira variables it is below 10^{-5} y^{-1}. This rate of change is consistent with those predicted by stellar evolution calculations (Wood and Zarro 1981; Vassiliadis and Wood 1993).

The changes in amplitude and mean magnitude are apparent both in the light curve itself and in the time-frequency analysis. The amplitude declines throughout the light curve, but is marked by an abrupt drop around JD 2439000 (late 1965); likewise the mean magnitude shows a weak brightening trend, marked by an abrupt increase of 0.6 magnitude (nearly seventy-five percent

in luminosity) at the same time. The changes in amplitude and mean light seem to occur because the minima suddenly become brighter (by over one magnitude). The brightness of the maxima have changed very little over the recorded history of RU Vul, but the very sudden brightening of the minima is remarkable. Curiously, these changes occur not at the start of the period decline (circa JD 2435000) but several thousand days later.

Finally, we note the detection of a secondary pulsation mode in the spectrum of RU Vul. There is a long-term oscillation in mean light apparent in the light curve, and when we analyze the light curve with a *clean*-based Fourier transform (Roberts *et al.* 1987), we find a second strong period at approximately 2,450 days. The period is too long to measure reliably whether it, too, is changing, but it does produce peaks at integer multiples of the main period in an autocorrelation diagram, and is also apparent as a modulation in the maxima and minima throughout the light curve. It is not as apparent to the eye in the light curve over the past 5,000 days.

3. Discussion

RU Vulpeculae is clearly an object in transition. The period change is dramatic; it has declined by thirty percent over the past fifty-five years, and only the Mira stars T UMi, LX Cyg, and BH Cru have rates of period change of similar magnitude. Like T UMi, RU Vul appears to have begun its dramatic changes as we have watched.

Both the GCVS and the earliest AAVSO observations indicate that the period remained constant between 1935 and the 1950s, when it began to steadily decline. If we can extrapolate the evolution calculations of thermally pulsing Mira-like stars to the semiregulars, the pre-decline constancy of period and the subsequent rate of period decline are like what is predicted for the onset of a thermal pulse. RU Vul may therefore be the second example of an AGB star initiating a thermal pulse during the history of recorded observations, after T UMi.

The similarity of RU Vul's period history to the pulsation periods predicted from thermally pulsing models is striking, but it is by no means proven that thermal pulses are responsible for the large period declines observed in this star or any other AGB pulsator. The fact that the mean magnitude has undergone a slight *increase* throughout the observational record— contrary to the model prediction of decreasing luminosity—may be important evidence against a thermal pulse. Both the evolutionary tracks of Vassiliadis and Wood (1993) and the period-luminosity relations for Miras and semiregulars in the solar neighborhood (Bedding and Zijlstra 1998) predict decreases of nearly half a magnitude when the period changes by the amount observed, for both fundamental and first overtone pulsation modes. The increase observed (nearly a magnitude) is too large to be due to an increase in effective temperature, since it would require an unphysically large change in (B–V) (see Stanton 1981 for the transformation equation from V to visual). The picture is further

complicated by RU Vul being a semiregular variable, which are by definition unstable, and for which the cause of instability is unknown. Although the light curve is modulated by the long secondary period of 2,450 days, it would not account for the long-term trend in mean magnitude. Such a trend would require a period far longer than the time span of the light curve itself. Proposed non-evolutionary mechanisms for global changes in AGB stars include feedback between the pulsations and the stellar structure (e.g., Ya'ari and Tuchman 1996; Lebzelter and Wood 2005) and secular changes in the opacity (e.g., Zijlstra *et al.* 2004) resulting in global changes to the equilibrium structure. Several pulsating AGB stars have also been observed to undergo substantial changes in pulsation amplitude with only slight changes in period, such as Y Per (Kiss *et al.* 2000), W Tau, and RT Hya (Mattei *et al.* 1990). Templeton *et al.* (2005) showed in a purely statistical sense that the number of AGB pulsators with measurable period changes (about one to two percent) is consistent with the relative times that Mira variables spend in the thermally pulsing and interpulse stages of the AGB, but unfortunately we can say nothing about whether an *individual* star is itself undergoing a thermal pulse. However, we are much less likely to observe a star during the *onset* of a thermal pulse during the course of a century's observations. The probability of any given AGB star undergoing this process is about 0.1 percent, or one in 1,000; again it is simply the duration of the rapid period change (about a century) relative to the total interpulse lifetime (of order 10^5 y). If we assume that both T UMi and RU Vul were caught at this stage, and if we assume that there are about 500 well-observed AGB stars among the variables in the AAVSO archives, then more objects than are expected are undergoing this behavior. We are limited by the small sample size at hand, but it does suggest that there may be another explanation for this behavior besides thermal pulses. As a further caveat, we note the existence of yet another evolved star, V725 Sgr, which has also undergone a large period change (Percy *et al.* 2006), and has transformed from Cepheid to semiregular over the past century. The cause of this transformation is also unknown, although Percy *et al.* (2006) speculate that V725 Sgr is in the middle of a blue loop through the Cepheid instability strip, and has moved back to the giant branch.

The theoretical picture of pulsations in AGB stars is far more complicated than what is seen in other pulsators, due in part to the critical importance of convection, complex chemistry and dust formation, the extremely high amplitudes, and the role of mass loss. Theoretical modeling involving many of these considerations is ongoing, and will reveal much about the physical behavior and evolution of these stars. A crucial question to answer will be how exactly do pulsations modify the physical properties of the star? One suggestion by Ya'ari and Tuchman (1996) and Lebzelter and Wood (2005) is that the star must undergo some relaxation process while it is pulsating, but it is not clear why such a process would start spontaneously when a star is already pulsating at a reasonable limiting amplitude, as both RU Vul and T UMi were doing prior to the onset of period changes.

Future long-term monitoring of both RU Vul and T UMi will also be key to understanding these stars. If both stars are moving through the AGB instability strip, then we may see them change pulsation mode or cease pulsating altogether in the future. It will be particularly interesting to monitor the behavior of these objects in coming decades, as T UMi is approaching the canonical lower amplitude limit for classification as a Mira star, and the variations of RU Vul appear to be vanishing altogether. Both objects are fascinating examples of stars evolving before our eyes, and warrant our attention in the future. We encourage observers—visual and instrumental—to begin and continue monitoring these fascinating objects in the coming decades.

4. Acknowledgements

References

Bedding, T. R., Kiss, L. L., Kjeldsen, H., Brewer, B. J., Dind, Z. E., Kawaler, S. D., and Zijlstra, A. A. 2005, *Mon. Not. Roy. Astron. Soc.*, **361**, 1375.
Bedding, T. R., and Zijlstra, A.A. 1998, *Astrophys. J., Lett. Ed.*, **506**, L47.
Christensen-Dalsgaard, J., Kjeldsen, H., and Mattei, J. A. 2001, *Astrophys. J.*, **562**, L141.
Foster, G. 1996, *Astron. J.*, **112**, 1709.
Kholopov, P. N., *et al.* 1985, *General Catalogue of Variable Stars*, 4th ed., Moscow.
Kiss, L. L., Szabó, G. M., and Bedding, T. R. 2006, *Mon. Not. Roy. Astron. Soc.*, **372**, 1721.
Kiss, L. L., Szatmáry, K., Cadmus, R. R., Jr., and Mattei, J. A. 1999, *Astron. Astrophys.*, **346**, 542.
Kiss, L. L., Szatmáry, K., Szabó, G., and Mattei, J. A. 2000, *Astron. Astrophys., Suppl. Ser.*, **145**, 283.
Lebzelter, T., and Hron, J. 2003, *Astron. Astrophys.*, **411**, 533.
Lebzelter, T., and Wood, P. R. 2005, *Astron. Astrophys.*, **441**, 1117.
Marigo, P., and Gararardi, L. 2007, *Astron. Astrophys.*, **469**, 239.
Mattei, J. A., Mayall, M. W., and Waagen, E. O. 1990, *Maxima and Minima of Long Period Variables, 1949–1975*, AAVSO, Cambridge, MA.
Mennessier, M. O., Mowlavi, N., Alvarez, R., and Luri, X. 2001, *Astron. Astrophys.*, **374**, 968.

Percy, J. R., and Au, W. -Y. 1999, *Publ. Astron. Soc. Pacific*, **111**, 98.

Percy, J. R., Molak, A., Lund, H., Overbeek, D., Wehlau, A. F., and Williams, P. F. 2006, *Publ. Astron. Soc. Pacific*, **118**, 805.

Perryman, M. A. C., *et al.* 1997, *Astron. Astrophys.*, **323**, L49.

Roberts, D. H., Lehar, J., and Dreher, J. W. 1987, *Astron. J.*, **93**, 968.

Stanton, R. H. 1981, *J. Amer. Assoc. Var. Star Obs.*, **10**, 1.

Templeton, M. R., Mattei, J. A., and Willson, L.A. 2005, *Astron. J.*, **130**, 776.

Vassiliadis, E., and Wood, P. R. 1993, *Astrophys. J.*, **413**, 641.

Wood, P. R., and Zarro, D. M. 1981, *Astrophys. J.*, **247**, 247.

Wood, P. R., *et al.* 1999, in *Asymptotic Giant Branch Stars*, IAU Symposium 191, eds. T. Le Bertre, A. Lebre, and C. Waelkens, Astron. Soc. Pacific, San Francisco, 151.

Ya'ari, A., and Tuchman, Y. 1996, *Astrophys. J.*, **456**, 350.

Zijlstra, A. A., and Bedding, T. R. 2002, *J. Amer. Assoc. Var. Star Obs.*, **31**, 2.

Zijlstra, A. A., *et al.* 2004, *Mon. Not. Roy. Astron. Soc.*, **352**, 325.
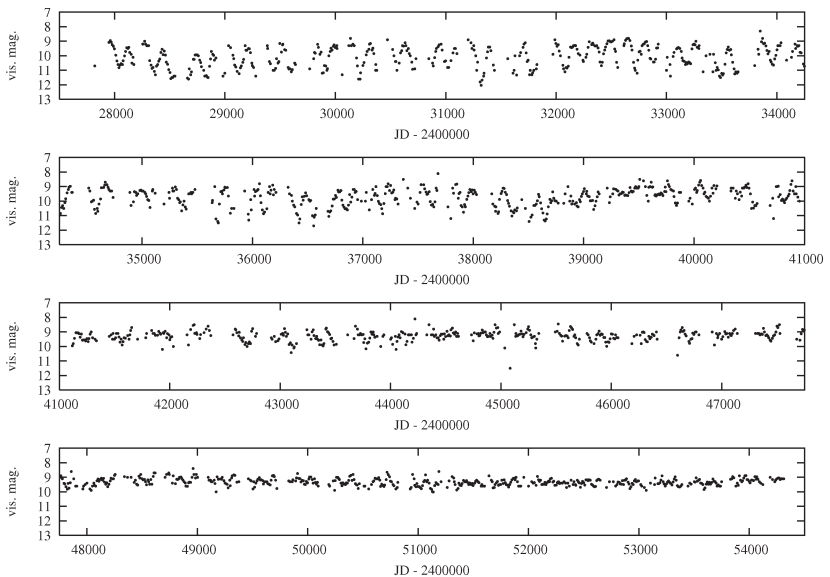
Figure 1. The visual light curve of RU Vul from the AAVSO International Database (January 1935–July 2007). Data points are 10-day means of visual magnitude estimates.
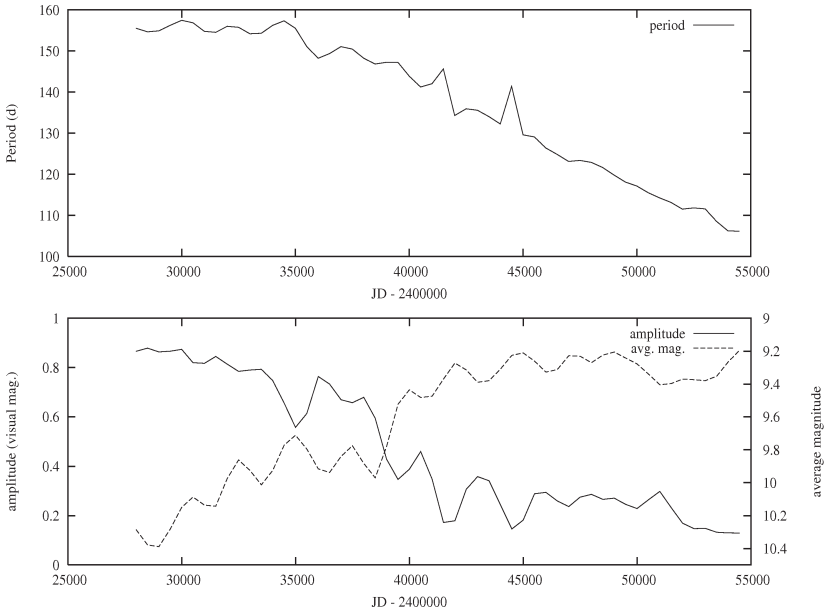
Figure 2. The period (top panel), amplitude (bottom panel, solid line), and mean magnitude (bottom, dashed) for RU Vul as calculated using the WWZ (Foster 1996) time-frequency algorithm. The period has dropped dramatically since JD 2435000, declining continuously from about 155 days earlier this century to the current value of less than 110 days.

How to Understand the Light Curves of Symbiotic Stars

Augustin Skopal

Astronomical Institute, Slovak Academy of Sciences, SK-059 60 Tatranska Lomnica, Slovakia

Abstract   I introduce fundamental types of variations observed in the light curves of symbiotic stars: the orbitally-related wave-like modulation during quiescent phases, eclipses during active phases, and apparent orbital changes indicated during transitions between quiescence and activity. I explain their nature with the aid of the spectral energy distribution of the composite spectrum of symbiotic stars and their simple ionization model.

1. Introduction

The symbiotic stars are understood as interacting binary systems comprising a late-type giant and a hot compact star—most probably a white dwarf. Their orbital periods run usually between one and three years, but can be significantly larger.

Mass loss from the giant represents the primary condition for appearance of the symbiotic phenomenon. A part of the material lost by the giant is transferred to the compact companion via accretion from the stellar wind. This process makes the accretor very hot ($T_h \sim 10^5$ K) and luminous ($L_h \sim 10–10^4$ $L_\odot$), and thus capable of ionizing a fraction of the neutral wind from the giant, giving rise to nebular emission. As a result, the spectrum of symbiotic stars consists of three basic components of radiation—two stellar (from the binary components) and one nebular, emitting by the ionized winds of both the stars.

If the processes of mass-loss, accretion, and ionization are in a mutual equilibrium, then the symbiotic system releases its energy approximately at a constant rate and spectral energy distribution (SED). This stage is known as the *quiescent phase*. Once this equilibrium is disturbed, the symbiotic system changes its radiation significantly, at least in its SED, which leads to a brightening in the optical by a few magnitudes. We call this the *active phase*.

The presence of physically different sources of radiation in the system which differ extremely in temperatures, and also their nature (stellar and nebular component), produce a complex composite spectrum. The resulting spectrum thus depends on the wavelength, the activity of the system, and also the projection of these regions into the line of sight, i.e., on the orbital phase of the binary. In addition, the composite spectrum of individual objects is also a function of their physical and orbital parameters.

Throughout the optical, the light contributions from these sources rival each other, producing a spectrum whose color indices differ significantly from those of standard stars.

Therefore the light curves (LCs) of symbiotic stars have a complex profile, often having an unexpected variation. Generally, the most pronounced changes are observed at the short-wavelength domain of the visual region—namely, within the photometric *U* filter. In this passband the dominant light contribution usually comes from the nebula, which responds most sensitively to the variation of the energy production of the symbiotic system. The large variety of changes recorded in the LCs of symbiotic stars is very broad, and many variations are not quite understood yet. It is, however, clear that they are related to those observed from X-rays to radio wavelengths. From this point of view, photometric monitoring is important to complement other multifrequency observations and thus to help in understanding the responsible physical processes. This aspect was recently highlighted by Sokoloski (2003) and demonstrated for the case of the symbiotic prototype Z And by Sokoloski *et al.* (2006).

In this contribution I discuss just the fundamental types of variations in the LCs of symbiotic stars that reflect most closely their nature—the orbitally-related wave-like variation, eclipses, and apparent changes of the orbital period. To understand these types of variability, I compare the multicolor LCs with the disentangled composite spectrum in the visual domain and consider the basic ionization structure of symbiotic stars. First, I introduce some examples of their LCs.

2. Examples of light curves of well studied symbiotic binaries

2.1. Z Andromedae

Z And is considered a prototype of the class of symbiotic stars. The binary comprises a late-type, M4.5 III giant and a white dwarf accreting from the giant's wind on the 758-day orbit (Nussbaumer and Vogel 1989). More than one hundred years of monitoring Z And has shown the eruptive character of its LC. It displays several active phases, during which fluctuations range in amplitude from a few tenths of a magnitude to about three magnitudes (Formiggini and Leibowitz 1994). Figure 1 (top panel) displays its recent activity from 2000 autumn covering the optical maxima in 2000 December, 2004 September, and 2006 July.

2.2. BF Cygni

BF Cyg is an eclipsing symbiotic binary with an orbital period of 757.2 days (Fekel *et al.* 2001). The system consists of a late-type cool component classified as a normal M5 III giant (Mürset and Schmid 1999) and a hot, luminous compact object (Mikołajewska *et al.* 1989). Its historical LC shows three basic types of active phases—nova-like and Z And type of outburst and short-term flares (Skopal *et al.* 1997). Figure 2 (top panel) shows its LC from 1985 covering the recent 1989 outburst with an eclipse effect and wave-like variation during the following quiescent phase.

2.3 CI Cygni

CI Cyg is also an eclipsing symbiotic binary with an orbital period of 855.25 days (Belyakina 1979; Belyakina 1984). Its cool component was recently classified as a M5.5 III giant (Mürset and Schmid 1999). A detailed study of this system was made by Kenyon *et al.* (1991). The last major active phase of CI Cyg began in 1975 (Belyakina 1976). During the first four cycles from the maximum, narrow minima indicating eclipses developed in the LC, a typical feature of active phases of symbiotic stars having a high orbital inclination. From 1985 the minima profile became very broad indicating a quiescent phase (Figure 1, mid panel). From 2006 May, CI Cyg entered its new active phase (Skopal *et al.* 2007).

2.4. V1329 Cygni

The symbiotic phenomenon of V1329 Cyg developed during its nova-like eruption in 1964. Prior to this outburst, V1329 Cyg was an inactive star of about 15th magnitude displaying ~2 magnitude-deep eclipses (see Figure 1 in Munari *et al.* (1988)). The post-outburst LC shows large, ~1.5 magnitude deep, periodic, wave-like variations connected with the binary motion. The IUE observations revealed the presence of a strong nebulosity in the near-UV spectrum (Figure 3).

2.5. AG Draconis

This symbiotic system belongs to the group of so-called yellow symbiotics, because it contains a K2 III giant as a cool component (Mürset and Schmid 1999). There are no signs of eclipses either in the optical or the far-UV regions. Schmid and Schild (1997), based on spectropolarimetric observations, derived the orbital inclination $i = 60 (\pm 8.2°)$. The system undergoes occasional eruptions. The star's brightness abruptly increases by 1–3 magnitudes, often showing multiple maxima separated approximately by one year (Luthardt 1983; Viotti *et al.* 2007). The quiescent phase of AG Dra is characterized by a periodic wave-like variation, which is more pronounced at shorter wavelengths. Figure 2 (mid panel) shows a part of its recent LC covering both the quiescent and the active phases.

2.6. AX Persei

AX Per is known as an eclipsing symbiotic binary with an orbital period of 680 days (Skopal 1991). The cool component of the binary is a normal giant of spectral type M4.5 III (Mürset and Schmid 1999). The historical LC of AX Per is characterized by long-lasting periods of quiescence with the superposition of a few bright stages (see Figure 1 in Skopal *et al.* 2001). Figure 1 (bottom panel) demonstrates evolution in the LC covering a part of its last active phase with eclipses (1990–1994) and the transition to quiescence at 1995.8, followed by typical periodic waves in the star's brightness.

3. Wave-like orbitally-related variation

Wave-like, orbitally related variability represents the most characteristic feature of the LCs of symbiotic stars that develops during their quiescent phases.

Generally, we observe a periodic, wave-like profile of the LC, whose minima and maxima occur at or around conjunctions of the binary components. The inferior conjunction of the giant (the cool component in front of the hot star) corresponds to the light minimum (orbital phase $\varphi = 0$), while at its superior conjunction (the hot star in front) we observe a light maximum ($\varphi = 0.5$). This variation is characterized with a large magnitude difference between the minimum and maximum, $\Delta m \sim 1–2$ magnitudes. This "amplitude" is always larger in the blue part of the spectrum than in the red one, i.e. $\Delta U > \Delta B > \Delta V$. This relationship can be understood with the aid of the SED throughout the *UBV* region.

Figure 2 shows examples of this type of light variation for BF Cyg (it contains a red M5 giant with an effective temperature $T_{eff} \sim 3400$ K) and AG Dra (yellow K2 giant with $T_{eff} \sim 4300$ K) with their SEDs covering the optical domain. This spectral region is dominated by the radiation from the nebula and the giant. The latter does not depend on the orbital phase and strengthens considerably towards the longer wavelengths, while the nebular radiation has the opposite behavior (it dominates the *U* passband and is fainter in *V*) and it is the source of the orbitally-related variation (Section 5.2). Therefore, the Δm amplitudes are declining to longer wavelengths, where the nebular emission is superposed with the increasing light from the giant, which does not vary with the orbital motion.

In other words, the observed amplitude of the wave-like variation is proportional to the ratio of fluxes from the nebula and the giant, which is a function of the wavelength—flux from the giant/nebula increases/decreases with increasing lambda.

In the case of the so-called yellow symbiotic stars (they contain a giant of the spectral type K to G), the giant's contribution into the *V* passband is very strong, which produces very different ΔU and ΔV amplitudes: $\Delta U / \Delta V \gg 1$. If the system contains a red giant, its contribution in *V* is relatively lower in the total composite spectrum, which yields the ratio $\Delta U / \Delta V \geq 1$. In our example on Figure 2, $\Delta U / \Delta V$ is ~ 1.4 for BF Cyg, whereas for the yellow symbiotic star AG Dra, $\Delta U / \Delta V$ is ~ 10 (see also Figure 25 in Skopal (2005)). On the other hand, a markedly different amplitude in *U* (eventually in *B*) and *V* (eventually in *R*) filters signals the presence of a yellow cool component in the symbiotic system.

4. Eclipses

During the active phases of systems with high orbital inclination, a significant change in the minima profile is observed—the very broad profile

becomes narrow. As the minima coincide with the inferior conjunction of the cool component, it is believed that they are caused by eclipses of the hot object by the cool giant. Examples of this effect are shown in Figure 1 and in the top panels of Figure 4 for eclipsing symbiotic binaries BF Cyg, AX Per and CI Cyg.

According to spectroscopic observations, an optically thick shell—a false photosphere—is created around the hot active star, which redistributes a significant fraction of its radiation. As the characteristic temperature of the false photosphere (~22000 K, Skopal 2005) is considerably lower than that of the hot star during quiescence (~10^5 K), its light contribution will be shifted to longer wavelengths according to Wien's displacement law, and thus make the visual region brighter. The bottom left panel of Figure 4 shows an example of BF Cyg during its 1990 major outburst. The hot star pseudophotosphere radiates at the temperature $T_h = 21500$ K, and its luminosity contribution is above those from the giant and the nebula through the *UBV* domain. Since the radius of the false photosphere is a few solar radii, the cool giant can eclipse it easily for about one tenth of the orbital period (i.e., 2–3 months) that corresponds to a typical giant's radius of 100R and orbital periods as long as 2–3 years. The depth of eclipses usually obeys the relation: $\Delta U > \Delta B > \Delta V$, because the light from the hot star decreases towards the red part of the spectrum, while that from the giant increases. However, the resulting eclipse depth and color indices are modulated by the presence of a rather strong nebula in the system, which is not subject to eclipses (bottom mid panel of Figure 4). Thus, during totality the nebula partially fills-in the minima and, in combination with the radiation from the giant, produces color indices that differ significantly from those of a normal red giant. For example, we observed $U–V$ ~0, +0.5 and +1.2 for BF Cyg, AX Per, and CI Cyg, respectively, during their total eclipses (compare Figure 4, top). For a comparison, in a theoretical case that the nebula is not present outside the eclipsing giant's stellar disk, we should measure the color indices of a normal red giant, e.g. $U–V$ ~ +3 magnitudes (e.g., Lee 1970).

On the other hand, knowing the spectral type of the giant and having measured magnitudes at totality would allow us to estimate parameters of the contributing nebula—its emission measure and the electron temperature.

During the quiescent phase, radiation from the nebula dominates the optical—its contribution to the *UBV* passbands is well above those from the hot star and the giant (compare Figure 4, bottom right).

The nebula represents a very extended source of radiation in the symbiotic system, which thus cannot be subject to eclipse. As a result, we instead observe a very broad minima; the LC waves as a function of the orbital phase.

5. On the nature of the wave-like variations

5.1. Reflection effect

Originally, Boyarchuk (1966) and Belyakina (1970) suggested a reflection effect as being responsible for the periodic wave-like variation recorded in their

LC of AG Peg. In this model, the hot star irradiates and heats up the facing giant's hemisphere that causes variation in the star's brightness when viewing the binary at different orbital phases. The left panel in Figure 5 illustrates the scheme of the reflection effect as suggested by Kenyon (1986). At the inferior conjunction of the giant ($\varphi \sim 0$), we observe a minimum of the light, and conversely, at the giant's superior conjunction ($\varphi \sim 0.5$) we observe its maximum analogous to the Moon's phases.

This natural explanation was adopted by many authors (e.g., Kenyon 1986, Munari 1989), and it is still considered as a possible cause of the wave variation in LCs as a function of the orbital phase (Munari and Jurdana-Šepić 2002). However, the reflection effect fails to explain quantitatively the observed very large amplitudes of 1–2 magnitudes or more, because a normal red giant does not intercept enough radiation from the hot component to produce the strong emission spectrum and its variation. For symbiotic stars this case was investigated theoretically by Proga *et al.* (1996), who found that the magnitude difference between the illuminated and non-illuminated red giant hemisphere is less than 0.3 magnitude. Also, Skopal (2001) demonstrated that the observational characteristics of the LCs of symbiotic binaries—the large amplitude, the profile of minima, and variation in their positions (see Sect.~5.2)—cannot be reproduced by the reflection effect.

A better agreement between the observed and calculated variation in both the line and the continuum spectrum was achieved by including the neutral wind of the giant into the model, which thus could intercept a much larger amount of the hot star radiation (Proga *et al.* 1998). It became clear that the nature of the orbitally-related changes in the optical/near-UV continuum should be explained within the ionization model of symbiotic binaries, in which the hot star radiation ionizes a portion of the neutral wind from the cool giant.

5.2. Ionization model and the wave-like variability—A simple model

The right panel of Figure 5 shows the ionization structure given by the H II / H I boundaries between the ionized and neutral hydrogen in a symbiotic binary calculated for a gradual acceleration of the giant's wind with the terminal velocity of 20km/s and a steady state case (binary rotation and the gravitational attraction on the wind particles were neglected). The model was originally outlined by Seaquist, Taylor, and Button (1984) (hereafter STB) to explain the radio emission from symbiotic stars and elaborated later by Nussbaumer and Vogel (1987) as a new approach to symbiotic stars to determine their basic physical parameters (Mürset *et al.* 1991; Skopal 2005). The ionization boundary is a curve at which the flux of ionizing photons from the hot star is balanced by the flux of neutral particles (here we consider just hydrogen) from the cool star. In other words, it is defined by the locus of points at which ionizing photons are completely consumed along paths outward from the ionizing star. The shape of the boundary is thus given mainly by the binary properties—separation of the components, number of hydrogen ionizing photons, the mass-loss rate from

the giant, and terminal velocity of the wind particles (see in detail Seaquist, Taylor, and Button 1984; Nussbaumer and Vogel 1987).

Figure 5 shows examples of free HII / HI boundaries:

(i) The case when the flux of ionizing photons exceeds significantly that of neutral particles corresponds to a very extended symbiotic nebula—the neutral HI zone has a cone shape with the giant at its top.

(ii) If both the fluxes are approximately equal, dimensions of both the zones are comparable.

(iii) For a very low ionizing capability of the hot star the HII zone can be closed around the hot star.

The SEDs in Figures 2 and 4 demonstrate that the nebula represents a significant source of light in the visual region, mainly during quiescent phases. Figure 5 then suggests that this source of radiation is physically displaced from the giant that excludes directly the reflection effect to be responsible for the orbitally related wave-like variation in LCs. Therefore the principal question is how and why the symbiotic nebula can affect the observed light to explain this type of variability. In the following sections I will try to answer these questions.

5.3. Variation in the nebular emission and LCs

Skopal (2001) found a relationship between the wave-like variation in LCs and the radiation from the symbiotic nebula. Both dependencies are of the same type. We observe a maximum/minimum of the nebular emission around the conjunctions of the binary components, similar to the periodic, wave-like variation of the photometric magnitudes. Figure 3 demonstrates this case for V1329 Cyg (Section 2.4). Maximum/minimum of the nebular emission at $\varphi = 0.57$ / 0.95 (bottom panels) corresponds to the maximum/minimum in the LC (top).

Thus, the orbitally-related variation in the nebular component of radiation causes that which is observed in the LCs. This relationship can be verified by converting the observed amount of the nebular radiation, usually characterized by the emission measure, EM, to the scale of magnitudes. (Note: The flux produced by the nebula of a volume V with concentrations of ions (protons), n_+, and electrons, n_e, largely depends on the number of hydrogen recombinations, and is proportional to $\int n_+ n_e \, dV$—the so-called emission measure.) Under the assumption that the light from the nebula dominates the considered passband, which is usually satisfied for U, the stellar magnitude, for example, m_U, can be expressed as

$$m_U = -2.5 \log (EM) + C_U, \qquad (1)$$

where the constant C_U depends on the volume emission coefficient and the contribution of the zero magnitude star in U (see in detail Skopal 2001). Figure 3 shows a very good agreement between the B-magnitudes determined according to Equation (1) and those obtained by standard photometric measurements.

This result thus confirms the unambiguous connection between variations in the nebular emission and photometric measurements.

5.4. Why does the emission measure vary?

It is simple to imagine that the orbitally-related variations in the nebular emission are only apparent. This implies that a fraction of the nebular medium has to be partially optically thick to produce different contributions of its total emission into the line of sight at different orbital phases.

Within the STB model the opacity, κ, of the ionized emission medium decreases with the distance r from the giant, since $\kappa \propto$ density$(r) \propto r^{-2}$. This implies that the parts of the nebula closest to the boundary between the stars will be the most opaque.

In the case of the extensive emission zone, the optically thick portion of the HII region has the geometry of a canopy located on the boundary around the binary axis (Figure 5, right). Such a shape will attenuate most of the radiation at orbital phase 0 (i.e., the relatively largest part of the optically thin nebula will be obscured by it), while at phase 0.5, we will observe a maximum light from the nebula in agreement with the variation in EM and the LCs. In this case the LC profile will be a simple sinusoid.

In the case of an oval shape of the HII zone (Figure 5, the dotted curve) its total emission will be attenuated more at positions of the binary component's conjunctions (the orbital phases $\varphi = 0$ and 0.5) than at positions of $\varphi = 0.25$ and 0.75, when viewing the binary from its sides. Such apparent variation in the EM can produce the primary, but also a secondary minimum in the LC. The secondary minima of this nature are well demonstrated by the *U*–LC of EG And (see Figure 2 in Skopal 2005).

The above described approximation of the nebula shaping in a symbiotic system allow us to explain qualitatively just the most pronounced features of the LCs. A more accurate ionization structure, including the effect of the binary rotation and the gravitational attraction on the wind particles, has not been investigated yet. Nevertheless, an asymmetry of the nebula with respect to the binary axis (i.e., the line connecting the stars) can be indicated observationally. The recently discovered effect of apparent changes in the orbital period gives evidence of this possibility.

6. Apparent changes in the orbital period

This effect is connected with transitions between the active and quiescent phases of a symbiotic system. Aside from the significant change of the minima profile during these periods (Section 4, Figure 4), a systematic variation in the minima position, i.e., the effect of apparent orbital changes, was revealed (Skopal 1998).

6.1. Systematic variation in the O–C residuals

Here I will demonstrate this effect on the historical LC of the eclipsing symbiotic system BF Cyg (Figure 6). First, we determine positions of the observed ("O") minima in its LC and calculate those ("C") using a reference ephemeris. Then we construct the so-called O–C diagram (i.e., the residuals between the observed and calculated timing of the minima). In our example of BF Cyg the O–C diagram was constructed using the reference ephemeris given by all the primary minima measured by Skopal (1998):

$$JD_{Min} = 2411268.6 + 757.3 \, (\pm 0.6) \times E, \qquad (2)$$

which is identical (within uncertainties) with the spectroscopic ephemeris of Fekel *et al.* (2001).

A systematic variation in the O–C residuals is clearly seen. This behavior was already noted by Jacchia (1941). The gradual increase of the O–C values before the 1920 bright stage (E = 1 to 11) corresponds to an apparent period of 770 days, larger than the orbital one, while their subsequent decrease (E = 12 to 24) indicates a shorter period of 747 days.

The same type of variability appeared again during the recent, 1989 active phase. Observed changes in both the position and the shape of the minima are illustrated in the top left panel of Figure 4, and in Figure 6. During the transition *from the active phase to quiescence* (A → Q transitions), a systematic change in the minima positions at E = 49 to 51 corresponded to the apparent period of only 730 days.

During the transition *from the quiescent to the active phase* (Q → A transitions), a significant change in the O–C values by a jump of +130 days was observed. The minima positions at E = 47 and E = 49 indicate an apparent period of 822 days.

6.2. Asymmetric shape of the HII zone

To explain the observed apparent changes in the orbital period, the HII zone has to be extended asymmetrically with respect to the binary axis. Asymmetrical shape of the ionized region in symbiotic stars was also suggested, for example, by:

(i) spectropolarimetric studies of Schmid (1998) and

(ii) hydrodynamical calculations of the structure of stellar winds in symbiotic stars that include effects of the orbital motion (e.g., Folini and Walder 2000).

In both models the ionization front in the orbital plane is twisted, going from the side of the hot star that precedes its orbital motion, through the line joining the components, to the front of the cool star against its motion. Therefore, it is possible to assume that the main nebular region follows the S-shaped track from the front of the hot star orbital motion to the binary axis. Thus, the optically thick fraction of the HII region is prolonged so that its major axis at the orbital plane points the observer around the orbital phase 0.9.

6.3. Principle of apparent orbital changes

During the A → Q transitions, the optically thick shell is gradually diluting, which leads to the increase of the hot star temperature and thus production of the ionizing photons. As a result, the nature of the optical continuum declines and changes significantly—from blackbody to nebular radiation (Figure 4, bottom left and right panel). This process causes an *expansion* of the HII zone and thus the change of the minimum profile from narrow to broad wave throughout the orbital cycle. According to the asymmetry of the nebula (Section 6.2) the light minima occur prior to the time of spectroscopic conjunction. This behavior is also illustrated by the top panels of Figure 4. Thus, during the A → Q transitions we indicate an apparent period, which is *shorter* than the orbital one.

During Q → A transitions a sudden decrease in the luminosity of the ionizing photons results from rather rapid creation of the false relatively cool photosphere. This implies a disruption of the HII zone. The optical region is then (usually) dominated by the stellar radiation from the pseudophotosphere and a narrow minimum (eclipse) is observed at the inferior conjunction of the giant. In such a case the time difference between the preceding broad minimum ($\varphi \approx 0.9$) and the eclipse ($\varphi \approx 0$) is $P_{app} \approx P_{orb} + 0.1 \times P_{orb}$. This apparent change in the period happens suddenly, and in the O–C diagram is indicated by a jump in the residuals. In our illustration of BF Cyg (Figure 6, minima just prior to the 1989 outburst), the timing of the broad minimum at the epoch $E = 47$ and the following eclipse at $E = 49$ corresponds to the apparent period $P_{app} \approx 822$ days.

7. Concluding remarks

7.1. A complexity of LC profiles

We have discussed only the fundamental variations in the LCs of symbiotic stars, i.e., those that can be explained with the aid of a basic model. However, LCs of symbiotic stars record a much larger variety of light changes that are unexpected and never repeat again. For example, during quiescence the wave-like variation is not a simple sinusoid, but alters its profile from cycle to cycle in both scales—time and brightness (e.g., EG And, AG Peg, AX Per, see Skopal *et al.* 2007). During active phases the LC profiles are very heterogeneous. Eruptions arise unexpectedly with a rapid increase (e.g., RS Oph and most of AG Dra events), or more frequently with a gradual increase to the maximum within a few months (e.g., recent outbursts of Z And and AG Dra (Skopal *et al.* 2006; Skopal *et al.* 2007)). Also the recurrence time is an unpredictable phenomenon. For some objects no active phase has yet been recorded (e.g., SY Mus, RW Hya, EG And). For others, eruptions are scattered in historical LCs irregularly. For example, during the 1994–1998 period the AG Dra LC (Figure 2) showed eruptions with a strict recurrence of ~1 year (Viotti *et al.* 2007).

Previously, Iijima *et al.* (1987) suggested that since 1930 AG Dra periodically entered active stages with an interval of about 15 years. However, from the

beginning of its historical records of the brightness from 1890 to about 1927, it was quiet with a first strong outburst indicated around 1932 (Robinson 1969). Another illustrative example in this respect is YY Her (Munari *et al.* 1997). In addition, an even more complex profile of the LC is observed when different types of eruptions (nova-like, Z And-type, flares) are superposed. An example here is the historical LC of BF Cyg (Figure 6; see Skopal *et al.* 1997).

7.2. The problem of eclipses

Eclipses can suddenly arise in the LC during active phases of symbiotics with a high orbital inclination (Section 4). However, their presence is not stable during each outburst of some symbiotic objects. For example, evidence for eclipses in the symbiotic triple system CH Cyg were reported by Skopal *et al.* (1996). However, those produced by the inner symbiotic binary were observed only during the lower level of the activity (1967–1971 and 1992–1995).

Generally, the depth of eclipses is very sensitive to the location of the main sources of radiation in the system and their relative contributions at the considered passband, which both can be subject to variation during different active phases. Therefore the eclipse effect can be observed only at specific brightness phases, at which the radiative contribution from a pseudophotosphere in the optical rivals that of the nebula. In addition, in the the case of CH Cyg, the effect of the precession of the inner orbit (i.e., that with the symbiotic pair) with a period of 6,520 days and the precession cone opening angle of 35° (Crocker *et al.* 2002) is probably the main cause of the intriguing behavior of eclipses in this system.

An additional problem connected with eclipses in symbiotic binaries is their width. In some cases it is too large to be explained by a simple eclipse of the hot object by the stellar disk of the giant. Examples here are BF Cyg (Skopal *et al.* 1997) and TX CVn (Skopal *et al.* 2007). In the case of Z And the broad eclipse profile suggested a disk-like structure for the hot object during active phases (Skopal 2003).

7.3. Importance of the photometric monitoring

The diversity of variations recorded in the LCs of symbiotic stars is thus far beyond our full understanding. The investigation of interactions between the cool giant and its hot luminous compact companion in a symbiotic binary requires simultaneous, multi-frequency observations from X-rays to radio wavelengths. This is an extremely challenging task, addressed mainly to large ground-based telescopes and those on satellites.

In spite of this, the photometric monitoring of symbiotic stars, usually carried out with small telescopes, plays an important role in such research. I summarize some reasons as follows:

(i) Monitoring usually first discovers an unpredictable sudden change in the brightness and thus can provide an alert for observation with other facilities.

(ii) Color indices can provide information about the nature of the composite continuum and thus to help to identify the responsible process.

For example, the very negative intrinsic (i.e., dereddened and corrected for lines) *U–B* index is usually connected with optical brightening that signals the energy conversion from the hot star to the nebular emission. Some examples were discussed by Skopal *et al.* (2006) and Tomov *et al.* (2004).

(iii) The eclipse profiles can help to recognize the structure of the hot active object—a spherical or a disk-like structure. Disentangling the color indices during the totality allows us to quantify the contribution from the non-eclipsed fraction of the nebula (Section 4).

(iv) The minima during quiescence, whose profiles reflect the geometry of the nebula, can determine the difference between the simplified ionization structure (compare Figure 4) and the real situation including effects of the binary motion and accretion.

(v) Variation in the LC profile in the *UB*[*V*] bands around the orbital phase φ ~ 0.5 (e.g., presence/absence of a secondary minimum) can probe the extension of the nebula—if it is closed or open in the sense of the STB model (Figure 5, Section 5.2).

(vi) A double-wave profile in the [*V*]*RI* passbands implies the possibility of the ellipsoidal shape of the red giant due to tidal distortion and thus can discriminate the type of mass transfer process (via the wind or the Roche lobe overflow?).

(vii) An intrinsic variability of the giant component in symbiotic binaries monitored in the *VRI* passbands can provide physical parameters for such "pulsation-type" of variability. Objects as CH Cyg, CI Cyg, AG Peg, and AR Pav are promising candidates here (Mikołajewski *et al.* 1992; Belyakina and Prokofieva 1991; Skopal *et al.* 2007; Skopal *et al.* 2000).

(viii) Multicolor LCs, if properly corrected for influence of emission lines (Skopal 2007), can provide a satisfactory tool to calibrate spectroscopic observations and thus be useful in determining other physical parameters.

(ix) Evolution in the LC profile at the very beginning stage of outbursts is of particular importance to mapping the process igniting the eruption (e.g., Sokoloski *et al.* 2006).

8. Acknowledgements

References

Belyakina, T. S. 1970, *Astrofizika*, **6**, 49.

Belyakina, T. S. 1976, *Inf. Bull. Var. Stars*, No. 1169.

Belyakina, T. S. 1979, *Izv. Krymskoj Astrofiz. Obs.*, **59**, 133.

Belyakina, T. S. 1984, *Izv. Krymskoj Astrofiz. Obs.*, **68**, 108.

Belyakina, T. S. 1992, *Izv. Krymskoj Astrofiz. Obs.*, **84**, 49.

Belyakina, T. S., and Prokofeva, V. V. 1991, *Astron. Zh.*, **68**, 314.

Boyarchuk, A. A. 1966, *Astron. Zh.*, **43**, 976.

Crocker, M. M., Davis, R. J., Spencer, R. E., Eyres, S. P. S., Bode, M. F., and Skopal, A. 2002, *Mon. Not. Roy. Astron. Soc.*, **335**, 1100.

Fekel, F. C., Hinkle, K. H., Joyce, R. R., and Skrutskie, M. F. 2001, *Astron. J.*, **121**, 2219.

Folini, D., and Walder, R. 2000, *Astrophys. Space Sci.*, **274**, 189.

Formiggini, L., and Leibowitz, E. M. 1994, *Astron. Astrophys.*, **292**, 534.

Iijima, T., Vittone, A., and Chochol, D. 1987, *Astron. Astrophys.*, **178**, 203.

Jacchia, L. 1941, *Bull. Harvard Coll. Obs.*, No. 915.

Kenyon, S. J. 1986, *The Symbiotic Stars*, Cambridge Univ. Press, Cambridge, p. 27.

Kenyon, S. J., Oliversen, N. A., Mikołajewska, J., Mikołajewski, M., Stencel, R. E., Garcia, M. R., and Anderson, C. M. 1991, *Astron. J.*, **101**, 637.

Lee, T. A. 1970, *Astrophys. J.*, **162**, 217.

Luthardt, R. 1983, *Mitt. Veränderliche Sterne*, **9**, 129.

Mikołajewska, J., Mikołajewski, M., and Kenyon, S. J. 1989, *Astron. J.*, **98**, 1427.

Mikołajewski, M., Mikołajewska, J., and Khudyakova, T. N. 1992, *Astron. Astrophys.*, **254**, 127.

Munari, U. 1989, *Astron. Astrophys.*, **208**, 63.

Munari, U., and Jurdana-Šepić, R. 2002 *Astron. Astrophys.*, **386**, 237.

Munari, U., Margoni, R., and Mammano, A. 1988, *Astron. Astrophys.*, **202**, 83.

Munari, U., *et al.* 1997, *Astron. Astrophys.*, **323**, 113.

Mürset, U., Nussbaumer, H., Schmid, H. M., and Vogel, M. 1991, *Astron. Astrophys.*, **248**, 458.

Mürset, U., and Schmid, H. M. 1999, *Astron. Astrophys., Suppl. Ser.*, **137**, 473.

Nussbaumer, H., and Vogel, M. 1987, *Astron. Astrophys.*, **182**, 51.

Nussbaumer, H., and Vogel, M. 1989, *Astron. Astrophys.*, **213**, 137.

Proga, D., Kenyon, S. J., and Raymond, J. C. 1998, *Astrophys. J.*, **501**, 339.

Proga, D., Kenyon, S. J., Raymond, J. C., and Mikołajewska, J. 1996, *Astrophys. J.*, **471**, 930.

Robinson, L. 1969, *Perem. Zvezdy*, **16**, 507.

Schmid, H. M. 1998, *Rev. Mod. Astron.*, **11**, 297.

Schmid, H. M., and Schild, H. 1997, *Astron. Astrophys.*, **321**, 791.

Seaquist, E. R., Taylor, A. R., and Button, S. 1984, *Astrophys. J.*, **284**, 202.

Skopal, A. 1991, *Inf. Bull. Var. Stars*, No. 3603.

Skopal, A. 1998, *Astron. Astrophys.*, **338**, 599.

Skopal, A. 2001, *Astron. Astrophys.*, **366**, 157.

Skopal, A. 2003, *Astron. Astrophys.*, **401**, L17.

Skopal, A. 2005, *Astron. Astrophys.*, **440**, 995.

Skopal, A. 2007, *New Astron.*, **12**, 597.

Skopal, A., Bode, M. F., Lloyd, H., and Tamura, S. 1996, *Astron. Astrophys.*, **308**, L9.

Skopal, A., Djurašević, G., Jones, A., Drechsel, H., Rovithis-Livaniou, H., and Rovithis, P. 2000, *Mon. Not. Roy. Astron. Soc.*, **311**, 225.

Skopal, A., Teodorani, M., Errico, L., Vittone, A. A., Ikeda, Y., and Tamura, S. 2001, *Astron. Astrophys.*, **367**, 199.

Skopal, A., Vaňko, M., Pribulla, T. *et al.* 2007, *Astron. Nachr.*, **328**, 909.

Skopal, A., Vittone, A., Errico, L., Bode, M. F., Lloyd, H. M., and Tamura, S. 1997, *Mon. Not. Roy. Astron. Soc.*, **292**, 703.

Skopal, A., Vittone, A. A., Errico, L., Otsuka, M., Tamura, S., Wolf, M., and Elkin, V. G. 2006, *Astron. Astrophys.*, **453**, 279.

Sokoloski, J. L. 2003, *J. Amer. Assoc. Var. Star Obs.*, **31**, 89.

Sokoloski, J. L., *et al.* 2006, *Astrophys. J.*, **636**, 1002.

Tomov, N. A., Tomova, M. T., and Taranova, O. G. 2004, *Astron. Astrophys.*, **428**, 985.

Viotti, R. F., Friedjung, M., González-Riestra, R., Iijima, T., Montagni, F., and Rossi, C. 2007, *Baltic Astron.*, **16**, 20.
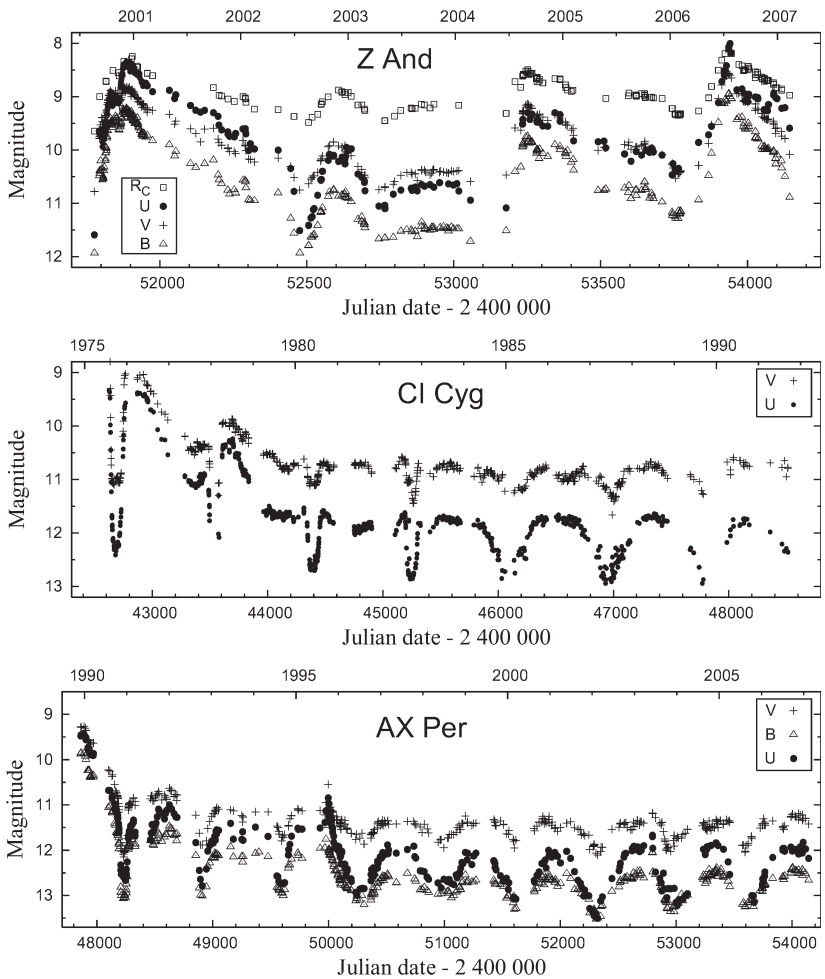
Figure 1. Top: The *UBVR*$_C$ LCs of Z And covering two major eruptions that peaked in 2000 December and 2006 July (from Skopal *et al.* 2007). Middle: Example of *U* and *V*LCs of CI Cyg from its 1975 outburst with narrow minima—eclipses. From about 1984 eclipses transferred into wave-like variation signaling thus quiescent phase. The data are from Belyakina (1992). Bottom: The *UBV*LCs of AX Per covering a part of its 1989–1994 active phase and the following quiescence from 1995 (see Skopal *et al.* 2001).
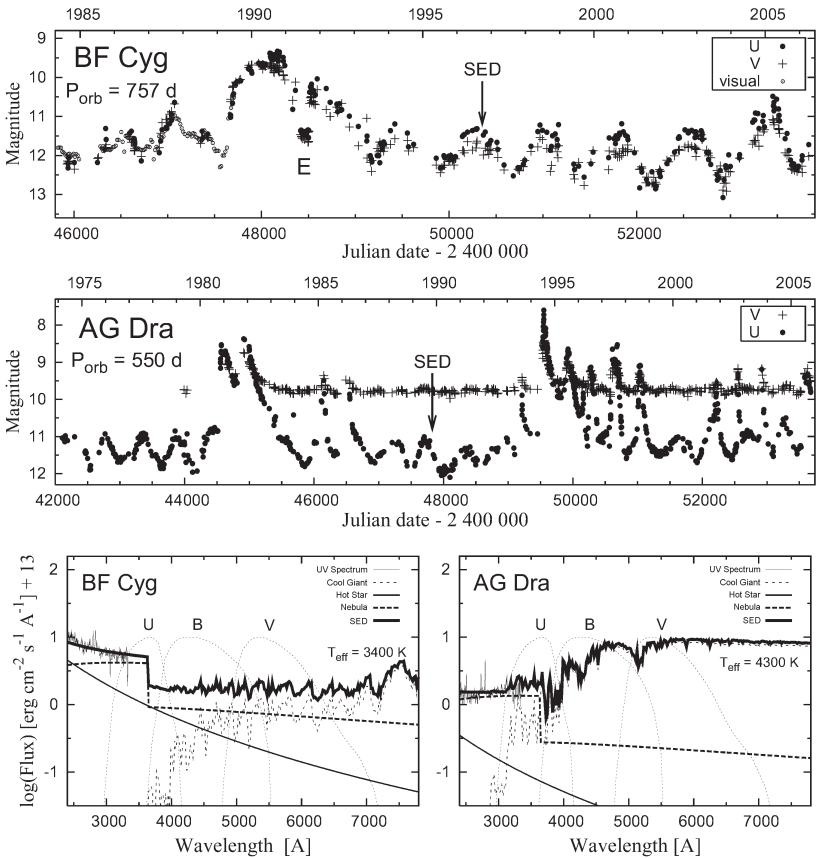
Figure 2. Top panels show the LCs of BF Cyg and AG Dra in *U* and *V* filters. During active phase the eclipsing system BF Cyg displays a relatively narrow minimum at the inferior conjunction of the giant (denoted by "E"), while during quiescent phase its LC shows pronounced wave-like variation, characterized with amplitudes $\Delta U \approx \Delta V \sim 1.5$ mag. The yellow symbiotic star AG Dra is not eclipsing. Amplitudes of its wave-like variations are smaller and depend considerably on the color: $\Delta U \sim 1$ mag, $\Delta V \sim 0.1$ mag. The bottom panels show the SEDs of these objects throughout the *UBV* passbands, which explains the observed differences in the wave-like variation (Section 3).
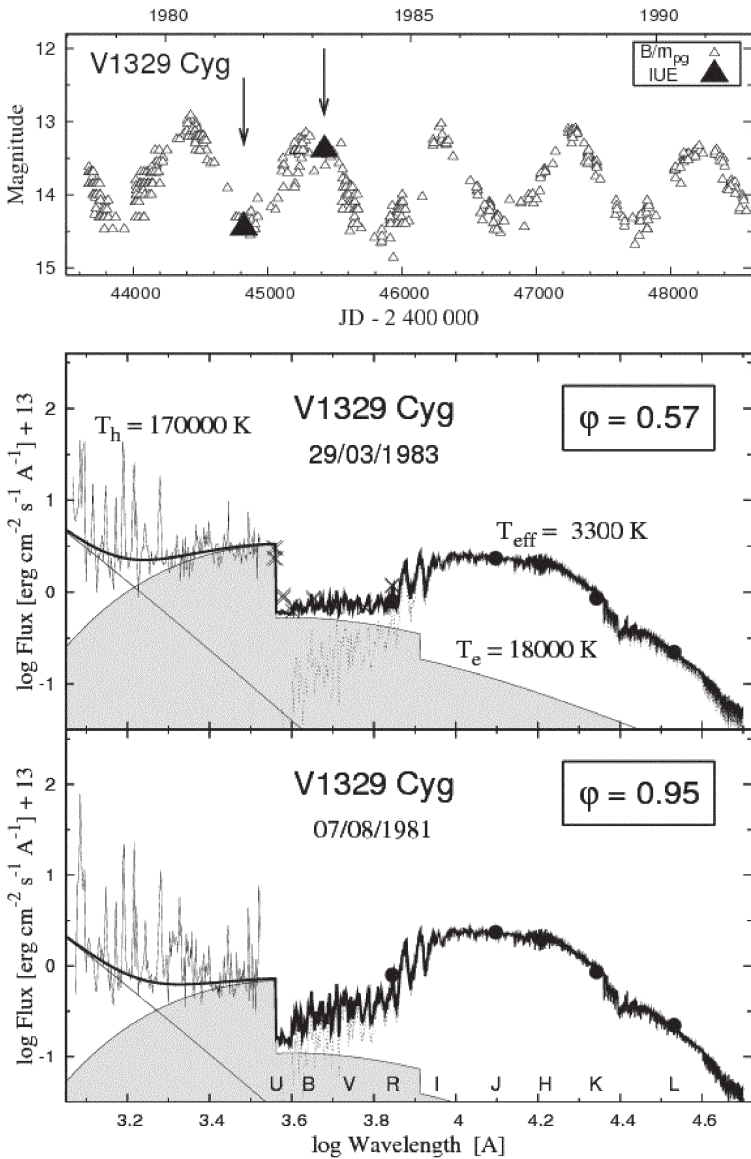
Figure 3. Example of the wave-like, orbitally-related variation in the LC of V1329 Cyg during quiescent phase (top). It is caused by variation in the quantity of the nebular radiation observed at different orbital phases (bottom panels). Magnitudes derived from the IUE spectra agree perfectly with those obtained photometrically (filled triangles in the top panel). This result thus demonstrates that the periodic variation in the nebular radiation is responsible for that observed in the LCs.
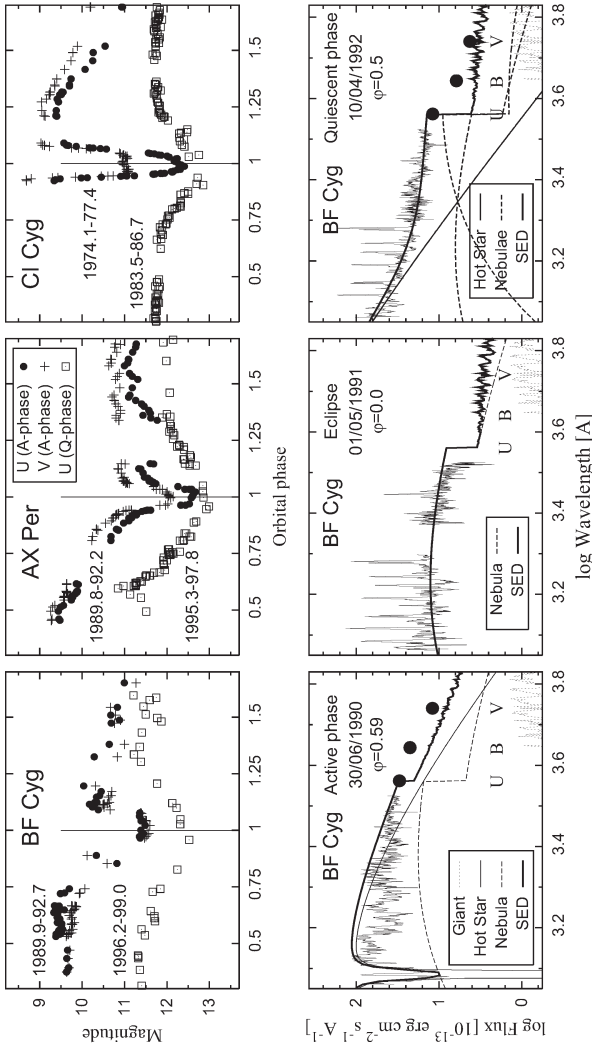
Figure 4. Eclipses plus wave variation and SEDs. Bottom: Examples of the SED during the active phase (left panel), eclipse (middle) and quiescent phase (right) of BF Cyg. During activity contribution from a warm false photosphere around the hot star is larger than that from the nebula in the *UBV* region. As a result we observe narrow minima—eclipses—in the LC at the inferior conjunction of the giant. The minima are in part filled in with rather strong residual light from the nebula, which is not subject to eclipse (mid panel). During quiescence the radiation from extended nebula(e) dominates the UBV region (right panel), which causes the minima to be very broad. Top panels demonstrate how these SED variations are reflected by the LCs of eclipsing systems BF Cyg, AX Per, and CI Cyg.
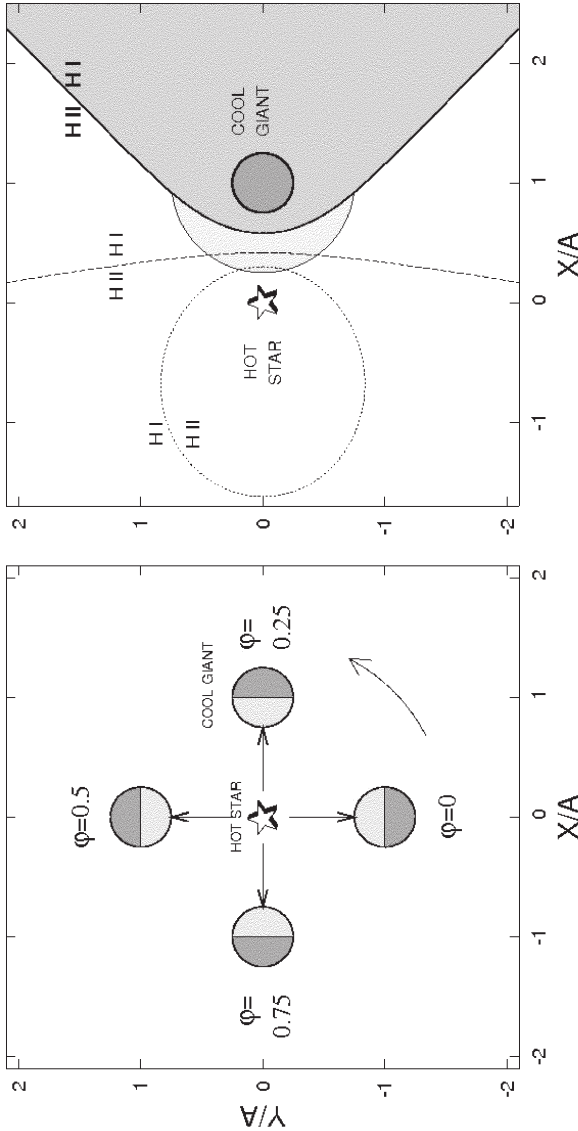
Figure 5. Left: Schematic representation of the reflection effect. Within this model the wave-like, orbitally-related variation in LCs of symbiotic stars results from different visibility of the illuminated giant's hemisphere (the lighter one facing the hot star) at different phases. This model, however, neglects the effect of ionization of the neutral wind from the giant. Right: The STB (1984) ionization structure of the hydrogen in symbiotic binary. The boundary between the ionized and neutral hydrogen (HII / HI) for a strong (heavy solid line), moderate (dashed line), and faint (dotted line) source of the ionizing photons (i.e., the hot star). Within this model the wave-like variability results from a different projection of the optically thick portion of the ionized zone (the light gray part of the HII zone) into the line of sight (see Section 5.2).
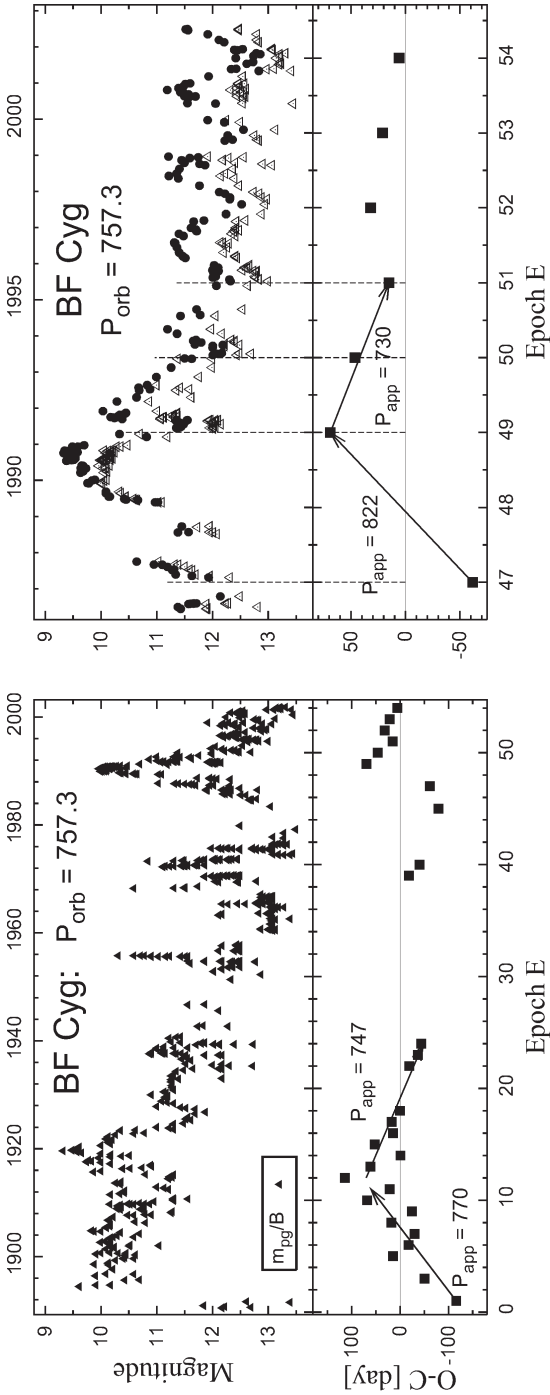
Figure 6. Historical and recent LCs of BF Cyg with the O–C diagrams. During transition from quiescent to active phases and vice versa, the main source of radiation contributing to the optical continuum changes significantly its location and geometry in the symbiotic system. As a result the observed minima change their profile and position, what we indicate in the O–C diagram as the apparent orbital changes. Filled triangles represent m_{pg}/B magnitude; open triangles, B magnitude; filled circles, U magnitude.

On the Connection Between CWA and RVA Stars

Patrick Wils
Aarschotsebaan 31, B-3191 Hever, Belgium; Vereniging Voor Sterrenkunde, Belgium

Sebastián A. Otero
Olazabal 3650-8C, 1430 Buenos Aires, Argentina; Grupo Wezen 1 88, Centro de Estudios Astronómicos (CEA)

Abstract   Phase plots of ASAS-3 data of a large number of CWA and RVA variable stars reveal that there is no clear distinction in period or light curve shape between these two types of stars.

1. Discussion

An evolutionary connection has long been conjectured between CWA stars (W Vir type stars or Population II Cepheids) and RVA stars (RV Tau type stars with constant mean magnitude). For a recent review, see Wallerstein (2002). CWA stars are usually defined as pulsating yellow giants with periods between 8 and 20 days, an amplitude up to about one magnitude, and fairly stable light curves. The distinguishing feature of RVA stars is that they have alternating bright and faint minima, and more erratic light curves (subsequent cycles are not necessarily identical). Their periods (between faint minima, so with two maxima per cycle) range between 40 and 150 days.

Templeton and Henden (2007) recently revealed that W Vir, the prototype of the CWA class, also showed a small but distinct brightness difference between consecutive minima in a similar way as the RVA stars. Abt (1954) had already noted significant cycle-to-cycle variations in W Vir. Also, Arp (1955) had found two type II Cepheids in the globular clusters M5 and M10 that showed alternating minima. In view of this it may be questioned as to how much the light curves between these two types of variable stars really differ. To look into this matter ASAS-3 data (Pojmański 2002) for 136 stars classified as CWA or RVA were plotted ordered according to their (double "RVA style") period (see Figure 1). These stars were collected mostly from the GCVS (Samus and Durlevich 2004) and the ASAS-3 catalogue (Pojmański 2002), plus some yet unclassified ones with very similar light curves. Some RVB stars (RV Tau, R Sge, and U Mon) that showed only a small change in mean brightness during the years ASAS-3 observed them were also included. The complete list of stars is given in Table 1. Note that some stars are misclassified in the GCVS.

It is clear from Figure 1 that there is no progression between these light curves according to period similar to the Hertzsprung progression in Population

I Cepheids (Hertzsprung 1926). The stars in the plots show a wide variety of light curve shapes, and similarly shaped light curves are seen at quite different periods. It is also noted that a number of stars classified as RVA do not really show alternating minima, while some stars classified as CWA do. In addition the phenomenon of alternating minima is not bound exclusively to a specific period range; stars not showing alternating minima have periods between those of stars that do. The difference in depth between minima cannot be considered a means of distinguishing stars either. Although stars with longer period in general show more scatter in their phase plots, some stars with long periods do not show much scatter.

In Figure 2 the *V–H* color of these stars is plotted against the *H–K$_s$* color. The average *V* magnitude derived from ASAS-3 data is used and the infrared magnitudes *H* and *K$_s$* are taken from the 2MASS survey (Skrutskie *et al.* 2006). The *H–K$_s$* color is almost free from interstellar extinction. The 2MASS data are from one epoch only, and may depend on the phase at which they were taken. However, plotting the *H–K$_s$* color against phase did not reveal a particular trend, and amplitudes in the infrared are much lower anyway.

Two distinct groups may be distinguished in Figure 2, and the border between the two may be roughly defined as *H–K$_s$* = 0.4. The stars of the first group to the left follow more or less a linear trend. The second group to the right of the plot is a more heterogeneous group showing infrared excess. The latter is usually also considered an indication of RV Tau variability (most of the RVB stars show infrared excess as the phenomenon of changing mean magnitude is often linked to circumstellar dust). However, stars classified as CWA and RVA appear in both of these groups. Also, the fact that whether stars show alternating minima or not does not determine into which one of the color groups they fall. Furthermore, the periods of the stars with infrared excess are not confined to a specific range either, as can be seen in Figure 3.

It may be concluded that there is no real indication from light curve shape, period, or color which determines whether a given pulsating yellow giant is a CWA or RVA type variable. The border between these classes of variable stars is not clearly defined on the basis of these criteria. One may wonder whether there is any need to distinguish between them at all.

2. Acknowledgements

References

Abt, H. 1954, *Astrophys. J., Suppl. Ser.*, **1**, 63.

Arp, H. C. 1955, *Astron. J.*, **60**, 1.

Hertzsprung, E. 1926, *Bull. Astron. Inst. Netherlands*, **3**, 115.

Pojmański, G. 2002, *Acta Astron.*, **52**, 397.

Samus, N. N., and Durlevich, O. V. 2004, *Combined General Catalogue of Variable Stars* (GCVS4.2, http://www.sai.msu.su/groups/cluster/gcvs/ gcvs), Sternberg Astronomical Institute, Moscow.

Skrutskie, M. F., *et al.* 2006, *Astron. J.*, **131**, 1163.

Templeton, M. R., and Henden, A. A. 2007, *Astron. J.*, **134**, 1999.

Wallerstein, G. 2002, *Publ. Astron. Soc. Pacific*, **114**, 689.

Watson, C., Henden, A. A., and Price, A. 2006, "The International Variable Star Index (VSX)" (http://www.aavso.org/vsx/index.php?view=search. top), AAVSO, Cambridge. MA.

Table 1. Stars with CWA- or RVA-like light curves in the ASAS-3 data. The type listed is from the GCVS and ASAS-3 online catalogues and from VSX (Watson *et al.* 2006) when the former were not available. The (RVA style) period and the *V* range are derived from ASAS-3 data, *H* and K_s are taken from the 2MASS catalogue.

Name	Type	Period (d)	V_{max}	V_{min}	V–H	H–K_s
VSX J192006.9+124743	CW	17.26	10.2	10.6	4.41	0.34
PZ Aql	CWA	17.51	11.3	12.1	3.57	0.25
AX Tel	CWA	19.79	12.3	13.2	1.86	0.10
ASAS 001430+1331.1	CW-FU/EC	19.80	11.8	12.7	3.45	0.22
AL Vir	CWA	20.60	9.2	9.9	1.76	0.04
AP Her	CWA	20.79	10.4	11.2	2.37	0.13
BH Oph	CWA	22.10	11.6	12.5	1.84	0.09
V775 Oph	CWA	24.29	13.3	13.9	2.49	0.16
V1304 Sgr	CWA	25.83	12.4	13.5	2.48	0.18
AL Lyr	CWA	25.96	11.8	12.6	2.95	0.18
DD Vel	CWA	26.37	12.2	13.1	3.90	0.28
KT Sco	CW-FU	26.43	12.6	13.3	2.16	0.08
V1077 Sgr	CWA	26.85	12.5	13.5	1.46	0.11
V802 Sgr	CWA	27.04	13.2	14.2	2.55	0.17
V2338 Oph	CWA:	27.32	11.6	12.3	2.81	0.08
V410 Sgr	CWA	27.56	12.2	13.2	1.65	0.17
V1185 Sgr	CWA	27.80	12.5	13.1	2.37	0.15
ASAS 050514+2145.8	CW-FU	27.87	12.2	13.2	2.65	0.19
V1834 Sgr	CWA	28.01	12.9	13.9	2.31	0.11
V1189 Sgr	CWA	28.18	11.7	12.9	2.03	0.08
V801 Aql	CWA	28.32	13.2	13.8	3.18	0.18
V445 Cen	E/DS:	28.39	11.5	12.5	2.31	0.12
YZ Vir	CWA	28.95	12.7	13.9	1.66	0.07
V833 Oph	CWA	29.42	13.6	14.7	2.07	0.07
V554 Oph	CWA	29.65	12.7	13.9	3.63	0.22
BO Tel	CWA	29.65	12.1	13.3	1.56	0.12
NW Pav	CWA	29.76	11.6	12.9	2.22	0.12
V1187 Sgr	CWA	30.21	13.3	14.0	2.62	0.15
V741 Sgr	CWA	30.29	12.3	13.4	2.15	0.14
ASAS 133028–3812.5	CW-FU	30.50	12.6	13.6	1.87	0.07
ASAS 211406+0019.2	CW-FU	30.56	11.9	13.0	2.08	0.08
V347 CrA	CWA	30.62	12.3	13.3	2.19	0.11
GSC 6666–00796	CWA	31.17	12.4	13.3	1.90	0.14
CO Pup	CWA	32.13	10.4	11.4	2.58	0.15
V557 Sgr	CWA	32.45	13.2	14.1	3.40	0.13

(Table 1 continued on following pages)

Table 1. Stars with CWA- or RVA-like light curves in the ASAS-3 data, continued.

Name	Type	Period (d)	V_{max}	V_{min}	V–H	$H–K_s$
UX Lup	CWA	32.47	12.6	13.6	2.11	0.15
SZ Mon	RVA	32.67	9.7	10.8	2.09	0.55
V478 Oph	CWA	32.83	12.6	13.5	2.53	0.08
V383 Sgr	CWA	32.86	12.3	13.7	1.93	0.14
V449 CrA	CWA	32.97	12.9	14.3	1.94	0.11
V2530 Sgr	CWA	33.66	13.0	14.0	3.11	0.25
ASAS 140434–4532.4	CW-FU	33.97	13.0	14.0	2.09	0.10
AL CrA	CWA	34.11	11.5	12.6	2.24	0.13
W Vir	CWA	34.53	9.5	10.7	1.74	0.04
V1303 Sgr	CWA	36.91	12.2	13.2	4.12	0.28
ST Pup	CWA	37.64	9.5	10.6	1.78	0.17
Z Aps	UGZ	37.89	10.9	11.7	2.71	0.19
EZ Aql	RVA	38.70	11.8	13.7	2.99	0.70
CY Vel	CWA	39.06	12.3	13.7	3.48	0.22
MR Ara	CWA	39.63	11.0	12.1	2.05	0.11
RS Pav	CWA	39.88	10.1	11.6	2.65	0.12
V1950 Oph	CWA:	42.21	12.4	13.3	3.50	0.48
EP Mus	CWA:	42.66	11.6	13.1	3.11	0.16
V760 Sgr	RVA	44.98	10.8	11.8	4.18	0.36
SY Cir	RV	46.26	11.6	13.2	3.17	0.16
V420 Cen	CWA	49.17	9.5	10.5	1.85	0.11
RX Lib	CWA	49.86	11.7	13.0	2.66	0.15
CN Cen	RVA	50.71	12.6	13.6	3.40	0.47
ASAS 202412-2457.0	CW-FU	51.37	12.4	13.7	2.19	0.09
ASAS 151825+0203.0	CW-FU	51.42	10.2	10.8	1.71	0.13
GP Mus	CWA	52.88	12.1	12.8	3.15	0.17
V2600 Oph	RV	53.10	11.6	12.8	3.48	0.15
V1831 Sgr	CWA	53.13	12.4	13.6	3.21	0.18
V415 Cen	CWA	53.16	12.3	13.4	2.72	0.14
V626 Sgr	CWA	53.45	11.8	13.4	2.33	0.07
GSC 8303-0183		53.65	11.8	13.3	2.80	0.28
GK Car	RV	55.12	11.2	12.2	2.92	0.55
V564 Sgr	CWA	55.67	12.3	13.2	2.86	0.55
V1290 Sgr	CWA	55.82	12.1	13.4	2.45	0.16
V1711 Sgr	CWA	56.88	10.4	11.1	2.15	0.49
UY Ara	RV	56.94	10.6	11.3	1.51	0.54
TW Cap	CWA	57.18	10.1	11.2	2.00	0.05
V446 Sco	CWA	57.29	12.7	13.7	3.01	0.22

(Table 1 continued on following pages)

Table 1. Stars with CWA- or RVA-like light curves in the ASAS-3 data, continued.

Name	Type	Period (d)	V_{max}	V_{min}	V–H	H–K$_s$
V594 Pup	RV	57.86	11.1	12.5	2.66	0.11
DI Car	*	58.34	9.7	11.8	2.48	0.26
ASAS 132605-4723.7	CW-FU	58.53	10.5	11.6	1.61	0.11
V541 Oph	CWA	58.92	13.1	14.3	4.88	0.24
V1670 Sgr	CWA	59.21	12.4	13.3	2.59	0.18
V423 Sco	RV	59.70	12.9	14.1	3.30	0.18
V2510 Sgr	CWA	60.66	12.7	14.1	3.37	0.22
CQ Sco	CWA	60.91	12.1	13.2	2.86	0.17
DY Ori	RV:	60.94	11.3	12.0	4.19	0.40
TT Oph	RVA	61.13	9.5	10.7	2.66	0.11
GSC 5663-0767		61.36	13.2	14.2	4.01	0.23
KQ CrA	CWA	61.74	11.9	12.8	2.50	0.15
IRAS 11472-0800		62.56	11.5	12.0	2.64	0.42
V2526 Sgr	CWA	63.05	12.9	13.9	3.31	0.15
V558 Sgr	RV	63.35	12.6	13.4	2.67	0.21
RR Mic	CWA	63.50	11.0	11.8	1.70	0.13
LN Aql	RV	64.71	13.0	14.0	2.68	0.15
RU Cen	RV	64.81	8.6	9.6	1.80	0.27
HI Tel	RVA	66.28	10.6	11.6	2.03	0.12
AD Aql	RVA	66.44	11.2	11.8	2.30	0.13
CT Ori	RV:	67.06	10.1	10.8	2.49	0.32
RX Cap	RV	67.83	11.1	12.1	2.10	0.09
V532 Sgr	CWA	68.97	12.7	13.5	3.04	0.17
NW Tel	RVA	68.99	11.1	11.9	1.99	0.12
R Sge	RVB	71.15	8.9	9.7	2.08	0.70
ASAS 160723-2957.2	CW-FU	74.13	12.6	13.5	2.84	0.14
V1004 Sgr	CWA	75.12	12.4	13.0	3.27	0.20
AC Her	RVA	75.36	7.3	8.3	2.30	0.26
V729 Ara	SR	75.91	10.2	11.3	3.59	0.53
V Vul	RVA	76.09	8.1	9.5	2.62	0.62
RT Ara	SRD	76.63	10.3	11.1	2.00	0.08
DS Aqr	RVA	77.50	10.3	11.2	1.39	0.11
RV Tau	RVB	78.43	9.3	10.6	4.30	0.71
V385 CrA	RV	78.60	11.1	12.2	2.36	0.16
V1284 Sgr	RV:	80.03	12.1	12.8	3.73	0.38
V1009 Sgr	RVA	80.95	12.5	13.2	3.04	0.32
V453 Oph	RVA	81.19	10.4	11.5	2.35	0.16
V1864 Sgr	RV	81.71	11.8	12.3	1.99	0.26

(Table 1 continued on following page)

Table 1. Stars with CWA- or RVA-like light curves in the ASAS-3 data, continued.

Name	Type	Period (d)	V_{max}	V_{min}	V–H	H–K_s
AR Sgr	RVA	86.76	9.1	10.3	1.59	0.27
UZ Oph	RVA	87.57	10.1	12.2	2.81	0.15
SS Gem	RVA	89.83	8.6	9.5	2.59	0.19
U Mon	RVB	91.36	5.8	7.1	2.04	0.23
V1833 Sgr	CWA	97.23	12.1	13.3	3.17	0.17
LR Sco	SRD	101.3	10.2	11.0	3.22	0.90
ET Vul	CWA	108.1	12.0	12.5	3.83	0.25
NSV 10164	RVA	110.8	10.0	12.0	2.98	0.25
AZ Sgr	RVA	111.2	10.8	11.5	2.26	0.15
V590 Aql	RVA	117.0	11.9	12.8	3.22	0.20
V691 Ara	RV:	129.7	11.6	12.1	3.36	0.18
QV Aql	RV	130.6	11.4	12.2	3.58	0.16
V411 Sco	RV	133.3	12.5	13.1	3.13	0.22
TX Oph	RVA	134.1	9.9	11.1	2.42	0.21
NSV 7708	I	135.2	11.2	11.6	2.90	0.70
RY Ara	RV	144.0	8.8	10.9	2.82	0.25
QT CrA	SRD:	158.8	10.4	11.2	3.26	0.17
V820 Cen	RV	159.7	8.6	9.5	2.73	0.17
GSC 7735-1239		160.8	12.9	13.6	3.50	0.24
BU Cen	RV:	169.0	10.4	11.3	3.26	0.18
V794 Sgr	RV	172.3	11.0	13.6	5.74	0.39
CK Vir	SRD	177.9	10.1	10.7	3.02	0.21
AT Del	SRD:	225.3	11.3	12.7	4.30	0.25
UY CMa	SRD	227.0	10.5	11.5	2.34	0.61
V3955 Sgr	SRD	240.5	9.9	11.1	3.84	0.29

Figure 1 *(on following pages).* Phase plots for CWA and RVA variables from ASAS-3 data, arranged by period (defined in the RVA sense with two maxima per cycle). The heading for each plot lists the name, period, and the GCVS type, when available, of the star. Tick marks on the vertical axis are separated by 0.1 magnitude.
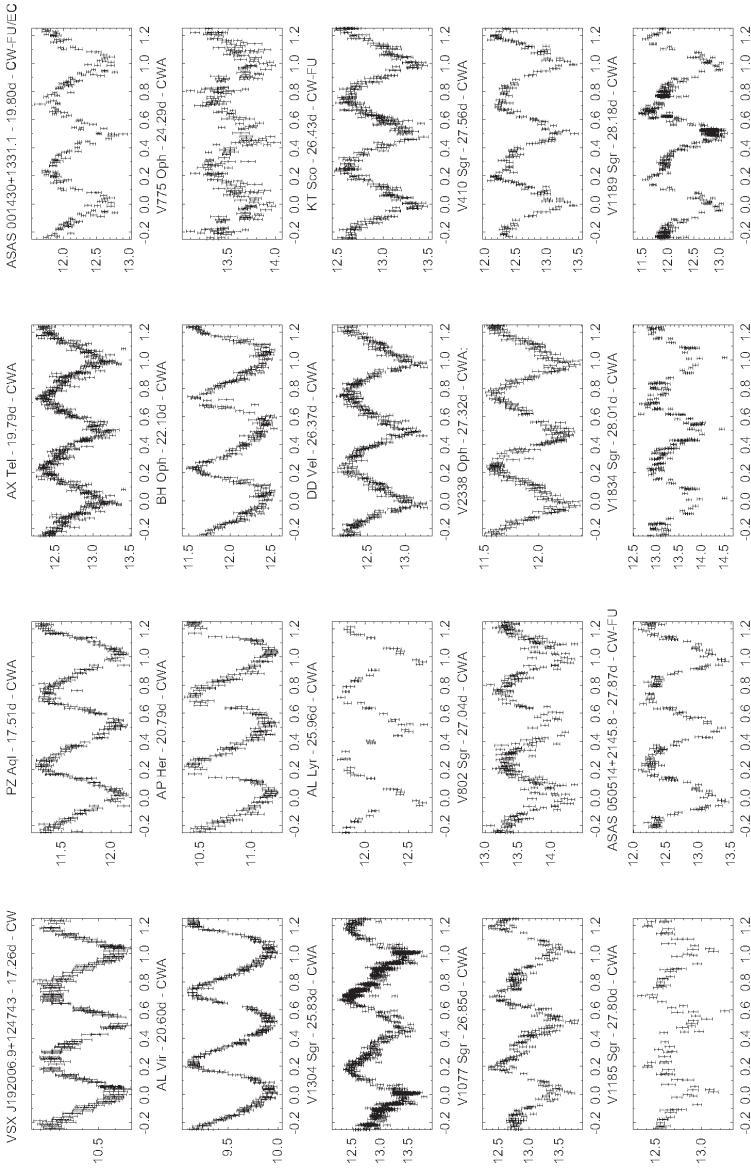
Figure 1. Phase plots for CWA and RVA variables from ASAS-3 data, arranged by period. *(Figure continued on following pages.)*
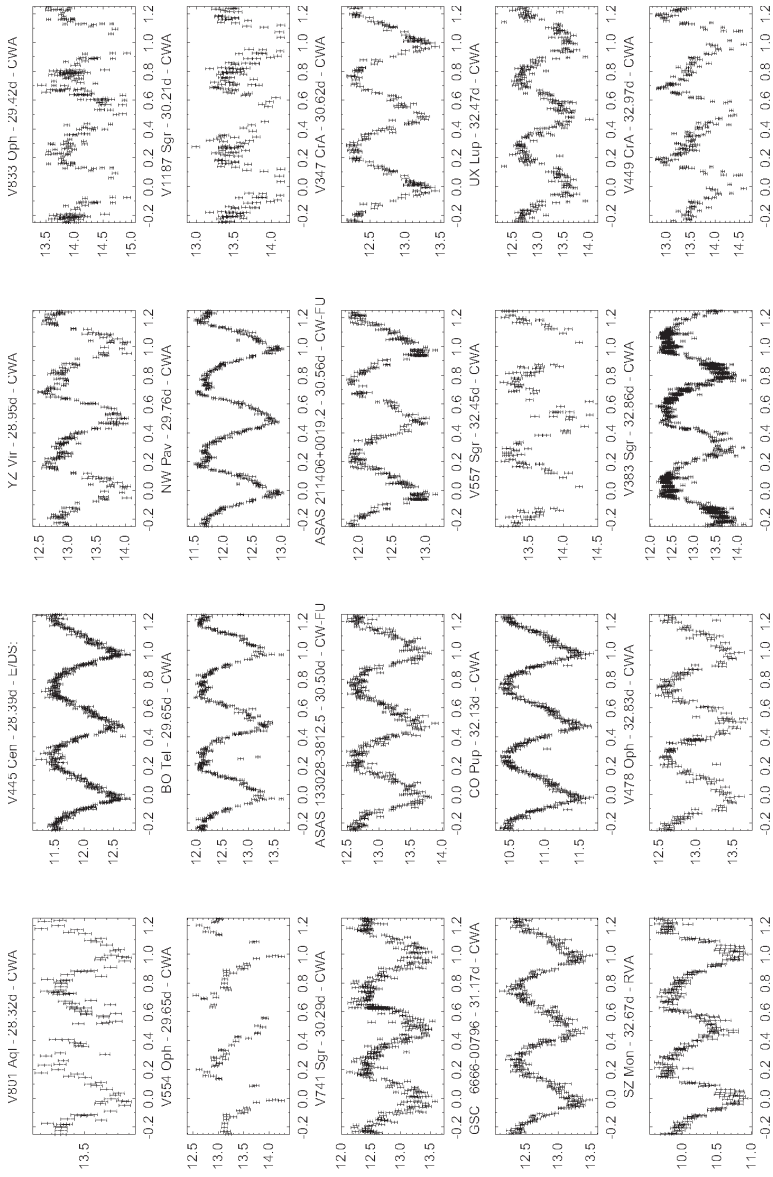
Figure 1, continued. Phase plots for CWA and RVA variables from ASAS-3 data. (*Continued on following pages.*)

Figure 1, continued. Phase plots for CWA and RVA variables from ASAS-3 data. (*Continued on following pages.*)
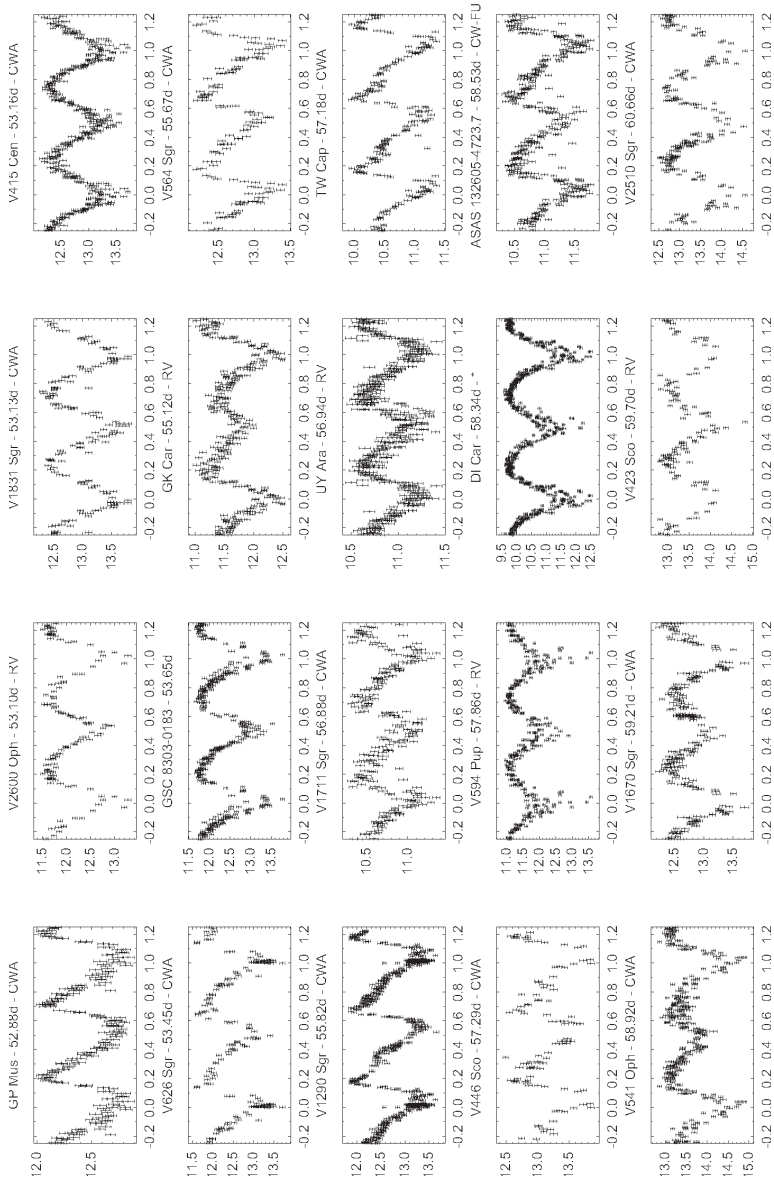
Figure 1, continued. Phase plots for CWA and RVA variables from ASAS-3 data. (*Continued on following pages.*)
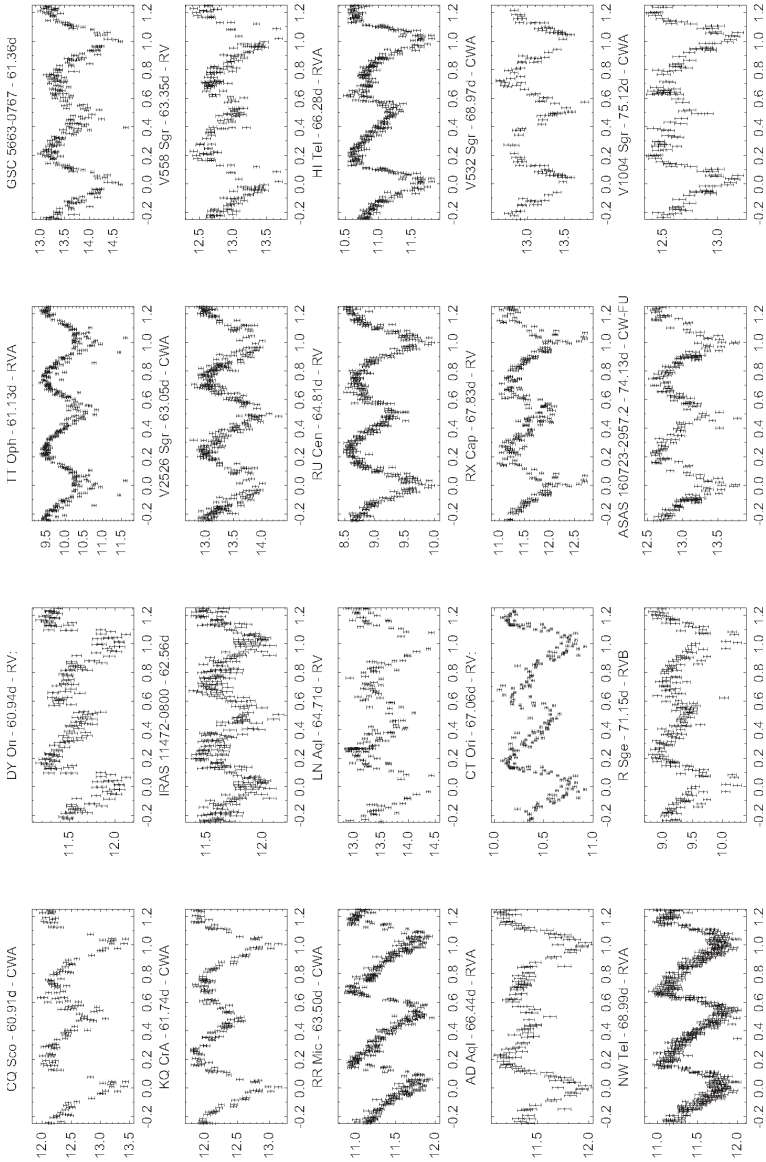
Figure 1, continued. Phase plots for CWA and RVA variables from ASAS-3 data. *(Continued on following pages.)*

Figure 1, continued. Phase plots for CWA and RVA variables from ASAS-3 data. (*Continued on following page.*)
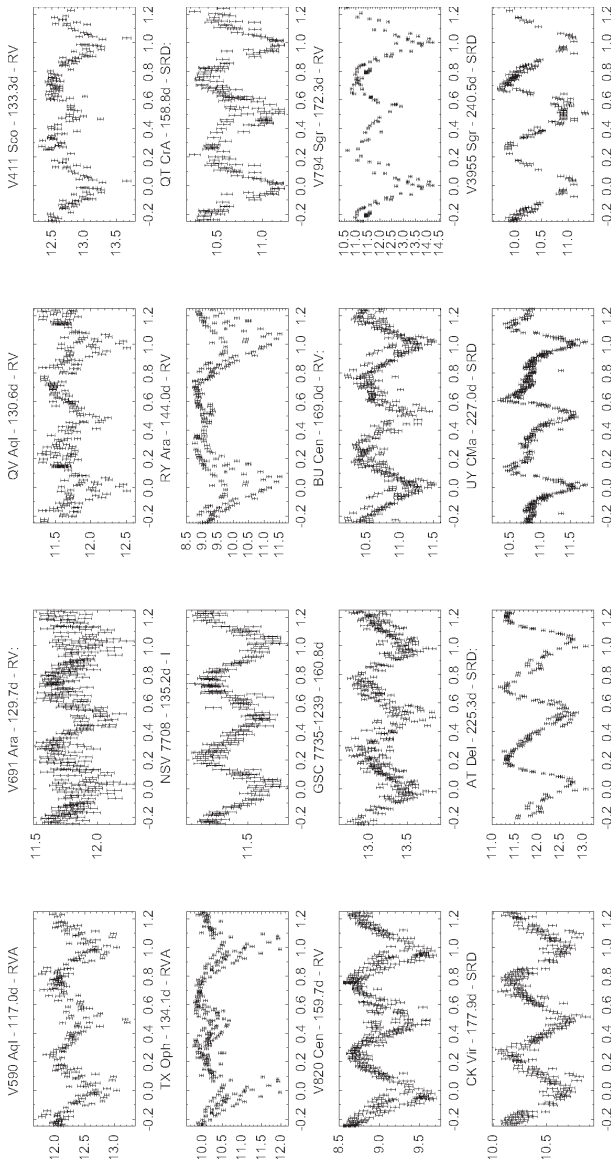
Figure 1, continued. Phase plots for CWA and RVA variables from ASAS-3 data.
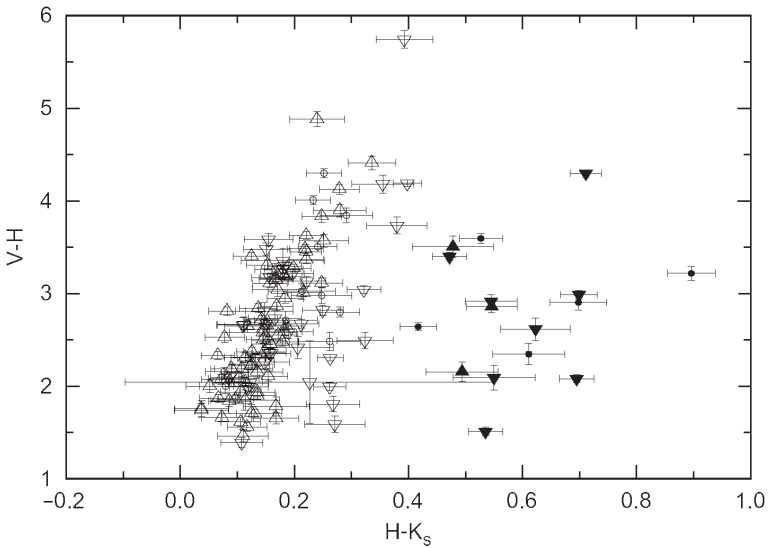
Figure 2. *V–H* plotted against *H–K$_s$* for the stars in Figure 1. Stars classified before as CW are plotted as triangles pointing upwards and those classified as RV as triangles pointing downwards. Stars not classified before or classified differently are plotted as small circles. The stars with *H–K$_s$* < 0.4 are plotted with open symbols, those with *H–K$_s$* > 0.4 with filled symbols.
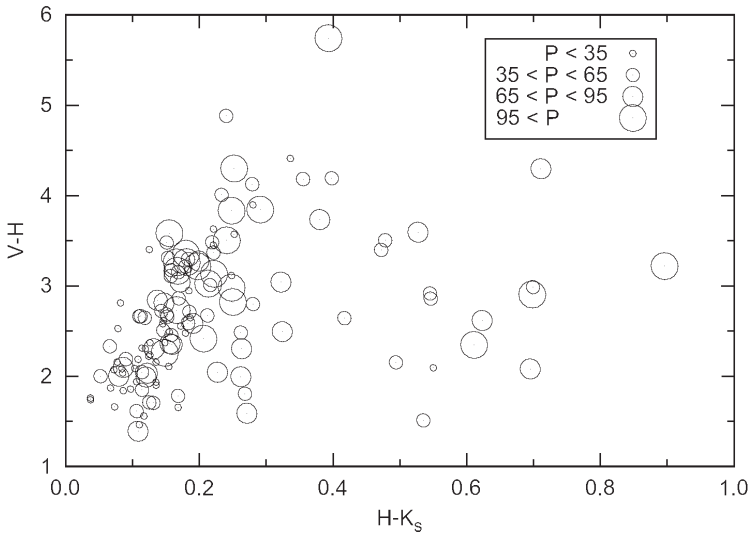
Figure 3. Same as Figure 2, but this time with the size of the symbols depending on the period.

Studying Variable Stars Discovered Through Exoplanet-Transit Surveys: A "Research Opportunity Program" Project

John R. Percy
Rahul Chandra
Mario Napoleone

Department of Astronomy and Astrophysics, University of Toronto, Toronto ON, M5S 3H4, Canada

Abstract   We discuss the study and classification of variable stars discovered as a by-product of searches for exoplanet transits—slight dimmings of stars by planets in orbit around them. We describe two specific projects carried out by undergraduate students in the University of Toronto's Research Opportunity Program. We discuss the nature of this program, in which second-year (sophomore) students can complete a research project for course credit.

1. Introduction

Extra-solar planets (exoplanets) are planets around stars other than the sun. As of September 2007, 212 exoplanets had been discovered since the first one was found in 1995 (see the website http://exoplanets.org). Almost all have been discovered through their gravitational effect on their star. The star moves in a small orbit with the same period as the planet. The star's orbital motion is detected by the precision radial velocity technique, developed by Campbell, Walker, and Yang (1988) among others.

Many of the exoplanets so far discovered orbit close to their star, and this increases the probability that a distant observer will observe a transit of the exoplanet across the face of the star, which decreases the brightness of the star—typically by one percent or less. Exoplanet transits have been used to study the properties of the planets; from them, the mass can be determined unambiguously, along with the radius and therefore the mean density. Several groups are also conducting exoplanet transit surveys as a way to discover additional exoplanets. Two such projects are EXPLORE and STARE.

2. EXPLORE

The EXPLORE (EXtra-solar PLanet Occultation REsearch) project is a transit search project carried out using wide-field CCD imaging cameras on 4-m class telescopes, and 8–10-m class telescopes for precision radial

velocity verification of the photometric candidates (Mallén-Ornelas *et al.* 2003; EXPLORE 2007). Data were obtained in four filters: I_c, R_c, *V*, and *B*. The nightly datasets were typically 0.3–0.4 day long. The stars are typically 20th magnitude. An important feature of this project is the high photometric precision (up to 2 millimag) and high rate of time sampling (every few minutes), implemented with an efficient pipeline enabling rapid follow-up of promising candidates. See von Braun *et al.* (2005) for some recent results.

3. STARE

Unlike the EXPLORE project, the STARE project (*ST*ellar *A*strophysics & *R*esearch on *E*xoplanets) uses a relatively small telescope—a 10-cm Schmidt telescope. The telescope typically images an area of sky six degrees on a side (STARE 2007). Most of the target stars are of magnitude 10–12, and are measured in three photometric bands: *B*, *V*, and *R*. In 2001, STARE moved from a location in Boulder, Colorado, to a new home on the island of Tenerife. The STARE project subsequently joined with two other projects—using even smaller telescopes—to form the TrES (Trans-Atlantic Exoplanet Survey) network, which subsequently discovered its first exoplanet in 2004. See Rabus *et al.* (2007) for some recent results.

4. By-products of exoplanet transit surveys

Because the probability of discovering an exoplanet transit is so small, these surveys must image tens of thousands of stars every few minutes over many days or weeks. A significant fraction of the imaged stars are variable for reasons other than an exoplanet transit, and most of these variable stars are new discoveries. They potentially provide astronomers with large homogeneous surveys of variable stars, as well as with the possibility of discovering individual variable stars that are unique and/or important, and worthy of further study. The present project deals with the study and classification of these variable stars.

The specific objective of the two studies described in this paper was to see whether the classification of the newly discovered variable stars could be improved by using self-correlation (Percy and Mohammed 2004, and references therein) as an adjunct to Fourier analysis. We have found self-correlation to be useful in distinguishing between possible periods in the Fourier spectrum when several alias periods are present. The correct period, and the corresponding phase curve, along with color information, can then be used to classify the variable. This can be done in theory, at least: in practice, it is not always possible to classify the variable unambiguously; students learn that scientific research is not always cut-and-dried!

An equally important objective was to provide the students with a meaningful structured research experience that introduced them to research skills, and to research data that required them to use their skills to produce new research results.

5. Research opportunity program

Undergraduate research should be an increasing priority for research universities in North America (Boyer Commission 1988), and many universities, including our own, are following this recommendation. It not only gives students a wide range of research skills, and other academic skills, but it also gives students a sense of "engagement" with both their subject of study and with their instructors. It is already an important part of the curriculum in many four-year undergraduate colleges in the U.S., and that is one reason why these colleges are very successful in preparing students for graduate and professional schools, as well as for the workplace. Regrettably, we have very few such colleges in Canada. In the sciences, undergraduate research is supported in the U.S. by the Research Experiences for Undergraduates (REU) program of the National Science Foundation.

At the University of Toronto, undergraduate research is carried out through several programs which are typical of programs elsewhere—a fourth-year project or "senior thesis" course, summer research assistantships (many funded through the Natural Sciences and Engineering Research Council—our equivalent of NSF), and the work-study program which provides career-related government-funded positions to eligible students during the academic year. There is also the University of Toronto Mentorship Program, that enables outstanding senior high school students to work on research projects at the university. These high school students are comparable, in ability, with undergraduates, and the Mentorship Program is excellent preparation for further research experiences when the students reach university.

In the present paper, we describe research that was carried out within the Research Opportunity Program (ROP), which is different from the programs mentioned above. This program provides an opportunity for students in their second year of study (sophomores) to earn a full course credit (one-fifth of a full load) by participating in a faculty member's research project. Students apply, and are interviewed in the spring of the previous year. Because there are relatively few ROP positions available, the ROP is competitive and prestigious.

My goal is for the student to carry out an original, self-contained project that can be presented at a conference and/or published in a journal (here it is!). Most students have not taken an astronomy course in their first year, so I provide a structured experience, with weekly meetings, that leads the students to the deliverables on which they are evaluated:

   • Reading about stars, stellar evolution, and variable stars (the AAVSO website is exceptionally useful for this); understanding the algorithms and software that they will use; understanding the datasets that they will use, and how they "interact" with the software; testing the software with standard datasets, etc.

• Progress report submitted in January; since most students have never written such a report, I read and comment on a first draft; the second draft is evaluated.

• First results, generally obtained in December-January.

• A non-technical poster for the Faculty-wide "Research Fair" in February (Figure 1).

• Completion of the project, leading to a project report; again, I read and comment on a first draft; the second draft is evaluated.

• An interview about the report, to test the depth of the student's understanding of all aspects of the project.

• A journal recording their progress and reflections on their experience.

For me, the Research Fair is a highlight of the year. It not only showcases the students' work, but it also brings me and my students into contact with professors and students from across the Faculty of Arts and Science. We see the full range of research strategies and techniques in the humanities and social sciences, as well as in the physical, mathematical, and life sciences. We see the creativity of professors who have found a wealth of ways to engage undergraduates in their scholarship and research.

6. The EXPLORE project: Rahul Chandra

Rahul Chandra examined in detail seventeen short-period variable stars that had been analyzed, using Fourier and phase dispersion minimization techniques, by Clement *et al.* (2006) and Nguyen *et al.* (2006). These members of the EXPLORE collaboration identified about 80,000 stars in a Galactic plane field, analyzed the observations of about 5,500 of these on a total of 1,950 frames, and discovered twenty-three new variable stars. The seventeen stars analyzed were listed as "additional variable stars"; no classification was suggested.

Chandra used the additional technique of self-correlation to complement the other two techniques. The following example, also shown in the accompanying figures, illustrates the nature of the project:

Star 1515-1 has a Fourier peak at 0.39965... cycle/day (a period of about 2.5 days), and two others that are almost as high (Figure 2); the self-correlation diagram (Figure 3) shows that this 0.4 cycle/day peak is clearly the correct one because there are minima at multiples of this value. There is no evidence for alternating deep and shallow minima such as would be found in an ellipsoidal variable, for instance. These would be apparent from the self-correlation diagram. Clement *et al.* (2006) and Nguyen *et al.* (2006) obtained a period of 2.519446 days, and an amplitude of 0.078 in I_c, and the amplitude that we

derive is consistent with this value. The $(V–I_c)$ color is 2.10, which corresponds to a late K or early M star but, given that this is a 20th-magnitude star that could be reddened, it could be almost any kind of periodic variable.

7. The STARE project: Mario Napoleone

Napoleone's project was atypical, within my ROP experience, in the sense that he independently came up with the project during the preceding summer. Normally, I prepare a list of possible projects, and present this to the student, along with some recommendations.

Napoleone carried out Fourier, self-correlation, and phase-diagram analysis on 146 stars in the AUR0 list (STARE 2007), for which periods had been determined by Fourier analysis, and classifications had been suggested by the STARE team. Phase diagrams can be useful for identifying stars with alternating deep and shallow minima, such as ellipsoidal variables, and variables with non-sinusoidal light curves. Classification was confirmed on about seventy stars using all three techniques. Self-correlation proved inconclusive on about sixty stars, but the other two techniques supported their classification. Self-correlation gave marginal confirmation on ten stars, but the other two techniques supported their period and hence their classification. Two stars showed very confusing results using all three techniques. The following example, also shown in the accompanying figures, illustrates the nature of the project.

Star AUR0-3355 has a Fourier peak at 3.4 days, along with alias peaks (Figure 4); the 3.4-day peak is confirmed by self-correlation analysis; there are minima at integral multiples of this value (Figure 5). The peak-to-peak amplitude is 0.080 magnitude. The phase curve is approximately sinusoidal, and there is no evidence for alternating deep and shallow minima. The STARE classification of γ Doradus seems doubtful, given the long period of the star; γ Doradus stars normally have periods of 1 to 3 days. It may be a rotating variable.

8. Discussion and conclusions

For several stars in these two surveys, self-correlation analysis provided more secure identification of the period of the star. In most cases, it did not provide any significant additional information.

Both studies point out the value of having additional information about the newly-discovered variable stars, such as spectral type or color, to aid in classification, though, if the stars are faint and heavily reddened, it is sometimes difficult to determine their intrinsic properties. Such information is available for both these surveys, but the classification may still be ambiguous. If the classification must be done solely on the basis of period, however, self-correlation analysis provides a useful adjunct to Fourier and phase-diagram analysis, especially when there are alias peaks in the Fourier spectrum.

Both Chandra and Napoleone received enriching educational experiences. They learned a branch of astronomy in some detail. They were exposed to real datasets, and research-grade techniques of time-series analysis. They learned to make judgments about classification, often on the basis of less-than-ideal data. They received guidance and experience in various forms of scientific communication.

There are also large-scale surveys for other kinds of variable objects, such as gravitational microlenses, and optical counterparts of gamma-ray bursts that also yield large numbers of new variable stars. The considerations outlined in this paper apply to them also.

The kind of research that is done by undergraduate students can also be done by skilled amateur astronomers. These individuals normally contribute to astronomical research through the measurements that they make, but they can help to analyze and interpret the vast amount of archival photometric data that is available. A book, specifically targeted to undergraduate student researchers, and skilled amateur astronomers, is now available (Percy 2007).

Hard copies of Chandra's and Napoleone's project reports can be obtained from John Percy: john.percy@utoronto.ca.

9. Acknowledgements

References

Boyer Commission 1988, http://naples.cc.sunysb.edu/Pres/Boyer.nsf

Campbell, B., Walker, G. A. H., and Yang, S. 1988, *Astrophys. J.*, **331**, 902.

Clement, C. M., Nguyen, D. C., Rucinski, S. M., Yee, H. K., Mallén-Ornelas, G., Gladders, M. D., and Seager, S. 2006, *Bull. Amer. Astron. Soc.*, **38**, 119 (Abstract #44.08).

EXPLORE 2007, http://www.dtm.ciw.edu/seager/EXPLORE/explore.htm

Mallén-Ornelas, G., Seager, S., Yee, H. K. C., Minniti, D., Gladders, M. D., Mallén-Fullerton, G. M., and Brown, T. M. 2003, *Astrophys. J.*, **582**, 1123.

Nguyen, D. C., Clement, C. M., Rucinski, S. M., Yee, H. K. C., Mallén-Ornelas, G., Gladders, M. D., and Seager, S. 2006, preprint, submitted to *Publ. Astron. Soc. Pacific*.

Percy, J. R. 2007, *Understanding Variable Stars*, Cambridge Univ. Press, New York.

Percy, J. R., and Mohammed, F. 2004, *J. Amer. Assoc. Var. Star Obs.*, **32**, 9.

Rabus, M., Brown, T. M., Deeg, H. J., Belmonte Avilés, J. A., Almenara Villa, J. M., and Alonso, R. 2007, in *Transiting Extrapolar Planets Workshop*, ASP Conference Series, **366**, 96.

STARE 2007, http://www.hao.ucar.edu/public/research/stare/stare.html

von Braun, K., Lee, B. L., Seager, S., Yee, H. K. C., Mallén-Ornelas, G., and Gladders, M. D. 2005, *Publ. Astron. Soc. Pacific*, **117**, 141.
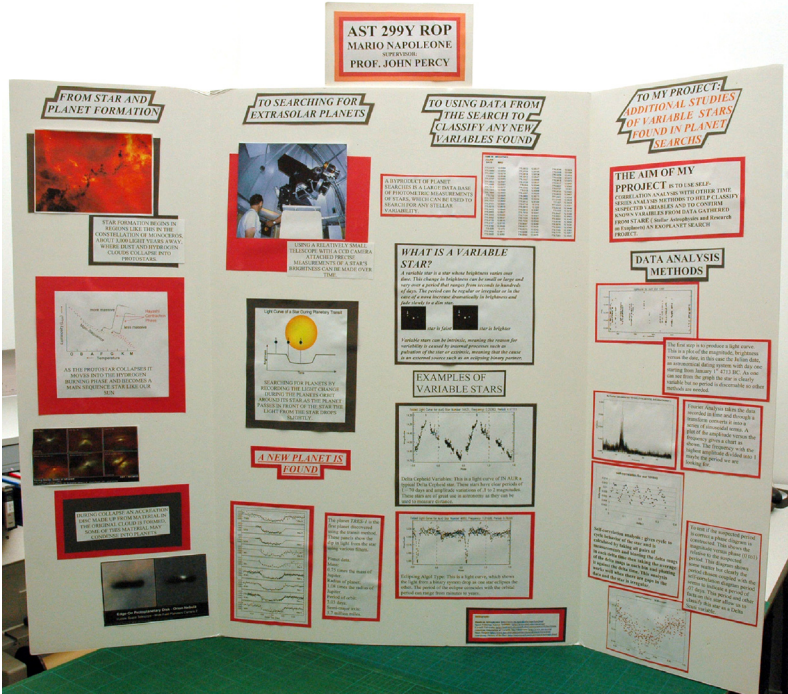
Figure 1. The ROP Research Fair. Students from across the Faculty of Arts and Science present poster papers about their research projects.
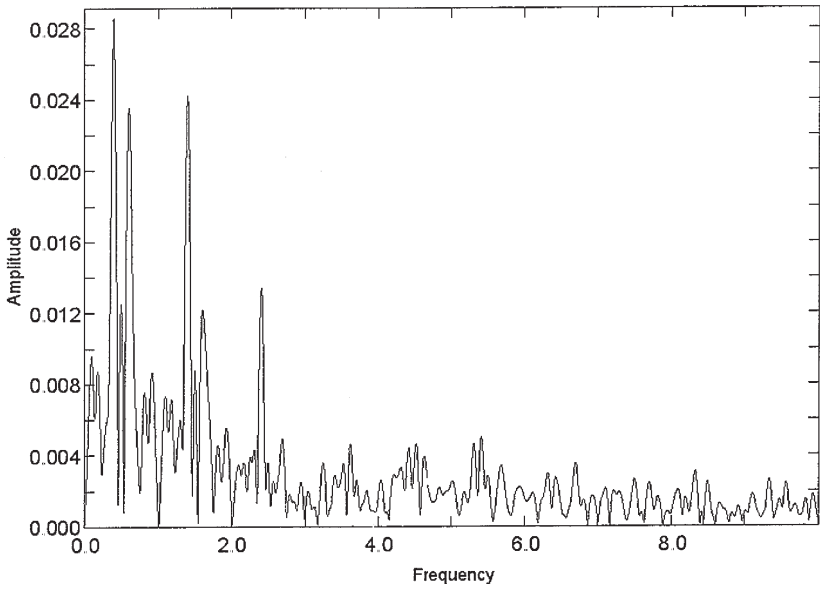
Figure 2. The Fourier spectrum of EXPLORE star 1515-1, showing a real peak (0.39965... cycle/day) peak and two alias peaks.
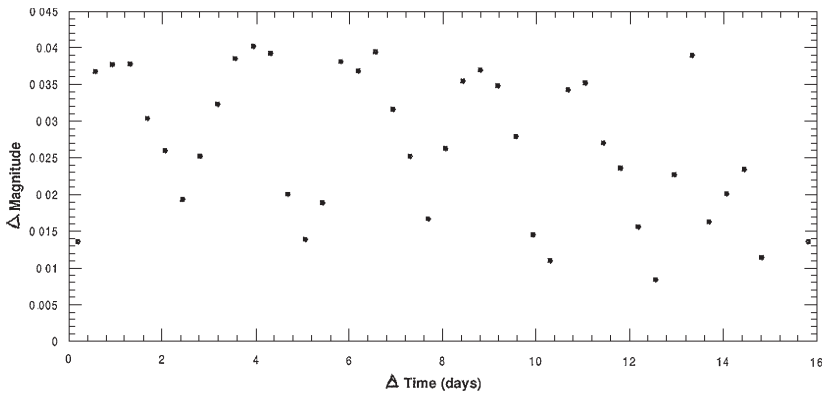
Figure 3. The self-correlation diagram of EXPLORE star 1515-1, showing minima at multiples of 2.50... days.
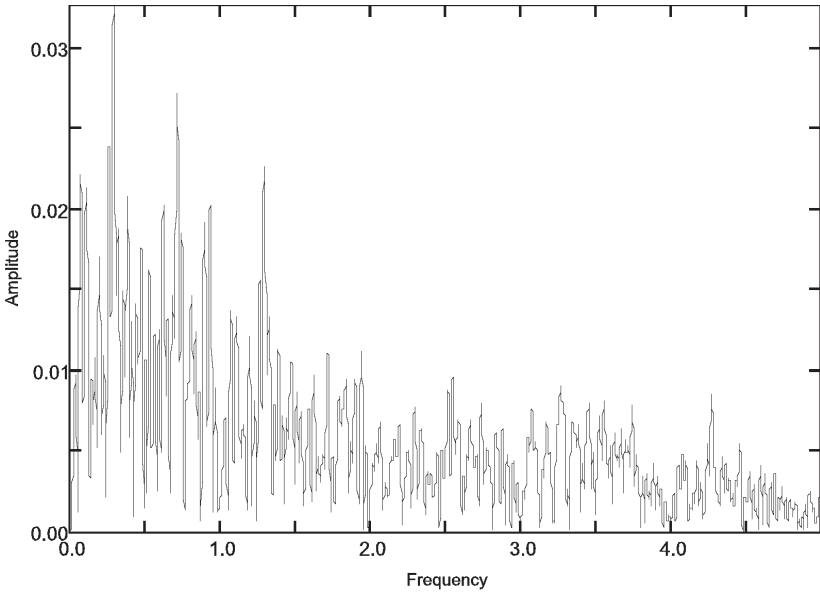
Figure 4. The Fourier spectrum of STARE star AUR0-3355, showing a real peak (0.29... cycle/day) and several alias peaks.
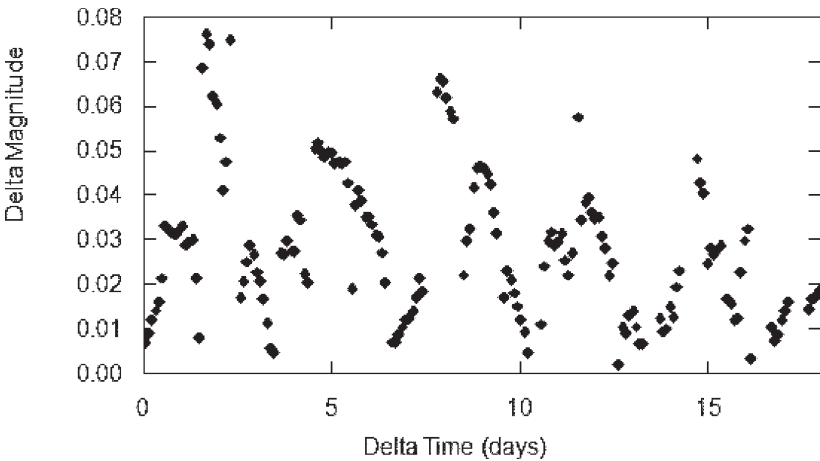
Figure 5. The self-correlation diagram of STARE star AUR0-3355, showing minima at multiples of 3.4... days. The diagram becomes somewhat scattered at values of Delta t for which there are very few Delta magnitudes.

Discovery and Observations of the Optical Afterglow of GRB 071010B

Arto Oksanen
Hankasalmi Observatory, Hankasalmi, Finland

Matthew Templeton
Arne A. Henden
AAVSO, 49 Bay State Road, Cambridge, MA 02138

David Alexander Kann
Thüringer Landessternwarte Tautenburg, Sternwarte 5, D-07778 Tautenburg, Germany

Abstract   On 2007 October 10 at 20:45:48 UT, the Swift satellite detected the bright, long-soft gamma-ray burst GRB 071010B in the constellation Ursa Major. Coordinates were automatically distributed via the Gamma-ray Burst Coordinate Network (GCN), and observations were begun by A. Oksanen at the Hankasalmi Observatory in Hankasalmi, Finland, within fifteen minutes of the burst. A previously uncatalogued optical source was detected at R.A. 10^h 02^m 09.26^s, Dec. +45° 43' 50.3" (J2000) at an unfiltered (*R*-band calibrated) magnitude of approximately 17.5. Imaging over the following six hours showed that the source faded, indicating that it was likely the optical afterglow of GRB 071010B. The discovery was published via the *GCN Circulars*, and the coordinates were subsequently used by other major telescope facilities to conduct follow-up photometry and spectroscopy.

The discovery of the optical afterglow by A. Oksanen is the first discovery of a GRB afterglow by an amateur astronomer since the discovery of GRB 030725 by L. A. G. Monard in 2003 (Monard 2003). The early detection of this afterglow and subsequent dissemination of coordinates via the GCN has proved very valuable from a scientific standpoint. These data are the earliest available photometry for this burst, enabling the study of the early stages of the GRB optical light. They were also the first localization, and these coordinates were subsequently used by other major optical facilities for their follow-up observations. This burst clearly shows that individual observers still have a role to play in GRB observations even in the era of automated, robotic telescopes, and that the amateur community is an important partner of the professional community in the observation of GRB afterglows.

1. Introduction

The Swift satellite (Gehrels *et al.* 2004) has been a prolific source of GRB localizations over the past three years of its operation; over 150 bursts have been detected and localized in gamma-rays, X-rays, and/or optically by the satellite itself, and the high-energy localizations provided in real-time by Swift have enabled ground-based follow-ups of many of these GRBs. The AAVSO International High Energy Network (AAVSO HEN) grew from the AAVSO International GRB Network, formed in April 2000 as a link between the amateur observer community and the wider gamma-ray burst research community. It has since grown into an organized observing program within the AAVSO that provides GRB localizations from Swift and other satellites, along with a mechanism for sharing information among network members and publishing observations via the *GCN Circular*. The rapid distribution of satellite localizations has been key to amateur participation in GRB observations, just as it has been in professional GRB research.

In principle, GRB fields can be imaged within seconds of detection of the gamma- rays, so long as the observer is in darkness, and can view the field from their location; GCN localizations are used by all ground-based rapid follow-up projects, including robotic facilities (e.g. ROTSE-III) that can slew to target within seconds of receipt. Human-discovered afterglows with 0.5-meter aperture telescopes and smaller have become very rare, given the near-instantaneous response of robotic systems that respond directly to GCN coordinates in real-time. However, robotic systems still have limitations; they may be in daylight or experiencing poor weather, or the coordinates may be inaccessible from the site. Thus human observers—particularly amateur GRB enthusiasts—still have an important role to play.

In this paper, we describe the discovery, observation, and subsequent analysis of GRB 071010B—the first GRB optical afterglow discovered by an amateur-astronomer since 2003. In Section 2, we describe the discovery and observations made by A. Oksanen along with the photometric reductions. In Section 3, we present our analysis of the light curve and compare these results to other published optical studies of GRB 071010B.

2. Observations

One of us (A. Oksanen) received the Swift gamma-ray localization for GRB 071010B (Markwardt *et al.* 2007) via the GCN, and within fifteen minutes began observations with the Hankasalmi Observatory RC Optical Systems 0.4-meter Richey-Chretien telescope. This telescope is mounted on a Paramount ME, and uses an SBIG STL-1001E CCD Camera with standard *BV RcIc* photometric filters. The majority of observations were made unfiltered, including the initial detection of the GRB. Sets of 10 × 60-second exposures were made in *V* and *Ic* following the initial detection, and were combined to obtain calibrated

photometry of the source; the remainder of the time-series observations were conducted unfiltered for the first night. The field was revisited again 2.2 days after the gamma-ray burst, and 40 × 120-second, unfiltered exposures were acquired.

The early observations beginning within fifteen minutes of the GRB detection are the only early-light optical data known to exist for GRB 071010B and provide an important photometric record of this burst. Although the source was below the pole and below the horizon of most observatories, the observer's high northern latitude enabled the prompt acquisition of the source. These circumstances were particularly fortunate for this burst, given that the Swift satellite had not yet been restored to full functionality following the 2007 August 11 gyroscope failure (see Gehrels 2007a, b), and thus the spacecraft did not autonomously slew to observe the field with UVOT.

The afterglow of GRB 071010B was clearly detected on the first night, and approximately six hours of unfiltered time-series data were obtained. The afterglow faded from an unfiltered (CR) magnitude of approximately 17.5 down to 19.0 over the course of six hours. The burst was again detected two days later, although it had faded to CR ~ 20.3 ± 0.1 and was too faint for time-series observations; the acquired frames were therefore averaged together. The results of the first night's observations were subsequently published in Oksanen (2007) and in Templeton *et al.* (2007).

For this paper, all images acquired by A. Oksanen were reanalyzed by A. Henden using point-spread function (PSF) fitting in IRAF. Calibration of the field was performed by A. Henden with the Sonoita Research Observatory 0.35-meter telescope in Arizona (Henden 2007). The early unfiltered images were photometered individually; the *V* and *Ic* images and later unfiltered images were stacked to improve the signal-to-noise. One image stack centered on JD 2454384.4882 was discarded due to severe interference from cosmic rays. The single data point obtained 2.2 days post burst was measured from a stack of images with total exposure time of 4,800 seconds. Table 1 gives the resulting photometry following reanalysis.

3. Analysis

We computed a best-fit power-law decay slope of the afterglow optical flux, $F \propto t^{\alpha}$:

$$\log F = \text{const} + \alpha \log (t - t_0), \tag{1}$$

where t_0 = JD 2454384.3651 (the time of the Swift detection of the GRB) and the constant is the flux predicted at $\log(t - t_0) = 0$ (or t_0 + 1 day). We fit three separate polynomials to these data: one to the earliest unfiltered data, taken within 0.05 day of the burst, and two to the later data. The two later-time fits were made to data that did and did not include the single observation made

two days later. The three fits are given in Table 2, and are shown along with the light curve in Figure 1.

These decay rates are different from the value of $\alpha = -0.482$ given in Templeton *et al.* (2007), primarily because the two epochs of unfiltered data were combined to compute a single power law for that paper. It is apparent from the current analysis that the data follow a broken power law. Both the early and late decay rates are significantly different from one another, indicating that there were significant physical changes occurring during each epoch of the decay. We note that there is some evidence for a flare around $t-t_0 = 0.02$ day, but this is based on a single data point and thus not confirmed. The slope we obtain for our late-time unfiltered observations (about $\alpha = -0.53$ for both the short and longer data sets) is similar to $\alpha = -0.56$ derived by Kann *et al.* (2007b) using a combined data set from the Hankasalmi (Oksanen 2007), Mount Lemmon (Im *et al.* 2007) and TLS Tautenburg 1.34-meter (Kann *et al.* 2007a) telescopes. The Kann *et al.* (2007b) fit includes more late-time data, and is thus consistent with the fit to the "late (long)" data being slightly steeper; the physical properties of the light source may have been evolving through this later stage even up to the second break. An analysis of all available photometry is currently in progress (Kann *et al.* 2008, in preparation).

4. Discussion

The localization and light curve of GRB 071010B obtained with the Hankasalmi telescope provided the wider GRB community with important data on this GRB, and facilitated the study of this burst by other major telescopes, including spectroscopic observations by Gemini North (Cenko *et al.* 2007) and Keck (Prochaska *et al.* 2007; Stern *et al.* 2007) that have established a redshift of $z \sim 0.947$ for the burst and host galaxy. Although GRB 071010B likely would have been localized by any of several other telescopes that subsequently made optical observations, the data presented in this paper are the earliest photometry available for this burst from any facility, and they provide unique information on the early evolution of the optical afterglow that will be important in future physical studies of this bright GRB.

Manually-controlled amateur and smaller professional telescopes continue to provide important data and upper limits to several GRBs per year, both through AAVSO HEN and independently via the *GCN Circular*s. Robotic telescopes devoted solely to GRB followups clearly have an advantage over human beings in the early detection of GRB afterglows, but even in this task they are not guaranteed to detect every burst on the sky. The number of robotic facilities is growing, but they do not have sufficient global coverage to guarantee a clear view of the entire sky at all times. There is an element of serendipity in amateur detections of GRB afterglows, but as this work makes clear, there is still the possibility for unique and important amateur contributions to the field of GRB research.

5. Acknowledgement

The AAVSO thanks the Curry Foundation for its continued support of the AAVSO High Energy Network.

References

Cenko, S. B., Cucchiara, A., Fox, D. B., Berger, E., and Price, P. A. 2007, *GCN Circular*, No. 6888.
Gehrels, N. 2007a, *GCN Circular*, No. 6760.
Gehrels, N. 2007b, *GCN Circular*, No. 6946.
Gehrels, N. *et al.* 2004, *Astrophys, J.*, **611**, 1005.
Henden, A. 2007, *GCN Circular*, No. 6909.
Kann, D. A., Hoegner, C., and Filgas, R. 2007a, *GCN Circular*, No. 6918.
Kann, D. A. *et al.* 2007b, *GCN Circular*, No. 6935.
Kann, D. A. *et al.*, 2008, in preparation.
Im, M., Lee, I., and Urata, Y. 2007, *GCN Circular*, No. 6897.
Markwardt, C. B., *et al.* 2007, *GCN Circular*, No. 6871.
Monard, B. 2003, *GCN Circular*, No. 2324.
Oksanen, A. 2007, *GCN Circular*, No. 6873.
Prochaska, J. X., Perley, D. A., Modjaz, M., Bloom, J. S., and Poznanski, D. 2007, *GCN Circular*, No. 6890.
Stern, D., Perley, D. A., Reddy, N., Prochaska, J. X., Spinrad, H., and Dickinson, M. 2007, *GCN Circular*, No. 6928.
Templeton, M., Kann, D. A., Oksanen, A., and Henden, A. 2007, *GCN Circular*, No. 6903.

Table 1. Photometry of GRB 071010B obtained with the Hankasalmi Observatory 0.4-meter telescope. Observations by A. Oksanen; photometry by A. Henden.

HJD	magnitude	err(mag.)	filter	n_{comp}	n_{stack}
2454384.3744	17.468	0.044	CR	10	$1 \times 60s$
2454384.3757	17.510	0.054	CR	10	$1 \times 60s$
2454384.3769	17.536	0.048	CR	10	$1 \times 60s$
2454384.3781	17.607	0.052	CR	10	$1 \times 60s$
2454384.3793	17.673	0.069	CR	10	$1 \times 60s$
2454384.3806	17.649	0.057	CR	10	$1 \times 60s$
2454384.3818	17.800	0.075	CR	10	$1 \times 60s$
2454384.3831	17.785	0.069	CR	10	$1 \times 60s$
2454384.3844	17.638	0.069	CR	10	$1 \times 60s$
2454384.3876	17.537	0.093	I	10	$5 \times 60s$
2454384.3954	17.781	0.109	I	10	$5 \times 60s$
2454384.4028	18.296	0.083	V	10	$5 \times 60s$
2454384.4091	18.324	0.061	V	9	$5 \times 60s$
2454384.4191	18.154	0.030	CR	8	$3 \times 120s$
2454384.4262	18.248	0.037	CR	9	$3 \times 120s$
2454384.4322	18.239	0.025	CR	8	$3 \times 120s$
2454384.4382	18.320	0.033	CR	9	$3 \times 120s$
2454384.4443	18.383	0.028	CR	9	$3 \times 120s$
2454384.4504	18.383	0.030	CR	9	$3 \times 120s$
2454384.4580	18.413	0.027	CR	9	$5 \times 120s$
2454384.4683	18.461	0.028	CR	9	$5 \times 120s$
2454384.4782	18.506	0.037	CR	9	$5 \times 120s$
2454384.4998	18.630	0.025	CR	8	$7 \times 120s$
2454384.5139	18.681	0.027	CR	9	$7 \times 120s$
2454384.5279	18.748	0.026	CR	9	$7 \times 120s$
2454384.5421	18.797	0.033	CR	9	$7 \times 120s$
2454384.5584	18.800	0.035	CR	9	$10 \times 120s$
2454384.5784	18.928	0.027	CR	9	$10 \times 120s$
2454384.5988	18.984	0.026	CR	9	$10 \times 120s$
2454384.6189	19.028	0.038	CR	9	$10 \times 120s$
2454386.5660	20.458	0.082	CR	9	$40 \times 120s$

Table 2. Flux decay rate of GRB 071010B as a function of time. The notation "late (long/short)" indicates the lightcurve (does/does not) include data taken two days post-burst. The flux constants have been converted back to their corresponding CR magnitudes predicted at $t = t_0 + 1$ day.

time	$m_{CR}(t_0 + 1d)$	α	*reduced* χ_z^2
early	19.30 ± 5	-0.36 ± 1	0.88
late (short)	19.767 ± 5	-0.516 ± 1	0.90
late (long)	19.810 ± 5	-0.534 ± 1	1.28
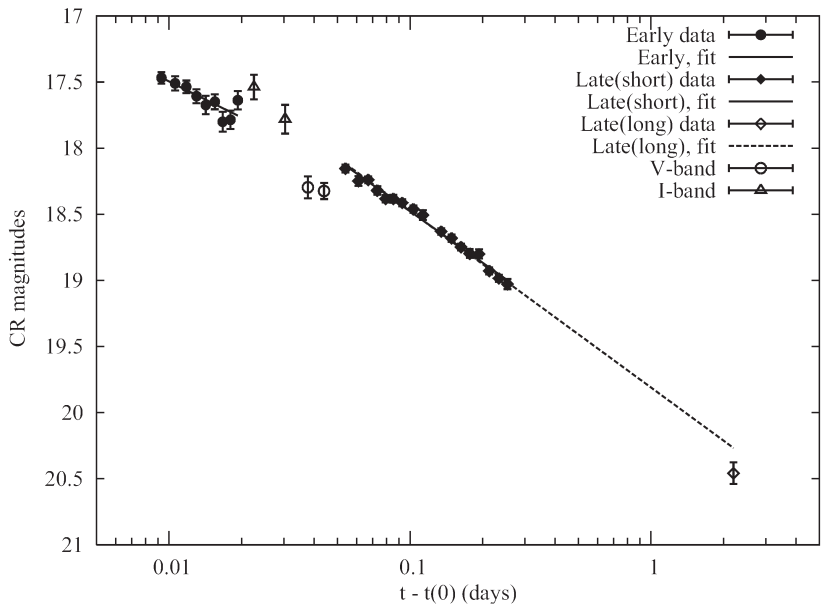
Figure 1. Light curve of GRB 071010B obtained at Hankasalmi Observatory. The majority of data are unfiltered (CR) magnitudes, with two *V* and *Ic* observations. The fits given in Table 2 are shown by the solid and dotted lines.

Detection of the First Observed Outburst of DW Cancri

Tim Crawford
Arch Cape Observatory, 79916 W. Beach Road, Arch Cape, OR 97102

David Boyd
5 Silver Lane, West Challow, Wantage, OX12 9TX, UK

Carlo Gualdoni
22100 Como, Italy

Tomas Gomez
Lira 8, 6-A, 28007 Madrid, Spain

Walter MacDonald II
P.O. Box142, Winchester, ON K0C 2K0, Canada

Arto Oksanen
Verkkoniementie 30, FI-40950 Muurame, Finland

Abstract   Using data gathered by amateur astronomers from several nations, as reported to the American Association of Variable Star Observers (AAVSO), the first observed outburst of the intermediate polar DW Cancri was detected on January 25, 2007, at magnitude *V* ~11.36. This represented a brightening of ~4 magnitudes from both recent measurements and long term average quiescence. The outburst was of a relatively short duration, as measured from the first detection of the outburst, showing a fading of ~2.25 magnitudes in ~27 hours, and another ~1.25 magnitudes within the next ~30 hours. Follow up photometric observations show the asynchronous rotation period of the magnetic white dwarf star of this system to be 38.6 minutes, in agreement with previous studies; a strong secondary signal of ~73.7 minutes was also noted. As to whether or not the outburst was the result of disk instabilities or caused by a mass transfer event, no conclusion could be reached.

1. Introduction

Sterken and Jascheck (1996) identified Intermediate Polar (IP or DQ Her) systems as containing a non-synchronously rotating magnetized white dwarf with a cool companion (near the main sequence). These high mass transfer systems have an accretion disk near the white dwarf whose accretion activity is disrupted by the magnetic field of the white dwarf as it flows towards the magnetic poles from the accretion disk; variations in the brightness of this

activity are caused by a combination of eclipsing and rotationally modulated accretion effects.

While Kholopov *et al.* (1981) gave this star its GCVS name of DW Cnc, Stepanian (1982) was the first to suggest that DW Cnc (R.A. 07^h 58^m 53.07^s, Dec. $+16°$ 49' 26.2" (J2000)) is a dwarf nova, on the basis of its blue color and *V* magnitude variations from 15 to 17.5.

Patterson *et al.* (2004) provide an overall review of this intermediate polar. The time-series photometry in their study showed two periodic signals, over the course of a one-year baseline of measurement, of 38.6 and 69.9 minutes. The spectroscopic study detected a period of 86.1 minutes. The authors interpreted the 86.1-minute signal to be the orbital period of the binary (P_{orb}) and the 38.6-minute signal to be the spin period of the magnetic white dwarf (P_{spin}). The analysis further showed that the 69.9-minute signal was a spin-orbital beat period (lower orbital sideband) through the relationship of $1/69.9 = (1/38.6)–(1/86.1)$ within the limits of their measurements.

Rodríguez-Gil *et al.* (2004) noted that DW Cnc had yet to be observed undergoing an outburst (~8 years of monitoring) and that the normal range of the magnitude variations was between *V* ~14 and *V* ~15 with occasional low states ~2 magnitudes fainter.

Here we present photometry showing the first observed outburst of DW Cnc on January 25, 2007, as well as follow-up observations showing the asynchronous rotation period of the magnetic white dwarf star of this system, with additional data analysis showing a strong secondary period signal.

2. Observations

All data are from the AAVSO International Database and *V* filter with the exception of Boyd's data from February 5 and 6, 2007, which were unfiltered. Table 1 lists the equipment used by the authors.

The most recent observation of DW Cnc (within the AAVSO database) prior to the detected outburst occurred on 2007 January 21.317 UT, and was measured by MacDonald (Canada) at a magnitude *V* = 15.29. The closest previous observation to that date was on 2007 January 13.0578 UT and measured by Gualdoni (Italy) at magnitude *V* = 15.21. Gomez (Spain) measured DW Cnc at *V* = 15.48 on 2006 December 25.9913 UT.

The first observed outburst of DW Cnc was detected by MacDonald on 2007 January 25.2970 UT at *V* ~11.36; the variable was noted as being saturated in the image which places a lower limit on the brightness (just the variable was saturated, not the comparison stars, and MacDonald had to be urged to post his observation, even if the photometry was suspect once the importance of his image became more apparent). The first follow-up detections were by Crawford (USA) on 2007 January 26.4333 UT, where DW Cnc had already faded to an average magnitude *V* = 13.56, and Gualdoni (26.9839 UT) with magnitude *V* = 13.55.

The next series of observations occurred 2007 January 27.8833 UT when Boyd (England) measured the average magnitude V = 14.83. On 2007 January 28.8507 UT Oksanen (Finland) measured an average V = 14.84. Average magnitude values are referenced simply because of the large oscillations, of as much as ~0.9 magnitude occurring within the light curve as shown in Figure 2 from a 3.6-hour time series on January 29, 2007, by Crawford. The series of measurements by Boyd on January 27 showed the oscillations ranging from V = 14.56 to V = 15.37 magnitudes, which appears close to DW Cnc's recent quiescent state and with oscillations similar to those prior to the outburst.

Figure 1 shows the overall light curve from all AAVSO V filter observations of DW Cnc between the JD dates of 2454094.5756 and 2454135.3084 (December 24, 2006– February 4, 2007) which show the outburst duration to have been less than ~7 days.

3. Period analysis

An analysis of Crawford's ~3.6-hour January 29, 2007, photometric data run (Figure 2) shows a strong period signal of 0.0268 day = 38.6 minutes (Figure 3), which is the asynchronous rotation period of the magnetic white dwarf star of this system as derived from photometry. This analysis was preformed by PERANSO software (Vanmunster 2005) using the CLEANEST method.

Figure 4 (a, b) show ~25 hours of photometric time series data with ~21.5 hours of data, from five nights, being contributed by Boyd and combined with Crawford's ~3.6 hours from one night's data. A CLEANEST period analysis of the data in Figure 4, also shows the same strong period signal of 0.0268 day; however, in this analysis a relatively strong secondary signal can be readily observed as well as some obvious weaker signals (Figure 5).

When the resulting period data from the combined Boyd and Crawford observations (Figure 4 and Figure 5) were pre-whitened to remove the 0.0268-day period signal, a strong secondary period signal of 0.0512 day was detected as shown in Figure 6. This strong secondary period is 73.73 minutes.

4. Discussion

It is unfortunate that during the ~4 preceding days of the observed outburst there are no observations known to the authors or the length of the outburst could be more accurately determined.

Uemura *et al.* (2002) also showed a strong secondary quasi-periodic oscillation at 73.4 ± 0.4 minutes. This is in close agreement with our own strong secondary signal of 73.73 minutes. We note that the Patterson *et al.* (2004) study showed a spin-orbital beat period of 69.91 minutes.

Hellier *et al.* (1997), in a study of the IP XY Arieti, presented additional outburst data for six intermediate polars (V123 Sgr, TV Col, EX Hya, XX Ari, YY Dra, and GK Per), and Hellier *et al.* (2000) presented a study of the

outbursts of the IP EX Hydrae and a discussion of mass-transfer events and disk instabilities. DW Cnc comes closest to EX Hya in terms of P_{orb} (98.4min) and TV Col in terms of P_{spin} (31.8 min), thereby sharing characteristics with both systems having outbursts due to disk instabilities and those having outbursts due to a mass transfer event. In addition, while DW Cnc ($P_{spin} = \sim55\%$ P_{orb}) may be grouped with the majority of IP's (TV Col-V1223 Sgr grouping) with respect to having a spin period greater than five percent of the orbital period, DW Cnc appears to have a higher-amplitude outburst (~4 magnitudes) than the other members, and a longer period of duration (~2–4 days) than either TV Col or V1223 Sgr (~1–2 days).

5. Conclusions

We report the first observation of an outburst of the intermediate polar system DW Cnc. The outburst at its observed maximum $V <= 11.36$ magnitude (qualified as star was saturated) showed a brightening of ~4 magnitudes from its previous quiescent state. The outburst was of a relatively short duration showing a fading of ~2.25 magnitudes in ~27 hours and another 1.25 magnitudes within another ~30 hours, from the time of discovery.

The rotational period of the white dwarf portion of the DW Cnc system (P_{spin}), as detected by Crawford's and Boyd's time series photometry at ~38.6 minutes, has remained the same since 2004. While Uemura *et al.* (2002) after a long term light curve study showed the strongest signal at a period ~37.5 minutes, Rodríguez-Gil *et al.* (2004) and Paterson *et al.* (2004) show the period to be ~38.6 minutes. Crawford and Boyd's data also show the rotational period to be stable over both short (3.6 hours) and longer (25.1 hours) periods of photometric time series data analysis.

No conclusion could be reached as to whether or not we are seeing a different spin-orbital beat period, a strong alias, or something else with the strong secondary period signal of 73.73 minutes.

DW Cnc does not appear to fit with either the grouping of IPs that go into outburst due to disk instabilities or those that go into outburst as a result of a mass transfer event, and no conclusion could be reached regarding the origin of this first observed outburst.

It would be desirable that both professional and amateur astronomers continue to observe and study this system, so that future outbursts can be detected and analyzed, and the question of whether or not the outburst is the result of disk instabilities, a mass transfer event, or even some other mechanism or combination can be resolved.

This is a demonstration, also, of the important role amateur astronomers from around the world can play in the collection of photometric data of variable stars, as well as the importance of the AAVSO as being a repository for those observations.

6. Acknowledgements

References

Hellier, C., Kemp, J., Naylor, T., Bateson, F. M., Jones, A., Overbeek, D., Stubbings, R., and Mukai, K. 2000, *Mon. Not. Roy. Astron. Soc.*, **313**, 703.

Hellier, C., Mukai, K., and Beardmore, A. P. 1997, *Mon. Not. Roy. Astron. Soc.*, **292**, 397.

Kholopov, P. N., Samus, N. N, Kukarkina, N. P., Medvedeva, G. I., and Perova, N. B. 1981, *Inf. Bul. Var Stars*, No. 2042.

Patterson, J., *et al.* 2004, *Publ. Astron. Soc. Pacific*, **116**, 516.

Rodríguez-Gil, P., Gänsicke, B. T., Araujo-Betancor, S., and Casares, J. 2004, *Mon. Not. Roy. Astron. Soc.*, **349**, 367.

Stepanian, J. A. 1982, *Perem. Zvezdy*, **21**, 691.

Sterken, C., and Jaschek, C. 1996, *Light Curves of Variable Stars—A Pictorial Atlas*, Cambridge Univ. Press, Cambridge.

Uemura, M., Kato, T., Ishioka, R., Novak, R., and Pietz, J. 2002, *Publ. Astron. Soc. Japan*, **54**, 299.

Vanmunster, T. 2005, PERANSO period analysis software, http://www.peranso.com

Table 1. Equipment used by the Authors

Observer (AAVSO Initials)	Telescope	Size	CCD
Crawford (CTX)	Meade, SCT @ f/10	30.5cm	SBIG ST-9XE
Boyd (BDG)	Meade SCT @ f/5.2	35cm	StarlightXpress SXV-H9
Gualdoni (GCO)	Meade SCT	25.4cm	SBIG ST-7XME
Gomez (GOT)	Newtonian @ f/5	20cm	SBIG ST7-XME
MacDonald (MDW)	Meade SCT @ f/6.3	25.4cm	StarlightXpress SXV-H9
Oksanen (OAR)	RCOS Ritchey-Chretien	40cm	SBIG STL-1001E
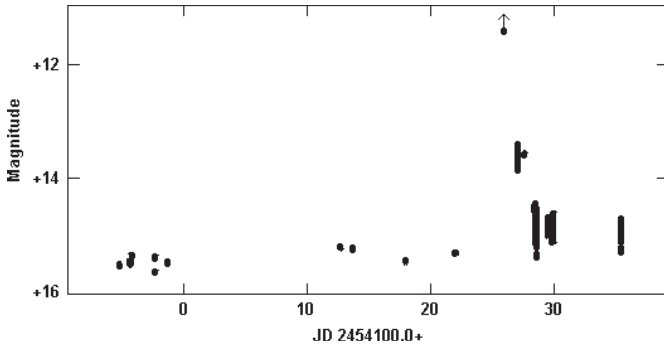
Figure 1. Photometric light curve from all AAVSO *V* filter observations of DW Cnc between the JD dates of 2454094.5756 and 2454135.3084 (2006 December 24–2007 February 04).
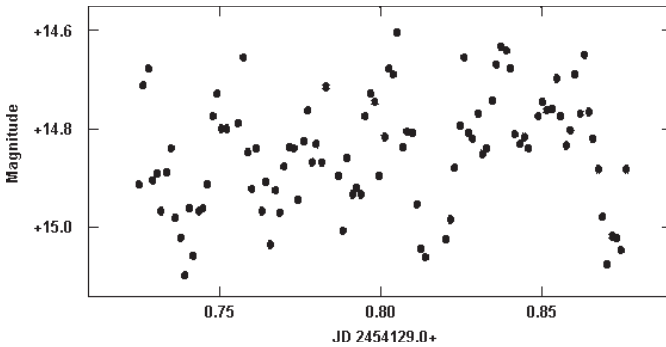
Figure 2. Time series photometry of DW Cnc obtained 2007 January 29, from *V* filter data gathered by Crawford over an approximate time period of 3.6 hours, demonstrating the frequent flickering of up to ~0.9 magnitude reported by previous observers.
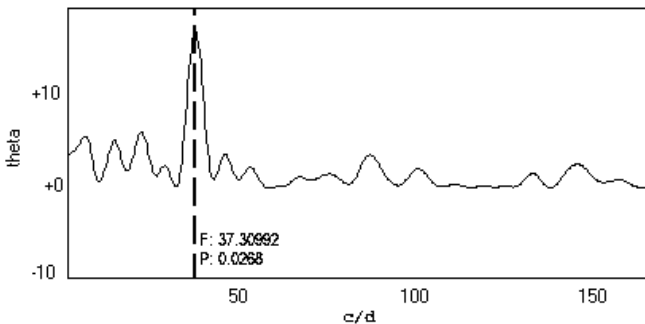
Figure 3. PERANSO software period analysis, using the CLEANEST method applied to Crawford's January 29, 2007, photometric data run as shown in Figure 2.
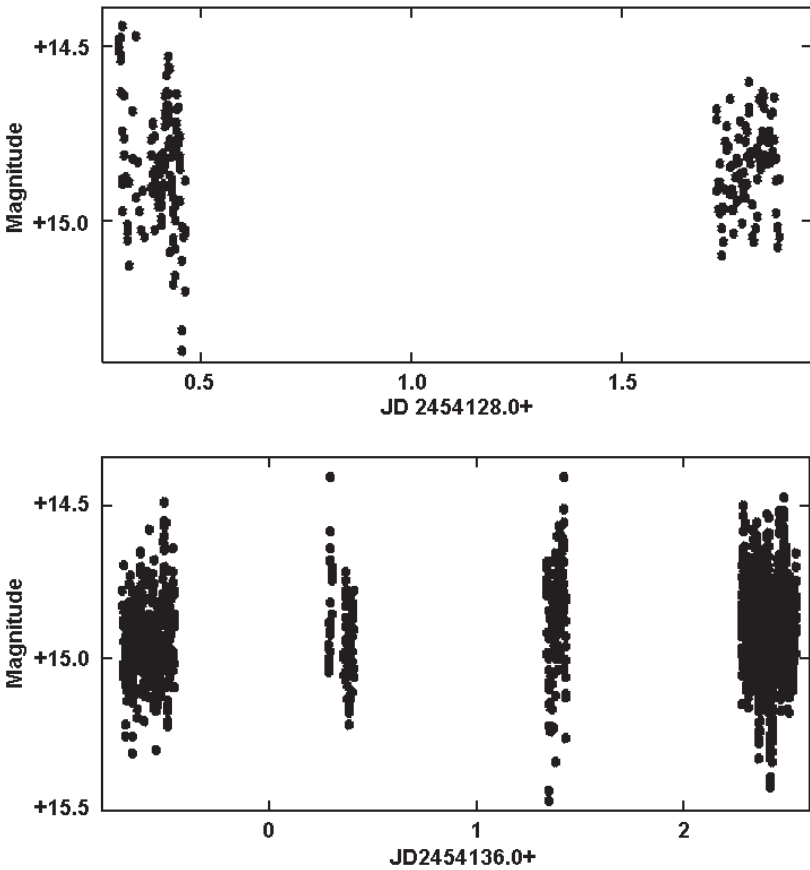
Figures 4a, 4b. ~25 hours of photometric time series data with ~21.5 hours of data from five nights, contributed by Boyd and combined with Crawdord's ~3.6 hours from one night's data. A CLEANEST period analysis of the data in Figures 4a and 4b, combined, also shows the same strong period signal of 0.0268 day.
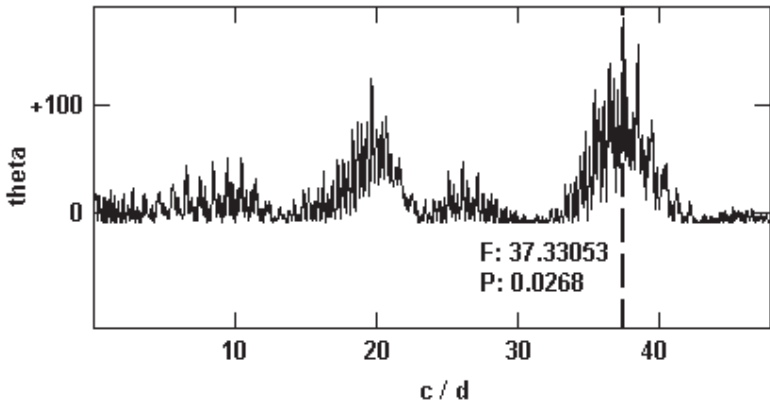
Figure 5. PERANSO software period analysis, using the CLEANEST method applied to ~25 hours of time series photometry. A relatively strong secondary signal can be readily observed as well as some obviously weaker signals.
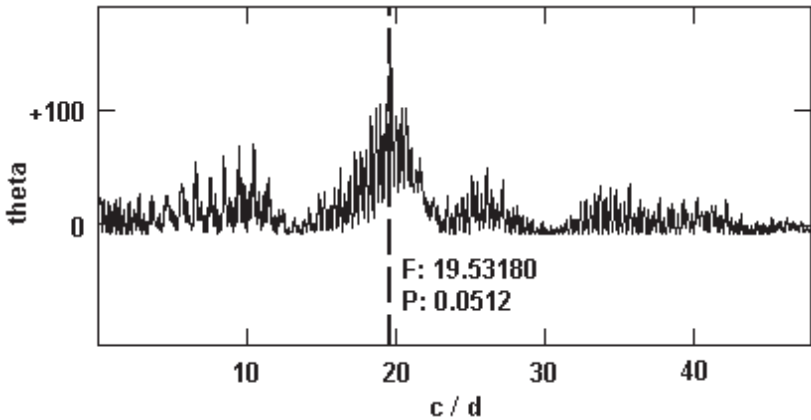
Figure 6. This presents the data from Figure 5 after a CLEANEST period analysis, after being prewhitened to remove the primary detected period signal of 38.6 minutes and leaving a strong secondary signal of .0512 d = 73.73 minutes.

Analysis of *BVI* Photometry of the Eclipsing Binary EV Lyrae

Jerry D. Horne

3055 Lynview Drive, San Jose, CA 95148

Abstract   Differential photometry of the previously little-observed semi-detached eclipsing binary EV Lyr from the 2006 observing season is presented and analyzed. This study utilized a 25-cm SCT instrument to observe portions of 116 orbital cycles and obtain *B*-, *V*-, and *I*-band photometry. This allowed the development of a complete phase diagram of the system and determination of the period of 0.91847 ±0.0002 day and HJD epoch 2453894.71997. Visual band photometric observations were fit to a binary star model phase diagram using the binary star modeling program NIGHTFALL. Derived properties for the primary were $M/M_\odot = 1.6$, $R/R_\odot = 1.64$, spectral type F0 V, and effective temperature of 7300 K. Derived properties for the secondary were $M/M_\odot = 0.79$, $R/R_\odot = 0.78$, spectral type K0 V, and effective temperature of 5200 K. Inclination for the system was found to be 88°.

1. Introduction

As part of an informal, on-going project to clean up, correct, or complete entries in the *General Catalogue of Variable Stars* (GCVS) (Krajci 2006), an observational study of EV Lyr was begun in the 2006 observing season (northern hemisphere). EV Lyr is listed in the current on-line GCVS (Samus *et al*. 2007) as a semi-detached eclipsing binary star, although the period and associated epoch are not currently shown. Its variability was first described by Hoffmeister (1929) as an Algol-type star system that varies between 13.0 and 15.0 apparent magnitude, with this variability probably derived from visual observations. Since then, little has been published on this variable star system, except for a period determination from an automated survey by Hartman *et al.* (2004). As a type EA/SD binary, the surface of the less massive component of EV Lyr is close to its inner Roche lobe, and is likely ellipsoidal in shape. Typically for these types of binaries, the light remains constant between eclipses or varies very slightly because of reflection effects, surface features, and/or the shape of a component star. The GCVS gives periods of known semi-detached binaries which typically range from 0.4 day to 18 days or more, with an average of 2.4 days (Samus *et al*. 2007).

Because photometry of this type of system lends itself to modeling by binary star modeling software, detailed multi-band photometry of the system

can be used, in conjunction with the software, to derive the major parameters of the stellar system. In this manner, observable and deduced properties of incomplete entries in the GCVS can be obtained.

2. Observations

In the summer of 2006, EV Lyr was observed from JD 2453894.755 to JD 2454001.781 (6 June 2006 through 23 September 2006), encompassing 116 orbital cycles. The observations were made using a Meade LX200 10-inch (0.25-m) telescope, with a Starlight Xpress MX 716 CCD camera, which has a 550×720 pixel array. One-minute exposures were taken at an *f*-ratio of 6.3 (for an effective field of view of approximately 11×14 arcminutes) with Johnson *B*, *V*, and Cousins *I* filters. Typical seeing conditions for this low-altitude site were between 3.5 and 4.5 arc seconds FWHM for EV Lyr in each image. The airmass for observations ranged from 1.01 through 1.45. All exposures were dark current and bias subtracted, and also flat-fielded (using twilight sky flats) according to established procedures. The software tool AIP4WIN, Ver 2.0 (V2.1.0, Berry and Burnell 2000), was utilized for photometric measurements.

All exposures of EV Lyr included two comparison stars GSC 31345 (Tycho data: $V = 10.02$, $B = 11.03$) and GSC 31343 (Tycho data: $V = 10.09$, $B = 10.37$). To insure that the comparison stars were not variable, the difference between GSC 31345 and GSC 31343 was also measured for each exposure. The standard deviation of the *V*- and *B*-band magnitude difference over all observations was found to be 0.020 and 0.017, respectively.

The *B*, *V*, and *I* photometric data on each comparison star were normalized with measurements taken from Tycho observations of these comparison stars, corrected to the Johnson and Cousins system. Zero points were then determined from the comparison star photometry and applied to the EV Lyr photometry using AIP4WIN to produce standardized *B–V* and *V–I* measurements of EV Lyr. The calculated photometric error of observations of EV Lyr was at or below 0.04 magnitude.

The position determined for EV Lyr was R.A. $19^h 26^m 36.45^s$ Dec. $+39°$ 02' 17.6" (2000.0) based upon the reference coordinates in the *USNO-A V2.0 Catalog* (Monet *et al.* 1998), and is within 3.5 arcseconds of the position generated from the SIMBAD website (FK5 2000.0 coordinates: R.A. $19^h 26^m 36^s$ Dec. $+39° 02' 06"$) and the coordinates in the GCVS.

Since there was limited knowledge of the parameters of the EV Lyr system, a sustained observation program had to be mounted to observe the variable on a regular basis for a significant number of hours per observing session. The binary system was initially observed nightly for a period of three weeks starting in June of 2006. Fortunately, during this initial observing campaign, multiple primary eclipses and several secondary eclipses were recorded.

3. EV Lyr period determination and phase diagram

To determine the period of EV Lyr, nine sets of *V*-band data taken during the initial observational campaign, each four to five hours in length, and including a primary eclipse in six such sets, were entered into the software program PERANSO (Vanmunster 2005). Using PERANSO's EA SOLVER analysis tool, the period for EV Lyr was determined to be approximately 0.9183 day, which allowed a complete phase diagram to be generated from the observational data. This phase diagram is seen in Figure 1. The phase diagram has the obvious characteristics of a semi-detached eclipsing binary, with a deep primary eclipse and a shallow secondary eclipse. Presumably, it is aspects of this phase diagram that allowed Hoffmeister to deduce this binary as an Algol type, but no such phase diagram was included in the original publication (Hoffmeister 1929), nor could be found in the literature. Multiple eclipses were recorded over the remainder of the summer and the midpoint of each eclipse identified. Utilizing the minima tool of Kwee and van Woerden (1956) in PERANSO, a more precise orbital period was calculated for EV Lyr as 0.91847 ± 0.00002 day, with a corresponding HJD epoch of 2453894.71997. The previously noted automated survey period determination (Hartman *et al.* 2004) was 0.9185 day.

4. Primary and secondary eclipses

The primary eclipse for EV Lyr was measured to be from 13.83 to 15.93 *V* magnitude, with the secondary eclipse measured from 13.83 to 14.04 *V* magnitude. The duration of the primary and secondary eclipses were measured to be 4.4 and 2.85 hours, respectively. A phase diagram of the primary eclipse in *B*, *V*, and *I* bands are shown in Figure 2. The average *B–V* color index of the non-eclipse light was found to be 0.68, while the *B–V* color index at maximum eclipse was measured to be 0.80. For the secondary eclipse, the *B–V* color index at maximum eclipse was measured to be 0.63.

5. Intrinsic variation

In order to detect any variability of EV Lyr during non-eclipse segments of its orbit, sets of twenty *V*-band exposures were averaged during seven six-hour observing runs. This averaging decreases the overall effects of scatter and scintillation. A plot of the light from EV Lyr for these non-eclipse averaged observations is shown in Figure 3. As can be seen, light from the binary star system varies up to approximately 0.1 *V* magnitude over a six hour period, and is present in both the early and later observational data sets. This variation could be the result of the ellipsoidal shape of the secondary star, surface spots/surface activity, heating effects on the primary or secondary star, and/or the result of low-volume mass transfer, although no flares or rapid brightening events were observed.

6. Spectral type and effective temperature

Although the graph of the primary eclipse does not have a flattened bottom, indicating that the eclipse is not total, the depth of the eclipse would still indicate that little of the primary star's light is present at eclipse maximum. Using the *B–V* color index of primary eclipse at this point allows computation of the probable effective temperature of the secondary star (Popper 1980).

McWilliam (1990) and Amado and Byrne (1996) have provided empirical relationships for effective temperature versus color indices (e.g., *B–V* or *V–I*) for stars of spectral types G to M. Using the color index of 0.80, this empirical relationship indicates an effective temperature of 5200 K. Using published tables of luminosity class and star effective temperatures from Meyer *et al.* (1998), this effective temperature would mean that the secondary star is likely a K0 V.

7. Fit to a binary star model

The binary star modeling software tool NIGHTFALL (Wichmann 1999) was used to model the EV Lyr system. This program utilizes the Djurašević (1992) binary star model. A phase-based data file for the entire phase diagram was created from the observations that included both the intrinsic variation and eclipse data points and this file was input to the modeling program.

Before beginning the phase diagram matching routine, certain parameters need to be input from known values from the observations or assumed from astrophysically reasonable numbers (Wilson 1994). The orbital period has been determined, as well as the probable effective temperature of the secondary star. Although the effective temperature of the primary star can not be similarly directly measured, it is possible to infer a range of spectral types from the overall EA/SD binary type and eclipse data. As the primary eclipse is quite deep—slightly more than two magnitudes—this should mean that the primary is several thousand degrees hotter than the secondary, and is probably a late A- or early F-type star, with an approximate effective temperature of 7500 K. This stellar type was used for the initial temperature and corresponding mass of the primary star parameters.

In turn, using common masses for these type stars the initial mass ratio would be 0.5 for the EV Lyr system. The (Roche Limit) fill factor was set to 0.6 and 1.0 for the primary and secondary, respectively. The initial inclination was assumed to be 89°. The linear cosine relationship was utilized in the model for limb-darkening.

The data-fitting routine of the software was started, and most system parameters (inclination, primary mass, primary fill factor, etc.) were allowed to vary from their initial conditions. After multiple iterations, the best match for the data (i.e., the smallest χ-square value = 0.95) was found. The NIGHTFALL software model output for *V*-band photometry is shown in Figure 4. This same

output, mapped together with the observational data, is shown in Figure 5. It should be noted that the output of the NIGHTFALL program positions the primary eclipse at the 0.5 phase point and the phase diagram is drawn from –0.25 to 0.75 phase. Figure 6 shows the residual values of the EV Lyr observation data subtracted from the binary star model data for the same orbital phase points. Using this best-fit solution to the observational data, the probable physical parameters for the EV Lyr star system are shown in Table 1.

8. Conclusions

This paper has presented new *B*-, *V*-, and *I*-band photometry of EV Lyr, which included multiple observations of the primary and secondary eclipses, and uncovered some intrinsic variability of the system. From these observations, it has been possible to determine the orbital period of EV Lyr and the associated epoch, and deduce the other principle parameters of the binary star system, which can be added to the data of the GCVS for this system. The analysis, together with the EV Lyr phase diagram, confirms that this stellar system is a typical semi-detached eclipsing binary. The period of EV Lyr, at 0.91847 day, is shorter than approximately 80% of similar EA/SD binaries listed in the current online GCVS (Samus *et al.* 2007), although the derived stellar types, radii, and masses are very similar to other Algol-type systems (Popper 1980).

9. Acknowledgements

References

Amado, P. J., and Byrne, P. B. 1996, *Irish Astron. J.*, **23**, 177.

Berry R., and Burnell, J. 2000, "Astronomical Image Processing Software," version 2.1.0, provided with *The Handbook of Astronomical Image Processing*, Willmann-Bell, Richmond, VA.

Djurašević, G. 1992, *Astron. Space Sci.*, **196**, 241.

Hartman, J. D., Bakos, G., Stanek, K. Z., and Noyes, R. W. 2004, *Astron. J.*, **128**, 1761.

Hoffmeister, C. 1929, *Astron. Nach.*, **236**, 233.

Krajci, T. 2006, *The Society for Astronomical Sciences 25th Annual Symposium on Telescope Science*. Society for Astronomical Sciences, Rancho Cucamonga, CA, 71.

Kwee, K. K., and van Woerden, H. 1956, *Bull. Astron. Inst. Netherlands*, **12**, 327.

McWilliam, A. 1990, *Astrophys. J., Suppl. Ser.*, **74**, 1075.

Meyer, M. R., Edwards, S., Hinkle, K. H., and Strom, S. E., 1998, *Astrophys. J.*, **508**, 397.

Monet, D., *et al.* 1998, *USNO-A V2.0 Catalog of Astrometric Standards*, U.S. Naval Observatory, Flagstaff, AZ.

Popper, D. M. 1980, in *Annual Review of Astronomy and Astrophysics*, **18**, Annual Reviews, Inc., Palo Alto, CA, 115.

Samus, N. N., *et al.* 2007, *General Catalogue of Variable Stars* (http://www. sai.msu.su/groups/cluster/gcvs/gcvs), Sternberg Astron. Inst., Moscow.

Vanmunster, T. 2005, PERANSO period analysis software, www.peranso.com

Wichmann, R. 1999, NIGHTFALL, binary star software, www.lsw.uni-heidelberg. de/users/rwichman/Nightfall.html.

Wilson, R. E. 1994, *IAPPP Communications*, No. 55, 1.

Table 1. Observed and derived EV Lyr system properties. From observations by the author in 2006.

Parameter	Value
Primary Spectral Type	F0V
Primary Star Mass	$1.6\ M_\odot \pm 0.08\ M_\odot$
Primary Star Radius	$1.64\ R_\odot \pm 0.1\ R_\odot$
Secondary Spectral Type	K0V
Secondary Star Mass	$0.79\ M_\odot \pm 0.08\ M_\odot$
Secondary Star Radius	$0.78\ R_\odot \pm 0.08\ R_\odot$
Mass Ratio (q_0)	0.43 ± 0.1
Orbital Inclination (i)	$88° \pm 1.0°$
Stellar Separation	$5.31\ R_\odot \pm\ 0.07\ R_\odot$
Orbital Period	0.91847 ± 0.0002 day
HJD Epoch	2453894.7199 ± 0.0007
Duration of Primary Eclipse	5.9 ± 0.03 hours
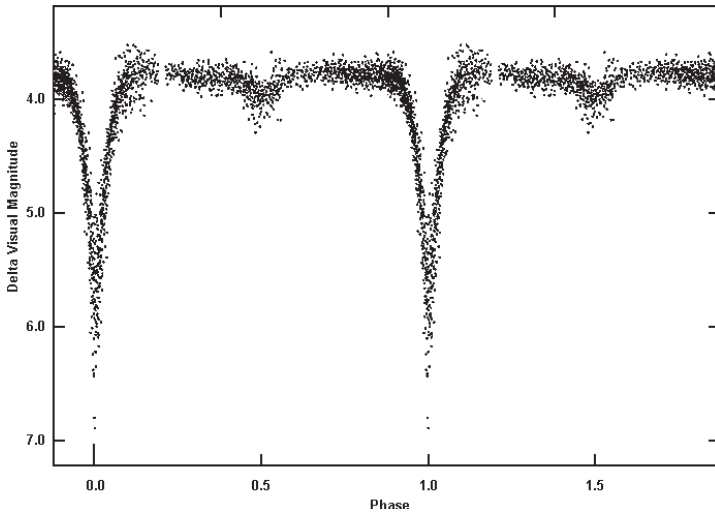
Figure 1. Phase diagram for EV Lyr. From observations by the author in 2006.
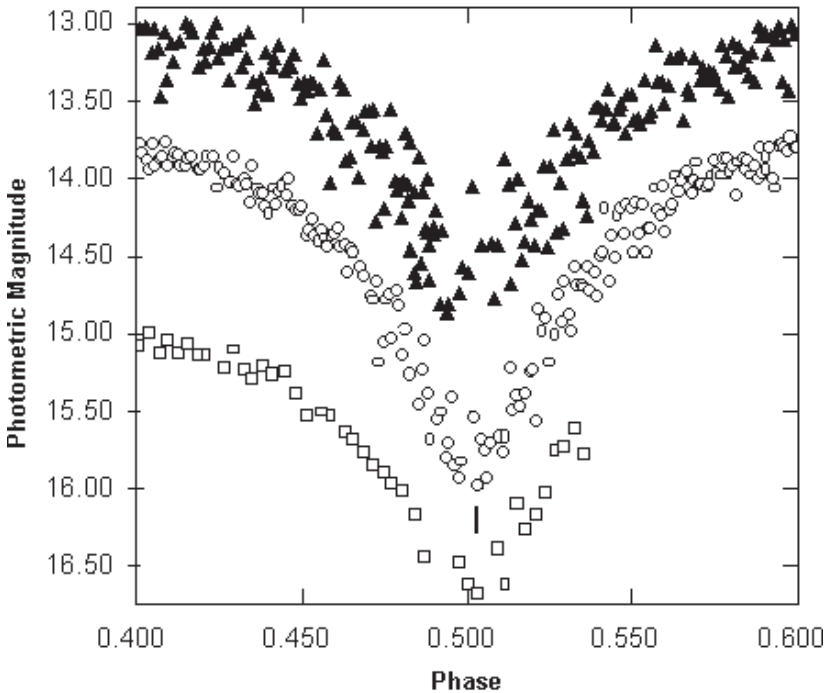
Figure 2. Phase diagrams of the primary eclipse of EV Lyr. From observations by the author in 2006. Circles denote *V* band; squares, *B* band; triangles, *I* band.
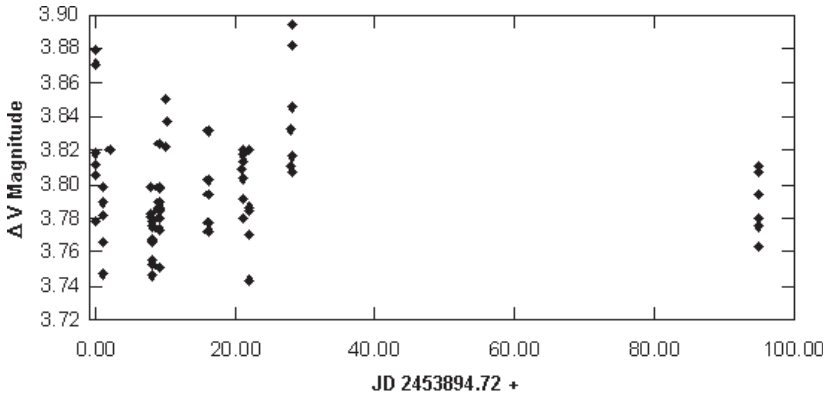
Figure 3. Intrinsic variability of EV Lyr. Each diamond is an average of 20 individual observations, with a *V* magnitude uncertainty of 0.02. From observations by the author in 2006.
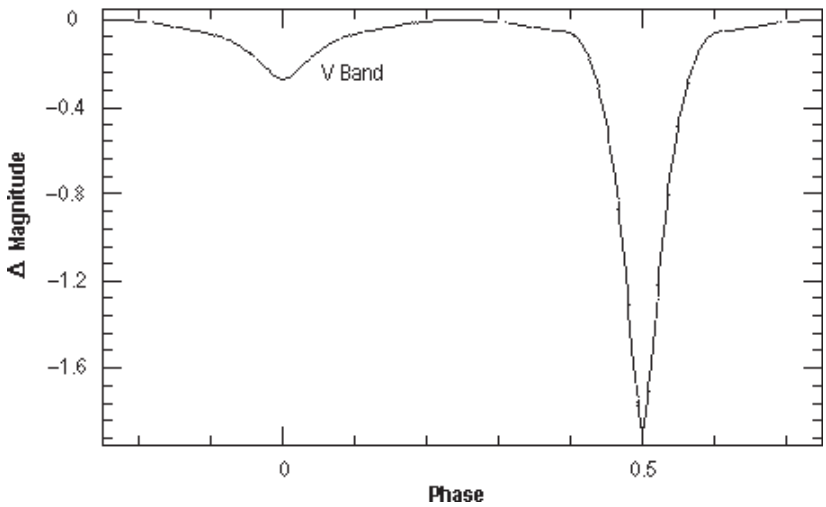
Figure 4. EV Lyr NIGHTFALL Binary Model phase diagram.
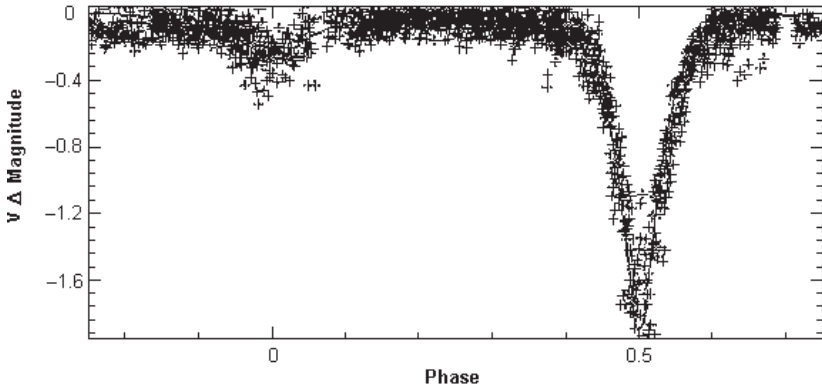
Figure 5. EV Lyr observational data fit (pluses) to binary model (line) shown in Figure 4. From observations by the author in 2006.
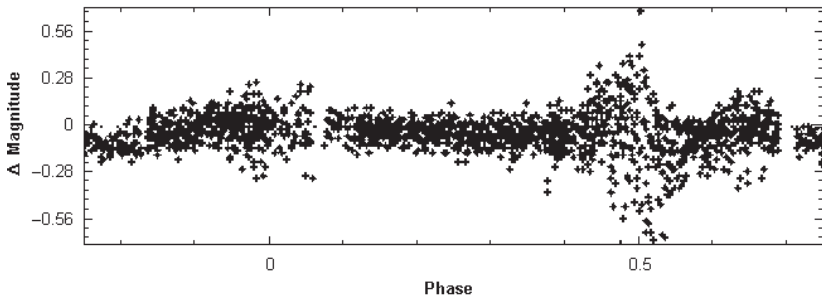
Figure 6. Residual values of EV Lyr observed minus fit data. From observations by the author in 2006.

Combining Visual and Photoelectric Observations of Semiregular Red Variables

Terry T. Moon
Astronomical Society of South Australia (ASSA), GPO Box 199, Adelaide, SA 5001, Australia

Sebastián A. Otero
Grupo Wezen 1 88, Buenos Aires, Argentina
and Centro de Estudios Astronómicos (CEA), Mar del Plata, Argentina

Laszlo L. Kiss
School of Physics, University of Sydney, NSW 2006, Australia

Abstract   Combining visual observations of semiregular variables with measurements of them using a photoelectric photometer is discussed, and then demonstrated using data obtained for the bright, southern semiregular variable θ Aps. Combining such observations is useful in that it can provide a more comprehensive set of data by extending the temporal coverage of the light curve. Typically there are systematic differences between the visual and photometric datasets that must be corrected for.

1. Introduction

The authors have been undertaking independent observing programs of variable stars (one in Argentina and the other in Australia) that include a group of bright semiregular red variables (SR) at southern declinations. One of us, Sebastian Otero, is undertaking a program of visual observations using a modified version of the Argelander method (Otero, Fraser, and Lloyd 2001) while another, Terry Moon, regularly obtains photoelectric photometry measurements of about thirty bright SR variables located at southern declinations. A number of these are being monitored by both programs, namely β Gru, θ Aps, X TrA, SX Pav, Y Pav, R Dor, BO Mus, and V744 Cen. The combining of visual estimates of magnitude with photoelectric photometry measurements is thus of interest as it affords us the opportunity to increase coverage of the light curves for these semiregular red variables. The importance of the extent of the set of observations was emphasized by Kiss *et al.* (1999). In an earlier paper, Otero and Moon (2006) combined their independent observations of β Gru to determine its characteristic period of pulsation. For that paper an overlap in the two sets of data was used to evaluate any mean difference between them. Subsequently a small correction of –0.03 magnitude was applied to the visual estimates to bring

them into accord with the photoelectric measurements. This paper discusses some of the issues associated with combining visual and photoelectric data, the discrepancies that arise, and why, then illustrates a practical approach to combining such data using observations of θ Aps as an example. Our dataset will be web-archived and available through the AAVSO ftp site at: ftp://ftp. aavso.org/public/datasets/jmoont361a.txt, jmoont361b.txt.

2. Visual estimates versus photoelectric measurements

Undertaking visual observations of variable stars remains popular owing to a number of advantages but there are also some significant drawbacks (Simonsen 2004). Henden and Kaitchuck (1990) note that "the human eye can generally interpolate the brightness of one star relative to nearby comparisons to about 0.2 magnitude." More recently Toone (2005) has pointed out that there can also be discrepancies of 0.2 magnitude or more between comparison star sequences from different sources. Using a modified version of the Argelander method in which the observer makes allowances for color differences by observing comparison stars encompassing a wide range of spectral types, and uses photoelectric rather than visual sequences of comparison stars, such discrepancies may be reduced to 0.1 magnitude.

Photoelectric photometry (Henden and Kaitchuck 1990) provides precise measurements of variable stars that can be recorded and then reduced to accurate magnitudes. Using different filters, color indices can also be measured, yielding additional information of astrophysical significance. Typically, the precision of photoelectric photometry measurements is better than 0.01 magnitude, but the scatter in *V* and *B–V* determined from many observers transforming their measurements to the standard UBV system appears to be about 0.02 magnitude (Böhm-Vitense 1981). Table 1 summarizes the comparative advantages and disadvantages of visual and photoelectric photometry observations.

3. Comparison of spectral responses

The spectral response of the Optec *V*-band is sufficiently close to that defined by the standardized UBV photometric system so that a linear relation can be applied to transform the measurements made to *V* magnitudes (Figure 1). Measurements of stars (encompassing a wide range of spectral types) made with this photometer confirm that a linear relation with respect to *B–V* suffices for transforming the photoelectric photometry *V*-band measurements to standardized *V* magnitudes and, similarly, a linear relationship also suffices for transforming measured to standard *B–V* indices. Figure 1 illustrates that the spectral response of the dark-adapted human eye (scotopic vision), in contrast, varies significantly from that for the standard *V*-band.

The problem is particularly complicated for SR variables owing to the prominent molecular absorption bands present in their spectra. Inspection of

Figure 1 shows that some of these will be included within the spectral response for the human eye and excluded from that for the photoelectric photometer and vice versa. A small shift in wavelength of the spectral response of a detector could then make a noticeable difference in the measured magnitude.

To explore the effects of detector spectral responses and stellar spectral features on magnitudes estimated or measured, spectral responses for dark-adapted (scotopic) vision, the *V*-band of the standard UBV system and that for the Optec *V*-band were multiplied by the spectrum of the SR variable θ Aps (Kiehling 1987). The integrated magnitudes were then calculated. The scotopic spectral response was chosen as it represents human vision using the rod receptors in the retina of the eye—a common approach to the estimation of variable stars is to use averted vision to exploit the low-light-level sensitivity of the rods (represented by the scotopic spectral response). While this is a useful technique for estimating magnitudes for variables that change in brightness by many magnitudes and those that may be at the limit of visual detection when at their minimum brightness, for bright stars the spectral response of the human eye may be better approximated by mesopic vision—a combination of scotopic and photopic vision.

The calculated *V* magnitude using the response of the Optec photometer differed from that for the standard system by 0.02 magnitude, while the magnitude calculated for scotopic vision differed by as much as 0.5 magnitude! Using cone receptors in the retina to a greater or lesser degree, this difference may be reduced, as the resultant visual spectral response will be shifted to longer wavelengths and thus closer to that of the standard photoelectric *V*-band. Although the techniques used by the visual observer will determine the effective spectral response for the visual observations, the calculations undertaken here illustrate the significant effect that differences in the spectral response can have on the *V* magnitudes determined for red variables.

While experienced visual observers account for the "Purkinje effect" (arising from the shift in the spectral response of human vision to the blue end of the spectrum at low illumination levels), small residual differences between the magnitudes of SR variables estimated visually and those measured using a photoelectric photometer are to be expected. Such discrepancies between visual and photoelectric photometry observations may also be color-dependent.

4. Transformation of photoelectric photometry measurements

The UBV standardized photometric system was introduced by Harold Johnson and William Morgan in the 1950s. Standard spectral responses for this photometric system were defined along with a set of standard stars. All measurements made with other instantiations of the UBV system thus require measurement of standard stars to determine the transformation relations. Linear transformations suffice, provided detectors and filters are chosen carefully so that their combined responses closely match the standard system.

While straightforward in principle, several practical problems arise:

• The standard stars do not encompass all spectral types, excluding by necessity any variable stars

• The primary standard stars defined by Johnson and Morgan are for Northern Hemisphere observers

• The original photomultiplier tube and filters used by Johnson and Morgan have been replaced by different brands, hence, later systems approximate rather than replicate the spectral responses of the original system

These practical problems pose significant challenges for photoelectric photometry measurements of bright SR variables at southern declinations. Firstly, virtually all M-type giants vary to some extent with amplitudes tending to increase for later types (Percy and Harrett 2004). Secondly, measurements of SR variables usually require extrapolation of the linear transformations determined using earlier-type stars that have smaller values of $B–V$. And thirdly, finding sufficiently "red" comparison stars that are both bright and close by to an SR of interest can be difficult.

To minimize these problems the comparison stars chosen are K-type giants, preferably those of later type with $B–V \sim 1.4$. Fortunately these are also common enough among bright stars so that there is usually one sufficiently close to the SR variable being measured. Many bright stars have been extensively measured over the years and their magnitudes and colors well determined. "The General Catalogue of Photometric Data" (GCPD; Mermilliod *et al.* 1997) is a heterogeneous source of photometric data for bright stars where multiple measurements of a star have been combined. The catalogue thus provides a useful source of well-determined magnitudes and colors for calculating transformation relations.

The question arises as to how well the V and $B–V$ data in this catalogue, a compendium of measurements by different observers using different equipment, represent a consistent and standard system and, particularly, how well the system can be applied to the measurement of SR variables. To check this, measured $B–V$ indices of thirty SR variables were compared to their GCPD values. The measurements represent a homogeneous set of data where linear relations for transformation of V and $B–V$ have been well-established for stars ranging in $B–V$ from 0 to 1.5. As is the case for all observers, this relation was then extrapolated for redder stars.

Figure 2 shows the plot of the measured $B–V$ indices as a function of the GCPD values for thirty southern, bright SR variables. Also plotted is the line for a one-to-one correspondence between the $B–V$ measurements and listed GCPD values. Some of the SR variables, particularly the redder ones, vary substantially in $B–V$, hence error bars have been drawn showing the range of their measured $B–V$ variations. GCPD values may, however, represent measurements at one part of the cycle of variation in $B–V$. Within the error

bars shown the agreement is good, providing confidence in the:

>   • fidelity with which a readily-available commercial photometer can measure *V* and *B–V* for SR variables, and

>   • consistency of *V* and *B–V* data listed in the GCPD for SR variables. This would also suggest that, where the photometer's spectral response is sufficiently well-matched to the standard system, the linear transformations determined using earlier-type stars may be extrapolated to redder stars such as SR variables, the resultant accuracy being determined by the differences arising from inclusion or exclusion of spectral features in the pass-band of the photometer. For an SR variable with a *B–V* ~1.7 (such as θ Aps), this could amount to several hundredths of a magnitude.

5. Visual and photoelectric photometry observations of θ Aps

Visual observations of θ Aps were made in Argentina from JD 2451621 to JD 2454180 using the Argelander method. Independently, photoelectric photometry was undertaken in Australia from JD 2452676 to JD 2454157. Subsequently, correspondence between the authors led to the pooling of their observations for further analysis.

The visual observations were made with the naked eye using a modified version of the Argelander method in which the visual magnitude for a bright variable star was estimated relative to several comparison stars but using direct (cone) vision rather than averted (rod) vision, as the spectral response for cone vision better approximates the response of the *V*-band. As all M-type stars are believed to be variable to some extent, choosing comparison stars of similar color (*B–V* index) to SR variables is problematic. The approach taken was to try to choose comparison stars with *B–V* indices as similar (i.e., red) as possible, i.e. late-K giants. As it is not always possible to find comparison stars of similar brightness and color and sufficiently close to the SR variable being observed, the visual observing technique developed also attempts to correct for color differences by using a different observing approach depending on the star's color and brightness and the sky background. Typically, bright red stars will saturate the cones, causing overestimation of the star's magnitude; conversely, faint red stars will not activate the cones, so their brightness may be underestimated. To reduce these effects, quick glances with slightly averted vision is used in the former case and direct vision in the latter. A bright background can cause underestimation of the brightness of blue stars and overestimation of the brightness of red ones, so a mix of cone and rod vision is used to minimize such effects. Using these techniques, along with photoelectric values for the magnitudes of the comparison stars rather than the values given in visual charts, estimates of the *V* magnitude of a variable are made rather than the traditional m_{vis} values based on rod (scotopic) vision. A full description of the observing technique used can be found in the video and presentation

slides of a talk given at the 94th annual meeting of the AAVSO two years ago (URL: http://www.aavso.org/aavso/meetings/fall05video/adv_otero.mov). This observing method can achieve a precision of 0.05 magnitude (Otero, Fraser, and Lloyd 2001). As indicated in Section 3, molecular absorption bands in the spectra of red giants will, however, affect the visual estimates.

The photoelectric measurements were made with an Optec SSP-5A photometer attached to a permanently-mounted 10-cm telescope housed in an observatory with a roll-off roof. For each star, five consecutive measurements, each of ten seconds integration time, were taken through the V filter. On some nights B-band measurements were also taken. As the observatory is situated in an outer suburb of a major city (Adelaide), the background sky was measured for each star. When measuring through both B and V filters the sequence was V_{star}, B_{star}, B_{sky}, V_{sky} with the time recorded at the switching of the filters during the sequence of measurements of the star through the two filters.

Measurements of θ Aps were always bracketed by measurements of two comparison stars and were usually part of more extensive observing sessions during which a group of bright, southern SR variables and their nearby comparison stars were measured. This allowed atmospheric extinction to be evaluated on each night from the group of comparison stars measured. Calibrations for transformation to standard V magnitude and $B–V$ color index have been established and are checked periodically. All comparison star values in this paper are taken from the GCPD (Mermilliod *et al.* 1997), rounded to the nearest 0.01 magnitude.

Corrections were applied to all photoelectric measurements for differences in air mass. The corrected magnitudes were then transformed to standard V magnitudes and $B–V$ color indices. This transformation involves a correction, as a function of $B–V$, to the measurements through the V filter. The standard deviation for all the $B–V$ measurements of θ Aps was 0.04 magnitude, however there was a large discrepancy between measured values and those listed in catalogues. The GCPD lists a $B–V$ of 1.48 for θ Aps, bluer than would be expected for an M6.5III star. Consequently, the average measured value of 1.68 was used for transforming V filter measurements to standard V magnitudes. Considering the correction coefficient was 0.07, any nightly variations resulting from using the average rather than measured value ($B–V$ was not measured on all nights) would typically be no more than 0.003 magnitude.

HR 5547 was used as the primary comparison star for most of the photoelectric photometry measurements, with a variety of other stars used to check its constancy. (For some of the earlier measurements α Aps was used as the primary comparison star but HR 5547 was subsequently chosen as it can be measured on the same photometer sensitivity setting.) The deviations of measurements of this comparison star from its GCPD value were also monitored. Over the course of the observations presented here, the average V magnitude of HR 5547 was in agreement with its GCPD value to within a few thousandths of a magnitude. Standard deviations of each measurement are also

calculated, the mean standard deviation of the photoelectric measurements for θ Aps being 0.01 magnitude. Figure 3 shows the observations made; a shift of –0.05 magnitude has been applied to the visual estimates to bring their mean value into accord with that for the photoelectric photometry measurements.

6. Results

6.1. Analysis by Terry Moon (using PERSEA software)

As both the visual and photometric sets of data cover many cycles with a substantial interval in common, it was possible to compare them for systematic differences during the period analysis process. Analysis undertaken using the software package PERSEA, which is based on the optimal period search method of A. Schwarzenberg-Czerny (Maciejewski 2005), gave a mean V from visual estimates (comprising 431 points) of 5.42, while the photoelectric photometry measurements (comprising 200 points) gave a mean $V = 5.37$. Considering the differences in the spectral responses of the eye and the photometer as discussed in Section 4, this difference is small and may be corrected for by adding –0.05 magnitude to the visual estimates of V.

The interval chosen for a period search was 7 to 1,000 days, with the visual and photoelectric data first analyzed separately to determine the mean magnitude for each (confirming the difference of 0.05 magnitude between the visual estimates and photoelectric photometry measurements) and to gauge the difference in the period determined using only the visual or photoelectric photometry observations. They were then analyzed as a single, combined dataset. A main peak found in the periodogram corresponded to a period of about 111 days. Table 2 summarizes the results from the analysis using PERSEA, giving the period of the dominant peak and an estimate of the precision in its determination, the mean V magnitude calculated, the range in the light curve, and the number of points used in the analysis.

6.2. Analysis by Laszlo Kiss (using PERIOD04 software)

The visual and photoelectric photometry data were also analyzed using PERIOD04 (Lenz and Breger 2007), which is a standard approach for period searches in pulsating stars and is the latest version of the original code written by Michael Breger back in the 1970s. This software allows pre-whitening in the time domain, so that, after finding the frequency of a best-fit sine-wave, that frequency is subtracted from the data and the residuals re-analyzed until there is a significant peak in their power spectrum. PERIOD04 also offers different weighting schemes. When applied, each point was weighted by the inverse square of its stated error. As for the analysis using PERSEA, periods in the order of the interval over which the observations spanned, i.e., ~2,600 days, were considered artifacts.

First, analysis was undertaken using both weighted and non-weighted photoelectric photometry data only. For both weighted and non-weighted data

the three periods found were very similar, the main effects of weighting being to increase the amplitudes and reduce the scatter in the resulting fits to the data (see Table 3).

For the visual data, the stated error was mostly 0.05 and occasionally 0.1 magnitude. The results of the analyses for both weighted and non-weighted visual data are given in Table 4. Finally, combining the photoelectric photometry and visual data gave results presented in Table 5.

6.3. Analysis by Sebastián Otero (using AVE software)

Visual and photoelectric photometry data were also analyzed with the AVE software using two algorithms—PDM and SCARGLE (Barberá 1996). Similar to the analysis using PERSEA, zero-point corrections were made to bring the mean *V* magnitude of the visual estimates into agreement with that for photoelectric photometry measurements. The two datasets were first analyzed separately then combined over their interval in common, i.e., from JD 2452676 to 2454156. A predominant period of 111.2 ± 0.1 day was found in the two separate and combined analyses and using both PDM and SCARGLE. Using all the available data collected since JD 2451621, both visual and photoelectric photometry, a predominant period of 110.6 day was determined from both the PDM and SCARGLE algorithms.

7. Discussion and conclusions

Figure 3 illustrates that visual and photoelectric photometry data of SR variables can be successfully combined for subsequent analysis provided suitable methods are followed with making both the visual and photoelectric photometry observations. Corrections of ~0.05 magnitude may, however, need to be applied owing to the significant differences in the spectral responses of the human eye and photoelectric *V*-band. (See also Otero and Moon 2006, where a similar correction is applied to the visual observations of β Gru.)

The advantage of combining visual and photoelectric photometry observations is that it offers a potentially efficient means to monitor longer-term variations of SR variables where datasets of 100 cycles are probably needed to ascertain adequately the nature and calculate the period of any longer-term variations. Visual observations can be made by more observers more frequently and thus can be used to extend and "fill out" the dataset obtained through more accurate photoelectric measurement. The photoelectric photometry data, however, provide the means to adjust visual observations to the standard UBV system.

Three significantly different software packages were used to search for periodicity in the data. The similarity between the three sets of results obtained for θ Aps suggests that there may be no clear case for choosing one particular software package over another—the choice being mainly a matter of personal preference and familiarity with the software. Also, weighting the

data did not appear to make a substantial difference to the results obtained for the predominant period and only a small difference for the possible secondary periods.

For θ Aps a predominant period of about 111 days was determined with possibly a longer period variation, ~1,200 days or so, and maybe a smaller, shorter-period variation of around 100 days. The longer-period variation for θ Aps is about ten times the predominant period; this longer-term variation of about an order of magnitude slower than the predominant pulsation period is observed in about 25% of semiregular variables (Olivier and Wood 2003). The phenomenon, also known as Long Secondary Periods (LSPs), is yet to be fully explained (Wood *et al.* 2004); if confirmed, θ Aps is one of the brightest southern LSP variables and hence a favorable target for further detailed investigations (e.g., using interferometry).The hint of a shorter-period variation of around 100 days for θ Aps would give a period ratio of 1.1. This ratio, which gives rise to "beating" in the light curve, is also observed in other SR variables (Kiss *et al.* 1999). A combination of radial and non-radial oscillations may explain this phenomenon.

References

Allen, C. W. 1973, *Astrophysical Quantities*, 3rd ed., Univ. London, Athlone Press, London.

Barberá, R. 1996, "Introducing AVE," URL: http://www.astrogea.org/soft/ave/aveint.htm

Böhm-Vitense, E. 1981, *Ann. Rev. Astron. Astrophys.*, **19**, 295.

Cox, A. N. 2000, *Allen's Astrophysical Quantities*, 4th ed., Springer-Verlag, New York.

Henden, A. A., and Kaitchuck, R. H. 1990, *Astronomical Photometry*, Willman-Bell, Richmond, Virginia.

Kiehling, R. 1987, *Astron. Astrophys., Suppl. Ser.*, **69**, 465.

Kiss, L. L., Szatmáry, K., Cadmus, R. R., Jr., and Mattei, J. A. 1999, *Astron. Astrophys.*, **346**, 542.

Lenz, P., and Breger, M. 2007, PERIOD04, (http://www.univie.ac.at/tops/Period04).

Maciejewski, G. 2005. "PERSEA 2.01, Period Search Program for Windows," (http://www.astri.uni.torun.pl/~gm/software.html).

Mermilliod, J. C., Hauck, B., and Mermilliod, M. 1997, "The General Catalogue of Photometric Data (GCPD). II," *Astron. Astrophys., Suppl. Ser.*, **124**, 349.

Olivier, E. A., and Wood, P. R. 2003, *Astrophys. J.*, **584**, 1035.

Optec, Inc. 2007, *Model SSP-5 Generation 2 Photoelectric Photometer* (Technical Manual), URL: http://www.optecinc.com/ssp_5_generation2.pdf

Otero, S., Fraser, B., and Lloyd, C. 2001, *Inf. Bull. Var. Stars*, No. 5026.

Otero, S., and Moon T. 2006, *J. Amer. Assoc. Var. Star Obs.*, **34**, 156.

Percy, J. R., and Harrett, A. 2004, *J. Amer. Assoc. Var. Star Obs.*, **33**, 34.
Simonsen, M. A. 2004, *J. Amer. Assoc. Var. Star Obs.*, **33**, 65.
Toone, J. 2005, *J. Amer. Assoc. Var. Star Obs.*, **34**, 76.
Wood, P. R., Olivier, E. A., and Kawaler, S. D. 2004, *Astrophys. J.*, **604**, 800.

Table 1. A summary of the comparative advantages and disadvantages of visual and photoelectric photometry (PEP) observations.

	Visual estimates	*PEP measurements*
Advantages	Minimal equipment and technical training required.	Accurate measurements of magnitudes and color indices to 0.02 magnitude or better.
	Results obtained with relative ease not requiring extensive processing of data.	Additional information (color indices) obtained through use of different filters.
	Can be undertaken in poorer seeing conditions.	Systematic corrections can be applied for color differences and atmospheric extinction.
Disadvantages	Quality of results is highly dependent on the skill of the observer, with precision seldom better than 0.1 magnitude and the error of an individual observation being typically 0.3 magnitude.	Requires significant investment in equipment and technical training.
	Significant scope for human bias to be introduced.	Involves significant effort both to obtain and process the data.
	Limited to visual wavelengths.	Highly dependent on seeing conditions.
	Difficulty in systematically correcting for color differences between stars and the effects of atmospheric extinction.	

Table 2. Summary of the results from the analysis using PERSEA, giving the period of the dominant peak and an estimate of the precision in its determination, the mean *V* magnitude calculated, the range in the light curve, and the number of points used in the analysis.

Parameter	Period (days)	V$_{mean}$	Range in V	Nr. of Points
Visual	110.6 ± 0.2	5.42	1.50	431
PEP	111.1 ± 0.2	5.37	1.52	200
Combined	111.1 ± 0.1	5.37	1.58	631

Table 3. Results of analyses for photoelectric photometry data only.

	Period (days)		Amplitude	
	weighted	non-weighted	weighted	non-weighted
1 (main)	111.1	111.2	0.39	0.35
2	1260	1203	0.24	0.2
3	103	100	0.20	0.16

Table 4. Results of the analyses for both weighted and non-weighted visual data.

	Period (days)	
	weighted	non-weighted
1 (main)	110.6	110.6
2	965	926
3	99.3	99.4

Table 5. Results of combining photoelectric photometry and visual data.

	Period (days)	
	weighted	non-weighted
1 (main)	111.0	110.6
2	1297	1002
3	101.1	99.3
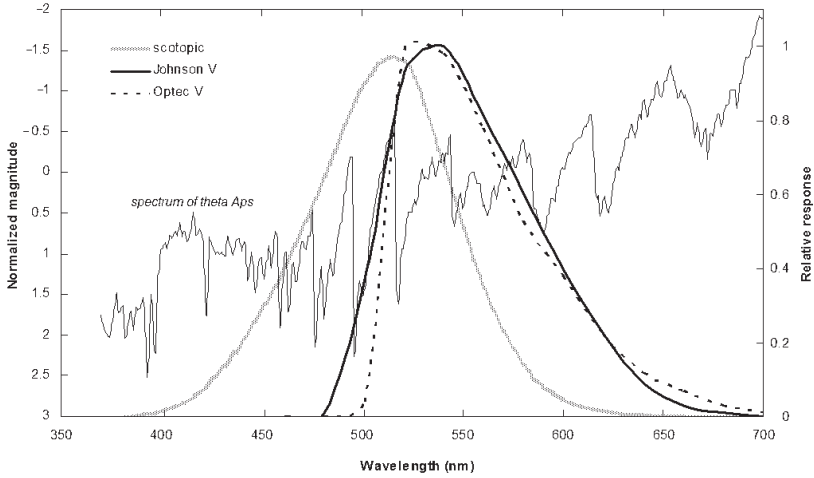
Figure 1. A comparison of the spectral responses of the dark-adapted human eye (Allen 1973; Cox 2000) and the Optec photometer (Optec, Inc. 2007) used for the photoelectric measurements presented in this paper, with that of the standard, photoelectric *V*-band (Allen 1973).
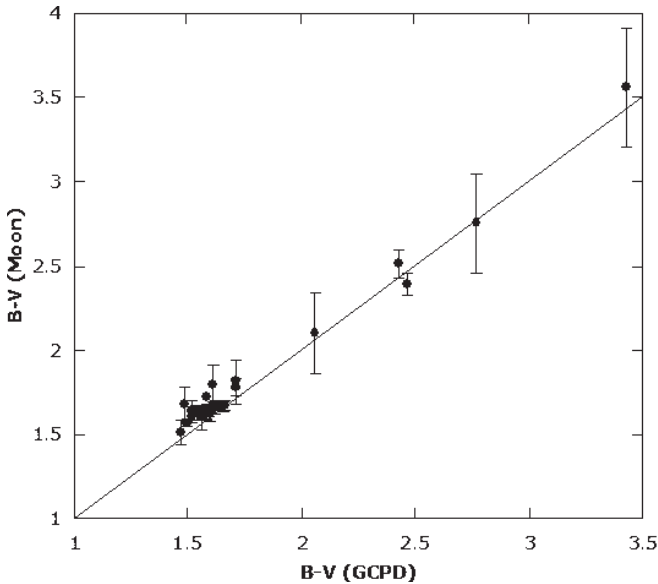
Figure 2. A plot of the measured *B–V* indices as a function of the GCPD values for thirty southern, bright SR variables. Also plotted is the line for a one-to-one correspondence between the *B–V* measurements and listed GCPD values.
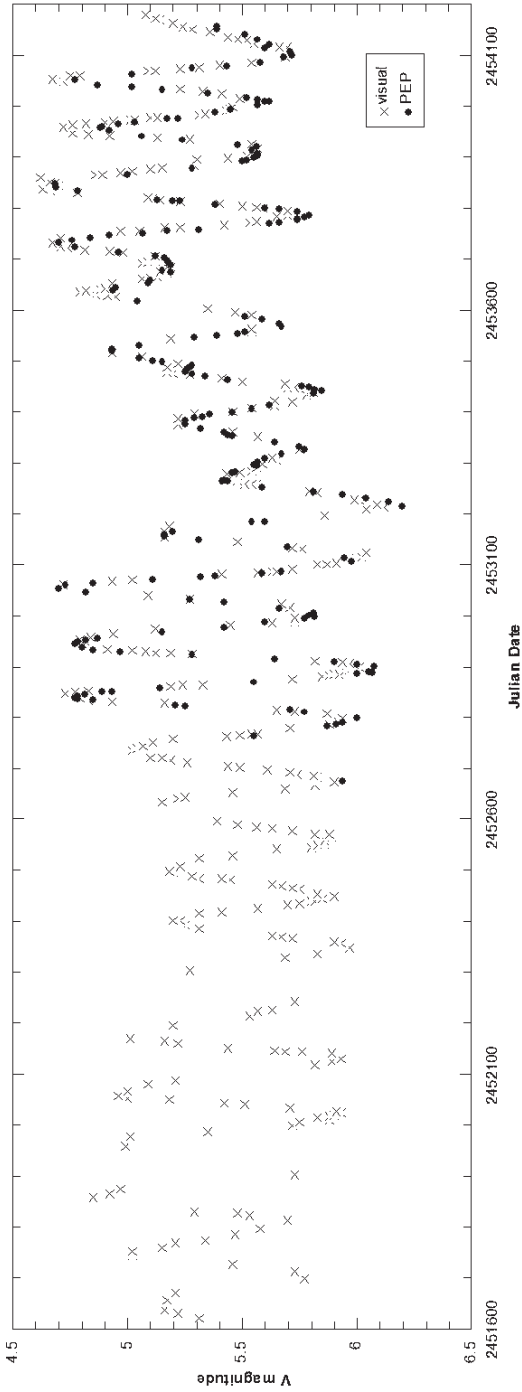
Figure 3. New visual and photoelectric photometry observations of θ Aps with a correction of −0.05 magnitude applied to the visual estimates.

The Exciting Star of the Berkeley 59/Cepheus OB4 Complex and Other Chance Variable Star Discoveries

Daniel J. Majaess
David G. Turner
Department of Astronomy and Physics, Saint Mary's University, Halifax, NS, B3H 3C3, Canada

and

Visiting Astronomer, Dominion Astrophysical Observatory, Herzberg Institute of Astrophysics, National Research Council of Canada

David J. Lane
Department of Astronomy and Physics, Saint Mary's University, Halifax, NS, B3H 3C3, Canada

and

Abbey Ridge Observatory, Stillwater Lake, NS, Canada

Kathleen E. Moncrieff
Department of Astronomy and Physics, Saint Mary's University, Halifax, NS, B3H 3C3, Canada

Abstract   A study is presented regarding the nature of several variable stars sampled during a campaign of photometric monitoring from the Abbey Ridge Observatory: three eclipsing binaries, two semiregulars, a luminous Be star, and a star of uncertain classification. For one of the eclipsing systems, BD+66°1673, spectroscopic observations reveal it to be an O5 V((f))n star and the probable ionizing star of the Berkeley 59/Cep OB4 complex. An analysis of spectroscopic observations and *BV* photometry for Berkeley 59 members in conjunction with published observations imply a cluster age of ~2 Myr, a distance of d = 883 ±43 pc, and a reddening of E_{B-V} = 1.38 ±0.02. Two of the eclipsing systems are Algol-type, but one appears to be a cataclysmic variable associated with an X-ray source. ALS 10588, a B3 IVn star associated with the Cepheid SV Vul, is of uncertain classification, although consideration is given to it being a slowly pulsating B star. The environmental context of the variables is examined using spectroscopic parallax, 2MASS photometry, and proper motion data, the latter to evaluate the membership of the variable B2 Iabe star HDE 229059 in Berkeley 87, an open cluster that could offer a unique opportunity to constrain empirically the evolutionary lineage of young massive stars. Also presented are our null results for observations of a sample of

northern stars listed as Cepheid candidates in the *New Catalogue of Suspected Variable Stars* (NSV, in Samus *et al.* 2004).

1. Introduction

The present study is the result of a survey of variable stars initiated at the Abbey Ridge Observatory (ARO). Most of the discoveries resulted from the variability of potential reference and check stars in the fields of Cepheid variables, the campaign's primary objective being to establish period changes for northern hemisphere Cepheids (Turner 1998; Turner *et al.* 1999). In two cases the interest lies in cluster stars discovered to be variable.

The program began in 1996 at the Burke-Gaffney Observatory (BGO) of Saint Mary's University, and was recently transferred to the ARO, which is located at a darker site. The stability of the ARO site and an upgrading of the photometric reduction routines facilitated the discoveries, some of which are described here. A preliminary survey was also made of stars in the *New Catalogue of Suspected Variable Stars* (NSV, in Samus *et al.* 2004) thought to be potential Cepheid variables, with the goal of expanding the Galactic sample and eventually studying their period changes. Rate of period change, in conjunction with light amplitude, has been demonstrated to be an invaluable parameter for constraining a Cepheid's crossing mode and likely location within the instability strip (Turner *et al.* 2006a). Such constraints permit further deductions to be made concerning a Cepheid's intrinsic reddening and pulsation mode, and offer yet another diagnostic tool for establishing Cepheids as members of open clusters, such calibrators being the foundation for the extragalactic distance scale (Turner and Burke 2002).

The photometric signatures of some variable stars can be sufficiently ambiguous that spectroscopic follow-up was necessary to resolve the true nature of the light variations. Preliminary results for the best-studied of the variables, summarized in Table 1, are presented here in order of increasing right ascension. The results for the NSV stars are given in Section 3.8..

2. Observations and equipment

The ARO is located in Stillwater Lake, a community ~23 km west of Halifax, Nova Scotia, Canada. The ARO allocated about two hours of observing time on each clear night in support of this research, with much of the remainder used to search for extragalactic supernovae and to participate in AAVSO observing campaigns and *AAVSO Special Notice* and *Alert Notice* targets. The site is quite dark, with typical Sky Quality Meter readings of 20.6 *V* mag. arcsec^{-2} on good nights. The observatory houses a 28-cm Celestron Schmidt-Cassegrain telescope equipped with an SBIG ST9-CCD camera and Bessel *B* and *V* filters. The facility is remotely accessible and completely automated, allowing unattended acquisition of astronomical and calibration images and providing a

software pipeline that calibrates, combines, and performs differential aperture photometry. Much of the design and software development to realize the ARO's capability was completed in the form of the Abbey Ridge Auto-Pilot software (Lane 2007). Other software, in particular MAXIM DL/CCD (George 2007), provides many of the low-level image acquisition and processing functions.

Observations and image processing are guided by two data files provided by the observer. The first contains relevant information about each field to be imaged, including a unique identifier, center equatorial coordinates, and exposure times and number of exposures to be taken in each filter. If aperture photometry is to be performed automatically on the field, additional information is needed, including aperture photometry parameters, magnitude of the designated reference star, and equatorial co-ordinates for each star to be measured. The second file type contains a list of target fields (identifiers) to be observed on a given night.

All resulting photometric data represent means for multiple (15–25, or more) short-exposure images, typically of 1 to 60 seconds duration, taken in immediate succession, combined using a noise-reduction algorithm developed by DJL. The algorithm first calibrates the individual images instrumentally, then registers them spatially using stars in the field. The mean and standard deviation are computed for each pixel position in the stack of images. Pixels on a given image that deviate more than a specified number of standard deviations from the mean of pixels at the same pixel positions on the other images are rejected, and a new mean is computed. The process is iterated up to five times until all deviant pixels are rejected, although no more than 30% of the pixels at a given pixel position are ever rejected. The resulting mean, without inclusion of rejected pixels, is used to form the combined image, which is plate-solved astrometrically using the PinPoint Astrometric Engine software (Denny 2007).

Differential aperture photometry is performed on each combined image using initial aperture and sky annulus parameters, and equatorial co-ordinates of the primary target star, reference star, and any number of "check" or other stars. The sky annulus radius and size are pre-selected for each field to be appropriate for all stars measured. The equatorial position of each star is converted to its corresponding X and Y pixel position using the plate solution embedded in the fts header. Aperture photometry is performed on the reference star three times iteratively to determine its precise X and Y pixel position and full-width half maximum (FWHM) seeing disk. A new aperture size is set to a pre-determined multiple of the measured FWHM, and the sky annulus position is adjusted so that it remains at the original radius from the star's center. The new aperture parameters and the same technique are used for the remaining stars measured. The instrumental magnitude derived for the reference star is used to convert instrumental magnitudes for the remaining stars into differential magnitudes.

The output for each measured star includes pertinent information, such as FWHM, sky annulus background, signal-to-noise ratio, and maximum pixel

value, all of which are invaluable when assessing the data quality. In most instances the reference stars are selected from the comprehensive *Tycho-2* catalogue (Høg *et al.* 2000), so there may be zero-point offsets, given that the reference stars are non-standards and the photometry is not explicitly normalized to the Johnson system. Also, differences in color between the reference and target stars are not normally taken into account.

The spectra used to classify the variables were obtained during two observing runs with the Dominion Astrophysical Observatory's 1.8-m Plaskett telescope. During the first run in October 2006, the SITe-2 CCD detector was used to image spectra at a resolution of 120 Å mm^{-1} centered on 4740 Å. For the second run in October 2007, the SITe-5 CCD detector was used to image spectra at a resolution of 60 Å mm^{-1} centered on 4200 Å. The spectra were reduced and analyzed using the NOAO's routines in IRAF along with software packages by Christian Buil (IRIS), Valérie Desnoux (VSPEC), and Robert H. Nelson (RAVEREC). Lastly, a search for periodicity in the photometry of periodic variables in the sample was carried out in the PERANSO software environment (Vanmunster 2007) using the algorithms ANOVA (Schwarzenberg-Czerny 1996), FALC (Harris *et al.* 1989), and CLEANEST (Foster 1995).

3. Comments on individual stars

3.1. BD+66°1673 (EA, O5 V((f))n)

BD+66°1673 lies on the northwestern edge of Berkeley 59, an open cluster embedded in an H II region (Figure 1) at the core of the Cep OB4 association. The star was classified previously from objective-prism spectra as O9-B0 (MacConnell 1968; Walker 1965), but is reclassified as O5 V((f))n from a spectrum at 60 Å mm^{-1} obtained at the DAO (Figure 2). BD+66°1673 now has the distinction of being the hottest star in Cep OB4. The star's implied high temperature drives mass loss via strong stellar winds that may be largely responsible for shaping and illuminating the surrounding H II region, along with playing a role in the formation of clearly-visible, cold, molecular pillars (Yang and Fukui 1992; Gahm *et al.* 2006).

BD+66°1673 was monitored as part of a search for variable stars in Berkeley 59, and was the first to exhibit convincing brightness variations. A period analysis of the photometry revealed a strong signal for $P = 5.33146$ ±0.00020 days. The phased light curve (Figure 3) is that of an Algol-type eclipsing binary system, with primary and secondary eclipse depths of ~0.13 and ~0.06 magnitude, although with eclipses skewed in phase indicating an eccentric orbit of $e \simeq 0.3$ and longitude of periastron $\omega \simeq 180°$. Our adopted ephemeris for light minimum in the system from regression fits for the light curve is:

$$\text{HJD}_{\text{min}} = 2454400.5322 + 5.33146 \text{ E.}$$
$$\pm0.0002 \quad \pm0.0002$$

For the inferred stellar mass and temperature of the primary, a preliminary model generated for the system using BINARY MAKER 3 (Bradstreet and Steelman 2004) constrains the companion to be an early-to-mid B-type star (B2-B3, say) in a system with an orbital inclination of ~75°. A more detailed photometric study is needed to generate a full light curve to confirm the orbital eccentricity as well as to permit a more detailed analysis.

The distance to BD+66°1673 can be established from its likely membership in Berkeley 59 and Cep OB4, despite a spatial location outside the cluster nucleus. We obtained all-sky *BV* photometry of the cluster field on five nights, derived extinction coefficients using the techniques outlined by Henden and Kaitchuck (1998), and standardized the photometry to the Johnson system using stars in the nearby cluster NGC 225 (Hoag *et al.* 1961). Our data for cluster stars for which we have spectroscopic results are given in Table 2.

BV photometry does not permit one to assess the properties of the dust extinction in the field, and for that we must rely on the *UBV* photometry obtained by MacConnell (1968) for bright association members. A complete reanalysis is indicated, given that MacConnell (1968) derived different values for the ratio of total to selective extinction (R_V) for different stars and regions of Cep OB4. Unusual reddening properties for the dust in the field were first suggested by Blanco and Williams (1959) in their study of Cep OB4. Such properties, if confirmed, would limit the accuracy of any derived distance to the cluster and association stars. We therefore decided to reanalyze the R_V estimate from the available photometric and spectroscopic data.

The new spectral classifications for Cep OB4 stars (Figure 2, Table 2) can be used with the *UBV* photometry of MacConnell (1968) to establish the reddening law for the dust in the field. The result for the four brightest stars is a reddening slope of $X = 0.80 \pm 0.01$, identical to the reddening parameters inferred for dust obscuring nearby fields in Cygnus (Turner 1989). The observed *UBV* colors were dereddened with that reddening law and either zero-age main-sequence (ZAMS) luminosities from Turner (1976, 1979) or main-sequence luminosities for obvious non-ZAMS stars, with results presented in the variable-extinction diagram of Figure 4. Some stars have colors systematically too blue for their observed spectral types, a feature encountered for many early-type emission-line stars (Schild and Romanishin 1976). The reddening law in Cep OB4 is reasonably well defined by the data, and the slope of the relation depicted in Figure 4 is $R_V = 2.81 \pm 0.09$ from least squares and non-parametric straight line fits. The slope is consistent with the properties of nearby dust clouds (Turner 1996b).

The distance to Berkeley 59 and Cep OB4 follows from a ZAMS fit, which gives $V_0 - M_V = 9.73 \pm 0.11$, corresponding formally to $d = 883 \pm 43$ pc. A main-sequence fit to our new photometry for stars in the core of Berkeley 59 (Table 2) is shown in Figure 5 along with data for association members. The results reveal another feature, namely an excess reddening for the B8 III star 2MASS 00021063+6724087: $E_{B-V} = 1.5$ relative to $E_{B-V} = 1.38 \pm 0.02$ for

other, spatially-adjacent, cluster members. 2MASS 00021063+6724087 may be an example of a rotating star embedded in a dust torus (see Turner 1996a), and its location in Figure 5 is consistent with a star near the turn-on point for pre-main-sequence objects.

The cluster radial velocity can be deduced by merging observations from Crampton and Fisher (1974) and Liu *et al.* (1989, 1991), which yields $V_R = -7$ ±15 km s^{-1} for BD+66°1674, and -8 ± 31 km s^{-1} for BD+66°1675. Crampton and Fisher (1974) noted that scatter in the radial velocities for both objects suggested they are spectroscopic binaries. A period search reveals putative periods of $P = 1.20$ days and $P = 5.30$ days for BD+66°1674. The results are sufficiently interesting to justify additional radial velocity measures, which are essential to establish a unique solution.

The presence of a O5 V((f))n star in Berkeley 59 and the predominance of late B-type cluster members lying above the ZAMS indicates an extremely young cluster. An age of $\sim2 \times 10^6$ years for Berkeley 59 is estimated from BD+66°1673 and the luminosities of stars lying near the cluster turn-on point in Figure 5 (see Guetter and Turner 1997), marking Berkeley 59 as one of the youngest and nearest clusters known. Certainly O5 V((f))n stars are rarely encountered in our Galaxy within a kiloparsec of the Sun. Much like Berkeley 87 discussed later, Berkeley 59 contains a sufficient number of exotic stars to make it an object of intense interest for future studies.

3.2. 2MASS 00104558+6127556 (EA, A9 V)

The star 2MASS 00104558+6127556 was found to vary in light during monitoring of the Cepheid BD Cas. A dominant period of $P = 2.7172 \pm0.0002$ days produces a light curve (Figure 3) indicating an Algol-type eclipsing system with eclipse depths of ~0.43 magnitude for primary minimum and ~0.31 mag. for secondary minimum. Our adopted ephemeris for light minimum in the system from regression fits for the light curve is:

$$\text{HJD}_{min} = 2454404.8586 + 2.7172 \text{ E.}$$
$$\pm0.0002 \quad \pm0.0002$$

A spectrum (Figure 6) indicates a spectral type near A9 V, but with some features that may indicate contamination by a companion. For the inferred stellar mass and temperature of the primary, a preliminary model generated for the system using BINARY MAKER 3 (Bradstreet and Steelman 2004) constrains the companion to be a mid F-type star (F4-F5, say) in a system with an orbital inclination of ~88°. Additional observations are needed to refine the period and to establish a complete light curve for a formal analysis.

3.3. 2MASS 19064659+4401458 (XI?, G2 V)

2MASS 19064659+4401458 lies in the field of the nova-like cataclysmic variable MV Lyr, and was found to display a low level of variability while monitoring the suspected Cepheid NSV 11753 (see Section 3.8). The star's

variability was presumably discovered by Weber (1959, number 90 in his list), although it is misidentified in the original finder chart as a different star of constant brightness located a mere 1.4 arcminutes away (NSV 11753, J2000 R.A. 19^h 06^m 54.19^s, Dec. $+44°$ $02'$ $55.5"$). There is X-ray emission at a flux level of 2.21×10^{-2} counts s^{-1} from within an arcminute of the object (ROSAT ASSC source J190645.9+440139, Voges *et al.* 2000) that is distinct from an X-ray flux of 1.26×10^{-2} counts s^{-1} associated with MV Lyr itself (ROSAT ASSC source J190716.8+440109, Voges *et al.* 1999). The object's spectral type is G2 V (Figure 6), and its spectroscopic parallax (below) implies an X-ray luminosity of $L_X \simeq 10^{30}$ ergs s^{-1}, as estimated using the energy conversion factor of Huensch *et al.* (1996). The result is too low for a canonical low-mass X-ray binary ($L_X \geqq 10^{36}$ ergs s^{-1}), but is similar to that of W UMa systems ($L_X \sim 10^{29-30}$ ergs s^{-1}, Chen *et al.* 2006), chromospherically active stars (i.e., RS CVn variables), and compact binaries.

A preliminary period analysis resulted in a dominant signal corresponding to $P \simeq 7.0$ days, which is consistent with the initial estimate by Weber (1959) of 8 days, and agrees with more recent estimates by Boyd (2008, private communication) and Lloyd (2008, private communication). The phased light curve in Figure 3 displays a brief eclipse superposed on more rapid, irregular, quasi-sinusoidal variations. The possibility that 2MASS 19064659+4401458 is a close contact system is inconsistent with the inferred period, and chromospheric activity in the primary is precluded by the absence of Ca II H and K emission in its spectrum.

An alternative scenario would associate irregularities in the light curve with frictional heating in an accretion disk, implying that 2MASS 19064659+4401458 is a semi-detached binary system consisting of a G dwarf overfilling its Roche surface and orbiting a compact companion, presumably a white dwarf. During eclipses the irregular variations disappear, implying that they originate from a hot spot in the accretion disk that is eclipsed by the G2 dwarf. It is hoped that the preliminary results presented here will motivate additional observers to join an ongoing campaign led by variable star observer David Boyd, with a group including Richard Huziak, Roger Pickard, Tomas Gomez, Gary Poyner, Tom Krajci, and Bart Staels, to constrain the period and further investigate the star. An understanding of the system via optical photometry, however, may be limited by the nature of the source driving the irregular variations. Time-series spectroscopy is also needed to assess the full nature of the system.

The object's distance is estimated from the canonical distance modulus relation reformulated for the infrared, namely with $A_J = 0.276 \times A_V$ and $E_{J-H} = 0.33 \times E_{B-V}$ (Bica and Bonatto 2005; Dutra *et al.* 2002). The 2MASS magnitudes for the star are $J = 11.275 \pm 0.020$, $H = 10.776 \pm 0.018$, and $K = 10.650 \pm 0.016$ (Cutri *et al.* 2003), and an absolute magnitude and intrinsic color can be established from the star's main-sequence spectral type as $M_J = 3.24 \pm 0.53$ and $(J-H)_0 \simeq 0.28 \pm 0.06$, parameters deduced from a sample of $n \simeq 30$ G2 V stars in the Hipparcos database (Perryman *et al.* 1997) with cited

parallax uncertainties $\lesssim 0.7$ mas. The implied intrinsic color agrees with a value of $(J–H)_0 \simeq 0.38$ from Koornneef (1983), when converted to the 2MASS system with the appropriate transformation (Carpenter 2001). The resulting distance for $R_V = 3.1$ is $d \approx 310$ pc, while, if a nearly negligible field reddening is adopted, as advocated by a 2MASS color-color diagram of the region, it is $d \simeq 400$ pc.

3.4. BD+22°3792 (SRB, M6 III)

The variability of BD+22°3792, of spectral type M6 III (Shi and Hu 1999, see Figure 6), was discovered by the ASAS survey (Pojmański *et al.* 2005). The semi-periodic nature of its photometric variations (Figure 7) and its spectral type are consistent with a Type B semiregular variable. A Fourier analysis of our observations and those of ASAS-3 implies a possible period around 79 days. The star's spectral energy distribution displays far-infrared emission, indicating the presence of a warm dusty envelope surrounding the star, likely stemming from mass loss.

BD+22°3792 is 12' from the open cluster NGC 6823, but is not a member. The cluster's associated H II region is excited by numerous, young, reddened, OB stars, which are $\sim 4–7 \times 10^6$ years old at a distance of $d = 2.1 \pm 0.1$ kpc (Guetter 1992). The star's distance can be estimated by spectroscopic parallax using photometry taken from Massey *et al.* (1995) and a set of intrinsic parameters, $M_V = –0.3 \pm 0.7$ and $(B–V)_0 = 1.36 \pm 0.09$, derived from a sample of $n = 7$ nearby M6 giants in the Hipparcos database (Perryman *et al.* 1997) with cited parallax uncertainties $\lesssim 0.9$ mas. The intrinsic parameters for M6 giants in the literature are rather scattered (see Mikami 1986, and references therein), mainly because most are variable and exhibit intrinsic color excesses. The resulting distance to BD+22°3792 is ~ 700 pc for a reddening of $E_{B–V} \simeq 0.38$ from the Hipparcos data, while adoption of an intrinsic color of $(B–V)_0 = 1.58$ from Lee (1970) gives $d \simeq 950$ pc and $E_{B–V} \simeq 0.18$.

3.5. 2MASS 19475544+2722562 (SRB, M4 III)

The star 2MASS 19475544+2722562 lies in the field of the Cepheid S Vul. Its light curve (Figure 7) exhibits a nearly regular oscillatory trend superimposed upon a gradual increase in brightness. The star's late spectral type of M4 III (Figure 6) suggests a likely designation as a Type B semiregular. A Fourier analysis suggests a rather short period of ~ 27 days for the oscillatory trend.

3.6. ALS 10588 = LS II+27 19 (SPB? ELL?, B3 IVn)

Alma Luminous Star 10588 (Reed 1998), or LS II+27 19 (Stock *et al.* 1960), is a close spatial neighbor of the Cepheid SV Vul, and a likely member of Vul OB1 (Turner 1980, 1984). The star's evolutionary status from its spectral type (B3 IVn, Figure 6) matches that of stars associated with SV Vul, namely main-sequence objects terminating at B3. Spectroscopic parallax places the star at a distance of 2040 ±470 pc, consistent with the distance to Vul OB1 (d

= 2.1–2.5 kpc, Turner 1986; Guetter 1992). ALS 10588 exhibits an IR excess with emission at 60 μm and 100 μm in the IRAS survey (IRAS19498+2717), which might account for its larger space reddening of $E_{B-V} = 0.79 \pm 0.02$ relative to a value of $E_{B-V} = 0.50$ for SV Vul, provided that the former possesses an equatorial dust torus (see Turner 1996a).

The variability of ALS 10588 was revealed during monitoring of SV Vul, although it also appears to have been detected in a *V* and *I* survey for new Cepheids by Metzger and Schechter (1998). A period analysis of the photometry revealed a dominant signal at $P = 1.8521 \pm 0.0005$ days, although a solution for twice that value ($P = 3.704$ days) matches our observations and those of ASAS (Pojmański *et al.* 2005) (Figure 8). The spectral type and period are consistent with the class of slowly pulsating B stars (SPBs), characterized by stars of spectral types B3-B8 oscillating with periods on the order of days (Waelkens and Rufener 1985). The observed *V* amplitude ($\simeq 0.25$ mag.), however, is unusually large for a SPB variable (De Cat *et al.* 2000). Similarly, if twice the period is adopted, the inferred ellipsoidal system has a light amplitude more than twice that observed in other B stars of the same class (Beech 1989). There is also an absence of spectroscopic contamination from the expected companion (Figure 6). A toroidal dust clump orbiting synchronously with the star would account for the IR excess as well as the star's excess reddening (Turner 1996a), and, if tied to the star's rotation, would imply a stellar rotational velocity of ~250 km s^{-1}, consistent with the slightly diffuse nature of the star's spectrum. Yet there is no significant deviation from a repeatable light curve morphology over several seasons of observation. The star's status may ultimately need to be resolved by time-series spectroscopy to examine whether the resulting radial velocities are consistent with the trend noted for SPBs (De Cat and Aerts 2002), or the canonical features of binarity or extrinsic variability.

3.7. HDE 229059 (α Cyg variable, B2 Iabe)

HDE 229059 is a B2 Iabe supergiant that displays emission in the lower hydrogen Balmer lines (Figure 6) and has an infrared (IR) excess (Clarke *et al.* 2005). Such characteristics indicate active mass loss and the presence of circumstellar dust. The *General Catalogue of Variable Stars* (GCVS, in Samus *et al.* 2004) designates stars with comparable spectral types and *V* amplitudes ($\simeq 0.1$ mag, Figure 7) to those of HDE 229059 as α Cyg variables, with irregular light variations tied to overlapping modes of non-radial pulsation. Burki *et al.* (1978) suggest that all luminosity class Ia B-G supergiants probably vary in brightness (see also Bresolin *et al.* 2004, and references therein).

HDE 229059 lies in Berkeley 87, an open cluster that has received considerable attention because it is a strong source of γ– and cosmic rays (Giovannelli 2002; Aharonian *et al.* 2006), which has motivated an area of research on how stellar winds interact with the interstellar medium, enabling young open clusters to become pseudo particle accelerators. Berkeley 87 also hosts an abundance of astronomical phenomena (compact H II regions,

molecular clouds, masers, and radio sources) and exotic stellar constituents that includes V439 Cyg, Stephenson 3, and BC Cyg. V439 Cyg is an emission-line star that has exhibited dramatic spectroscopic changes over a short time-scale (Polcaro *et al.* 1990; Polcaro and Norci 1997; Norci *et al.* 1998; Polcaro and Norci 1998), Stephenson 3 is a rare type of Wolf-Rayet star (WO3) (Norci *et al.* 1998; Polcaro *et al.* 1997), and BC Cyg is an M3 Ia supergiant and type C semiregular variable (Turner *et al.* 2006b) that will eventually terminate in a Type II supernova explosion. The cluster therefore offers intriguing insights into the effects of initial mass and mass loss on the end states of evolution for O-type stars, and may allow us to place new constraints on the initial progenitor masses for WO stars and red supergiants. The situation of HDE 229059 in such an evolutionary scheme is not entirely clear, which is why further study is essential. As a start, we investigate the possibility of cluster membership for the stars using spectroscopic parallax, 2MASS photometry, and proper motion data.

The distance to HDE 229059 can be established by spectroscopic parallax using the photometry of Turner and Forbes (1982) and intrinsic parameters determined from a sample of blue supergiants: $M_V = -6.4 \pm 0.8$ and $(B-V)_0 = -0.19 \pm 0.03$ (Kudritzki *et al.* 1999; Blaha and Humphreys 1989; Garmany and Stencel 1992), values that compare favorably with unpublished results (Turner) of $M_V = -6.3$ and $(B-V)_0 = -0.18$ for B2 Iab stars. The distance for $R_V = 3.0$ is $d = 970$ pc. For BC Cyg, with mean $<V>$ and $<B-V>$ from Turner *et al.* (2006b) and intrinsic parameters derived for the comparable M-type supergiant α Orionis, the resulting distance is $d \simeq 1200$ pc.

2MASS photometry (Cutri *et al.* 2003) for the cluster field yields color-color and color-magnitude diagrams for Berkeley 87 presented in Figure 9. The reddening solution, $E_{J-H} = 0.42 \pm 0.04$ ($E_{B-V} \simeq 1.36$), is well-defined because of the presence of numerous young B-type stars in the cluster. Isochrones for the 2MASS system (Padova Database of Stellar Evolutionary Tracks and Isochrones, Bonatto *et al.* 2004) fit the data at a distance of $d = 1280 \pm 150$ pc. The reddening matches previous results, but the distance is larger than that found by Turner and Forbes (1982), although consistent with a later estimate of 1230 ± 40 pc (Turner *et al.* 2006b). Constraining the cluster's age from 2MASS data is complicated by the fact that BC Cyg lies near the saturation limit of the survey. The isochrone fit in Figure 9 is provided mainly to highlight the envisioned evolution, although high mass loss rates are indicated and the plotted isochrone is more closely linked with conservative mass evolution.

Proper motion data (Zacharias *et al.* 2004) exist for several bright stars whose membership in Berkeley 87 is supported by their locations in Figure 9, and can be compared with the similar values found for HDE 229059, BC Cyg, and Stephenson 3 (Table 3). The proper motions for such distant stars are small and may be dominated by measuring uncertainties. Consequently, we can only argue that a physical association between the above stars and the cluster cannot be excluded on the available evidence. Membership of the exotic variable stars of Berkeley 87 would be strengthened by radial velocity measures.

3.8. NSV variables

A number of stars from the *New Catalogue of Suspected Variable Stars* (NSV, in Samus *et al.* 2004) were surveyed in a search for potential small-amplitude Cepheids. Reference stars of well-established magnitude in each field were not available, so the observations were made differentially relative to other stars in the field, with unknown zero-point. The coordinates provided by the original sources are estimated to be uncertain by several arcminutes or more, which led us to make photometric sweeps of the immediate field to find objects that might correspond to the suspected variables. There are stars that are reasonably coincident with the co-ordinates for the NSV variables listed in Table 4, but none appear to be light variable. Listed in Table 4 are the co-ordinates from the NSV for the suspected variables, magnitudes from Samus *et al.* (2004), the standard deviation of the magnitude estimates for the stars selected in the present survey, and the number of observations made. None of the stars identified here in the fields of the suspected Cepheid variables displayed the canonical light variations expected, although other types of variability cannot be dismissed because of our limited observational sampling.

4. Discussion

It is of interest to note how a program of regular observation of Cepheid variables has generated serendipitous discoveries of new variable stars because of the need to establish photometric standard stars and check stars in the fields of the CCD images. In many cases the variable stars prove to be interesting, possibly unique, objects in their own right. But additional photometric and spectroscopic observations may be essential for clarifying their overall properties.

5. Acknowledgements

References

Aharonian, F., *et al.* 2006, *Astron. Astrophys.*, **454**, 775.
Beech, M. 1989, *Astrophys. Space Sci.*, **152**, 329.
Bica, E., and Bonatto, C. 2005, *Astron. Astrophys.*, **443**, 465.

Blaha, C., and Humphreys, R. M. 1989, *Astron. J.*, **98**, 1598.

Blanco, V. M., and Williams, A. D. 1959, *Astrophys. J.*, **130**, 482.

Bonatto, C., Bica, E., and Girardi, L. 2004, *Astron. Astrophys.*, **415**, 571.

Boyd, D. 2008, private communication.

Bradstreet, D. H., and Steelman, D. P. 2004, *Binary Maker 3 Light Curve Synthesis Program,* Contact Software: Norristown, Pennsylvania.

Bresolin, F., Pietrzyński, G., Gieren, W., Kudritzki, R. -P., Przybilla, N., and Fouqé, P. 2004, *Astrophys. J.*, **600**, 182.

Burki, G., Maeder, A., and Rufener, F. 1978, *Astron. Astrophys.*, **65**, 363.

Carpenter, J. M. 2001, *Astron. J.*, **121**, 2851.

Chen, W. P., Sanchawala, K., and Chiu, M. C. 2006, *Astron. J.*, **131**, 990.

Clarke, A. J., Oudmaijer, R. D., and Lumsden, S. L. 2005, *Mon. Not. Roy. Astron. Soc.*, **363**, 1111.

Crampton, D., and Fisher, W. A. 1974, *Publ. Dom. Astrophys. Obs. Victoria*, **14**, 283.

Cutri, R. M., *et al.* 2003, *The IRAS 2MASS All-Sky Point Source Catalog of Point Sources*, NASA/IPAC Infrared Science Archive.

De Cat, P., and Aerts, C. 2002, *Astron. Astrophys.*, **393**, 965.

De Cat, P., Aerts, C., De Ridder, J., Kolenberg, K., Meeus, G., and Decin, L. 2000, *Astron. Astrophys.*, **355**, 1015.

Denny, R. 2007, *DC-3 Dreams, SP*, PinPoint Astrometric Engine software.

Dutra, C. M., Santiago, B. X., and Bica, E. 2002, *Astron. Astrophys.*, **381**, 219.

Foster, G. 1995, *Astron. J.*, **109**, 1889.

Gahm, G. F., Carlqvist, P., Johansson, L. E. B., and Nikolić, S. 2006, *Astron. Astrophys.*, **454**, 201.

Garmany, C. D., and Stencel, R. E. 1992, *Astron. Astrophys., Suppl.* Ser., **94**, 211.

George, D. 2007, *MaxIm DL/CCD* software, http://www.cyanogen.com.

Giovannelli, F. 2002, *Mem. Soc. Astron. Ital.*, **73**, 920.

Guetter, H. H. 1992, *Astron. J.*, **103**, 197.

Guetter, H. H., and Turner, D. G. 1997, *Astron. J.*, **113**, 2116.

Harris, A. W., *et al.* 1989, *Icarus*, **77**, 171.

Henden, A. A., and Kaitchuck, R. H. 1998, *Astronomical Photometry: A Text and Handbook for the Advanced Amateur and Professional Astronomer*, Willmann-Bell, Inc., Richmond, Virginia.

Hoag, A. A., Johnson, H. L., Iriarte, B., Mitchell, R. I., Hallam, K. L., and Sharpless, S. 1961, *Publ. U. S. Nav. Obs., Second Ser.*, **17**, 343.

Høg, E., *et al.* 2000, *Astron. Astrophys.*, **355**, L27.

Huensch, M., Schmitt, J. H. M. M., Schroeder, K. -P., and Reimers, D. 1996, *Astron. Astrophys.*, **310**, 801.

Koornneef, J. 1983, *Astron. Astrophys.*, **128**, 84.

Kudritzki, R. P., Puls, J., Lennon, D. J., Venn, K. A., Reetz, J., Najarro, F., McCarthy, J. K., and Herrero, A. 1999, *Astron. Astrophys.*, **350**, 970.

Lane, D. J. 2007, Abbey Ridge Observatory and Abbey Ridge Auto-Pilot software, http://www.davelane.ca/aro.

Lee, T. A. 1970, *Astrophys. J.*, **162**, 217.

Liu, T., Janes, K. A., and Bania, T. M. 1989, *Astron. J.*, **98**, 626.

Liu, T., Janes, K. A., and Bania, T. M. 1991, *Astron. J.*, **102**, 1103.

Lloyd, C. 2008, private communication.

MacConnell, D. J. 1968, *Astrophys. J., Suppl. Ser.*, **16**, 275.

Massey, P., Johnson, K. E., and Degioia-Eastwood, K. 1995, *Astrophys. J.*, **454**, 151.

Metzger, M. R., and Schechter, P. L. 1998, *Astron. J.*, **116**, 469.

Mikami, T. 1986, *Astrophys. Space Sci.*, **119**, 65.

Norci, L., Polcaro, V. F., Rossi, C., and Viotti, R. 1998, *Irish Astron. J.*, **25**, 43.

Perryman, M. A. C., *et al.* 1997, The Hipparcos and Tycho Catalogues, ESA SP-1200, ESA Publications Division, Noordwijk.

Pojmański, G., Pilecki, B., and Szczygieł, D. 2005, *Acta Astron.*, **55**, 275.

Polcaro, V. F., and Norci, L. 1997, *Astrophys. Space Sci.*, **251**, 343.

Polcaro, V. F., and Norci, L. 1998, *Astron. Astrophys.*, **339**, 75.

Polcaro, V. F., Rossi, C., Norci, L., and Giovannelli, F. 1990, *Astrophys. Space Sci.*, **169**, 31.

Polcaro, V. F., Viotti, R., Rossi, C., and Norci, L. 1997, *Astron. Astrophys.*, **325**, 178.

Reed, B. C. 1998, *Astrophys. J., Suppl. Ser.*, **115**, 271.

Samus, N. N., Durlevich, O. V., *et al.* 2004, *Combined General Catalogue of Variable Stars*, VizieR Online Data Catalog, II/250.

Schild, R., and Romanishin, W. 1976, *Astrophys. J.*, **204**, 493.

Schwarzenberg-Czerny, A. 1996, *Astrophys. J.*, **460**, L107.

Shi, H. M., and Hu, J. Y. 1999, *Astron. Astrophys., Suppl. Ser.*, **136**, 313.

Stock, J., Nassau, J. J., and Stephenson, C. B. 1960, *Luminous Stars in the Northern Milky Way, II*, Hamburger Sternwarte and Warner and Swasey Observatory, Hamburg-Bergedorf.

Turner, D. G. 1976, *Astron. J.*, **81**, 97.

Turner, D. G. 1979, *Publ. Astron. Soc. Pacific*, **91**, 642.

Turner, D. G. 1980, *Astrophys. J.*, **235**, 146.

Turner, D. G. 1984, *J. Roy. Astron. Soc. Canada*, **78**, 229.

Turner, D. G. 1986, *Astron. Astrophys.*, **167**, 157.

Turner, D. G. 1989, *Astron. J.*, **98**, 2300.

Turner, D. G. 1996a, in *The Origins, Evolutions, and Destinies of Binary Stars in Clusters*, eds. E. F. Milone and J. -C. Mermilliod, Astron. Soc. Pacific Conf. Series, **90**, 382.

Turner, D. G. 1996b, in *The Origins, Evolutions, and Destinies of Binary Stars in Clusters*, eds. E. F. Milone and J. -C. Mermilliod, Astron. Soc. Pacific Conf. Series, **90**, 443.

Turner, D. G. 1998, *J. Am. Assoc. Var. Star Obs.*, **26**, 101.

Turner, D. G., Abdel-Sabour Abdel-Latif, M., and Berdnikov, L. N. 2006a, *Publ. Astron. Soc. Pacific*, **118**, 410.

Turner, D. G., and Burke, J. F. 2002, *Astron. J.*, **124**, 2931.

Turner, D. G., and Forbes, D. 1982, *Publ. Astron. Soc. Pacific*, **94**, 789.

Turner, D. G., Horsford, A. J., and MacMillan, J. D. 1999, *J. Am. Assoc. Var. Star Obs.*, **27**, 5.

Turner, D. G., Rohanizadegan, M., Berdnikov, L. N., and Pastukhova, E. N. 2006b, *Publ. Astron. Soc. Pacific*, **118**, 1533.

Vanmunster, T. 2007, PERANSO Light Curve and Period Analysis Software, http://www.peranso.com.

Voges, W., *et al.* 1999, *Astron. Astrophys.*, **349**, 389.

Voges, W., *et al.* 2000, *IAU Circ.*, No. 7432, 1.

Waelkens, C., and Rufener, F. 1985, *Astron. Astrophys.*, **152**, 6.

Walker, G. A. H. 1965, *Astrophys. J.*, **141**, 660.

Weber, R. 1959, *J. Obs.*, **42**, 106.

Yang, J., and Fukui, Y. 1992, *Astrophys. J.*, **386**, 618.

Zacharias, N., Monet, D. G., Levine, S. E., Urban, S. E., Gaume, R., and Wycoff, G. L. 2004, *Bull. Amer. Astron. Soc.*, **36**, 1418.

Table 1. Monitored variable stars.

Star	RA(2000) h m s	DEC(2000) ° ′ ″	Type	P (days)	Sp. Type
BD+66° 1673	00 01 46.86	+67 30 25.1	E B	5.33146	O5V((f))n
2MASS 00104558 +6127556	00 10 45.58	+61 27 55.6	E B	2.7172	A9 V
2MASS 19064659 +4401458	19 06 46.82	+44 01 46.5	XI?	7.0	G2 V
BD+22° 3792	19 43 53.00	+23 11 36.0	SRB	79.4	M6 III
2MASS 19475544 +2722562	19 47 55.52	+27 22 57.8	SRB	27.3	M4 III
ALS 10588	19 51 52.87	+2 7 25 00.1	SPB?	1.8521	B3 IVn
	—	—	ELL?	3.704	—
HDE 229059	20 21 15.45	+37 24 35.2	α Cyg	—	B2 Iabe

Table 2. Photometry and spectroscopy of Berkeley 59 members.

Star	MacC*	R.A. (2000) h m s	Dec. (2000) ° ′ ″	V	B–V	Sp. Type
BD+66° 1673	3	00 01 46.91	+67 30 24.3	10.07±0.04	1.31±0.03	O5 V((f))n
BD+66° 1675	14	00 02 10.32	+67 24 32.5	9.08±0.03	1.08±0.02	O7 V
BD+66° 1674	13	00 02 10.68	+67 25 44.5	9.60±0.04	1.07±0.02	B0 IIIn
MacConnell 15	15	00 02 13.42	+67 25 05.5	11.30±0.03	1.08±0.02	B0.5 Vn
2MASS 00020012+6725109	A3	00 02 00.17	+67 25 11.2	12.81±0.03	1.20±0.01	B3 V
2MASS 00021063+6724087	—	00 02 10.63	+67 24 08.7	13.43±0.02	1.36±0.03	B8 III

*Numbering from MacConnell (1968).

Table 3. Proper motion data for Berkeley 87 stars.

Star*	Identity	μR.A. (mas/yr)	μDec. (mas/yr)
3	HDE 229059	−4.5 ±0.6	−5.3 ±0.7
4	—	−5.2 ±0.7	−5.5 ±1.0
13	—	−5.6 ±0.7	−7.5 ±0.7
15	V439 Cyg	+1.1 ±5.4	+11.2 ±5.4
25	—	−3.9 ±0.7	−5.7 ±1.1
26	—	−5.7 ±1.3	−4.1 ±2.4
29	Stephenson 3	−8.0 ±5.4	−2.8 ±5.4
32	—	−5.1 ±2.0	−3.1 ±0.7
78	BC Cyg	−4.5 ±1.1	−7.7 ±1.1

*Numbering from Turner and Forbes (1982).

Table 4. Cepheid Candidates from the NSV Catalogue.

Star	R.A. (2000) h m s	Dec. (2000) ° ′ ″	Mag.*	s.d.	n
NSV 00924	02 48 19.91	+58 41 44.8	12.50	±0.003	3
NSV 11753	19 06 54.19	+44 02 55.5	13.50	±0.007	16
NSV 11931	19 21 11.73	+00 07 02.6	14.20	±0.014	7
NSV 14094	22 16 16.71	+49 13 13.8	12.10	±0.008	8
NSV 14237	22 35 04.02	+63 47 37.6	12.30	±0.006	8

*From Samus et al. (2004).

Figure 1. The field of view of Berkeley 59, a pseudo-color image constructed from POSS II data. North is up, east is to the left. The location of BD+66°1673 is indicated.
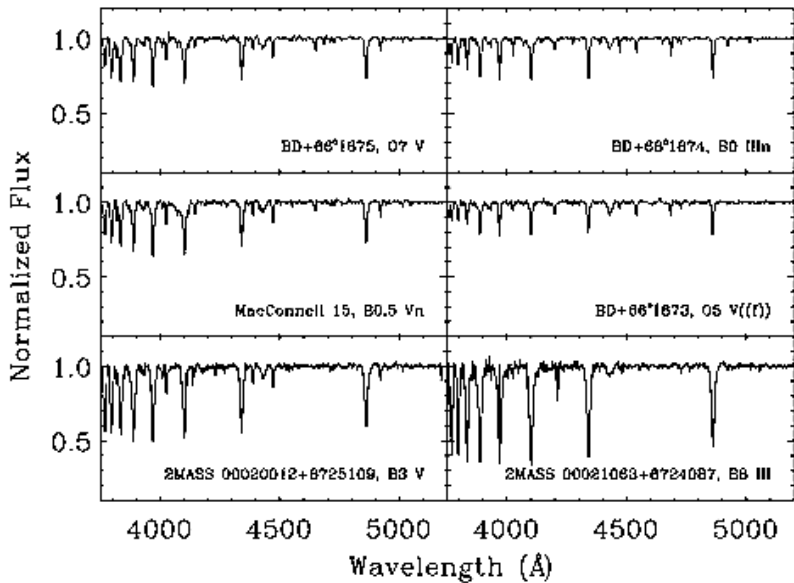
Figure 2. A mosaic of continuum-normalized CCD spectra for likely members of Berkeley 59 and Cep OB4.
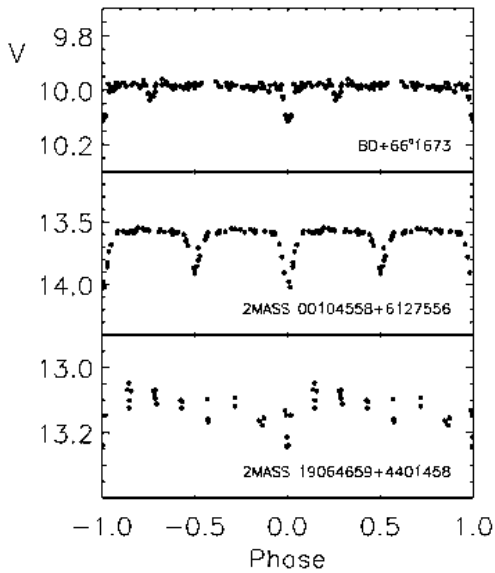
Figure 3. Light curves for the three eclipsing systems BD+66°1673, 2MASS 00104558+6127556, and 2MASS 19064659+4401458.
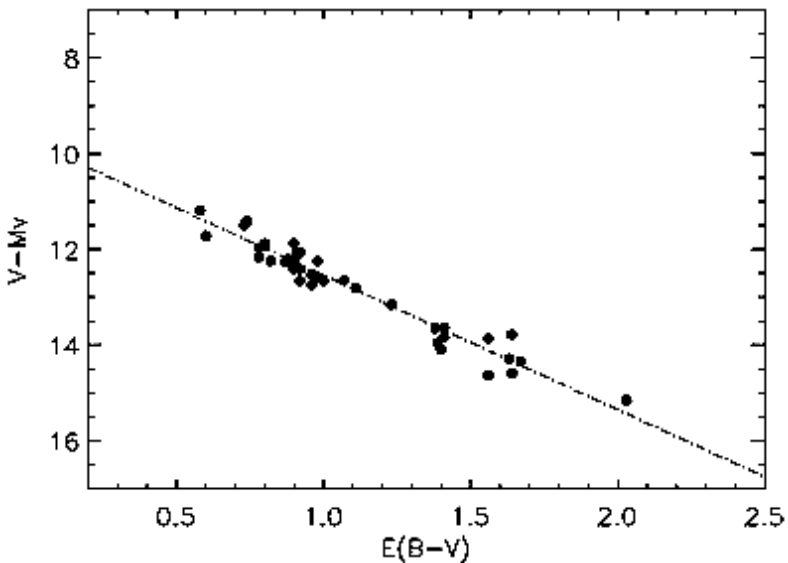
Figure 4. A variable-extinction diagram for likely main-sequence and zero-age main-sequence (ZAMS) members of Berkeley 59 and the Cep OB4 association. Least squares and non-parametric fits yield a ratio of the total to selective extinction of $R_V = 2.81 \pm 0.09$.
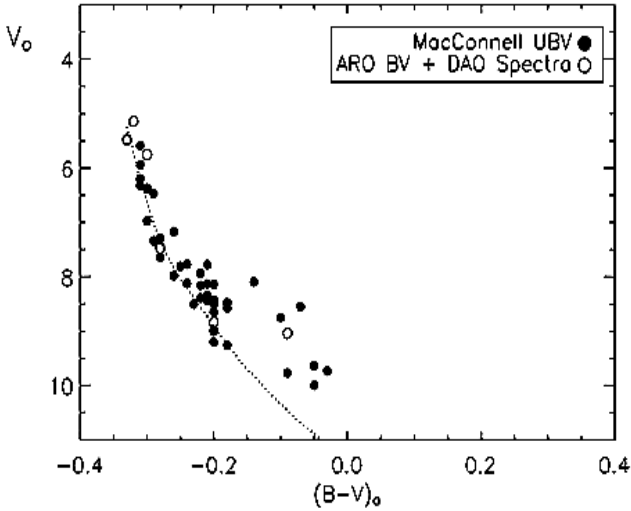
Figure 5. A reddening-free *BV* color-magnitude diagram for Berkeley 59 (open circles) and Cep OB4 (filled circles). A ZAMS fit to the observations yields a distance of d = 883 ±43 pc and a reddening of E_{B-V} = 1.38 ±0.02 in the core of the cluster.
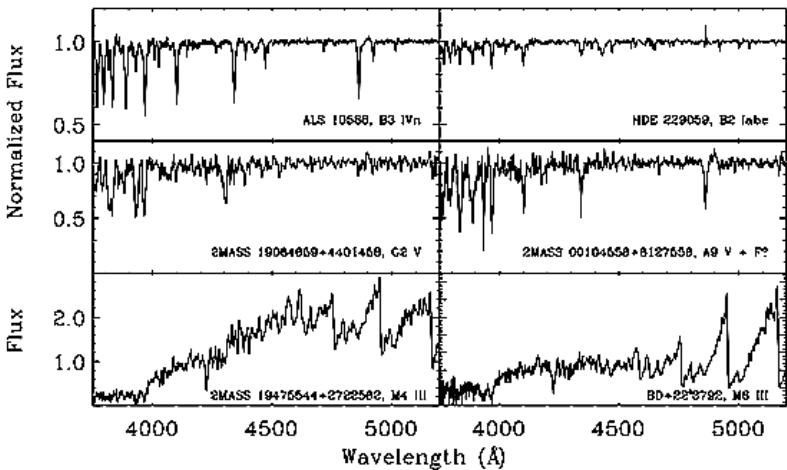
Figure 6. A mosaic of CCD spectra from the DAO 1.8-m Plaskett telescope for variables examined in this study.
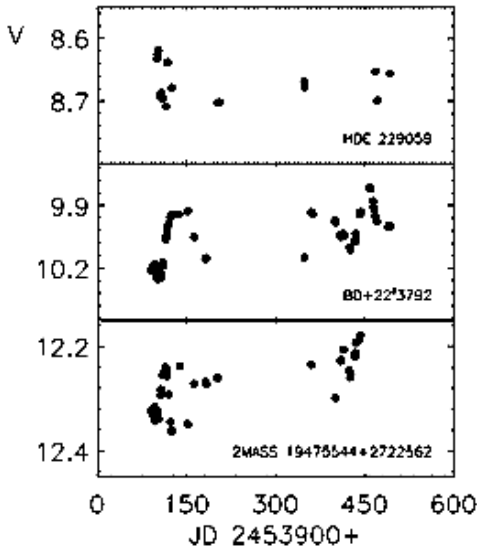
Figure 7. Light curves for variables examined in this study, constructed from differential photometry from the ARO. Zero-point offsets are expected (see text), although the standard deviation of observations for check stars in the same fields ranges from ±0.006 to ±0.008 mag.
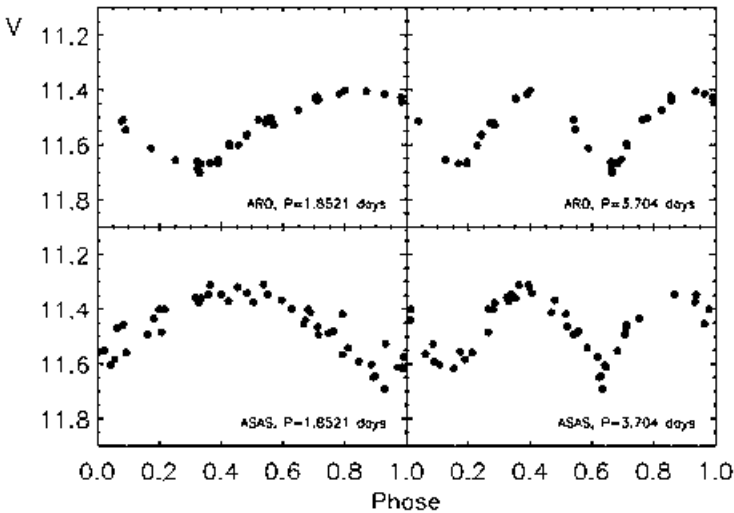
Figure 8. Light curves for ALS 10588 from ARO and ASAS data phased with possible periods of 1.8521 and 3.704 days.
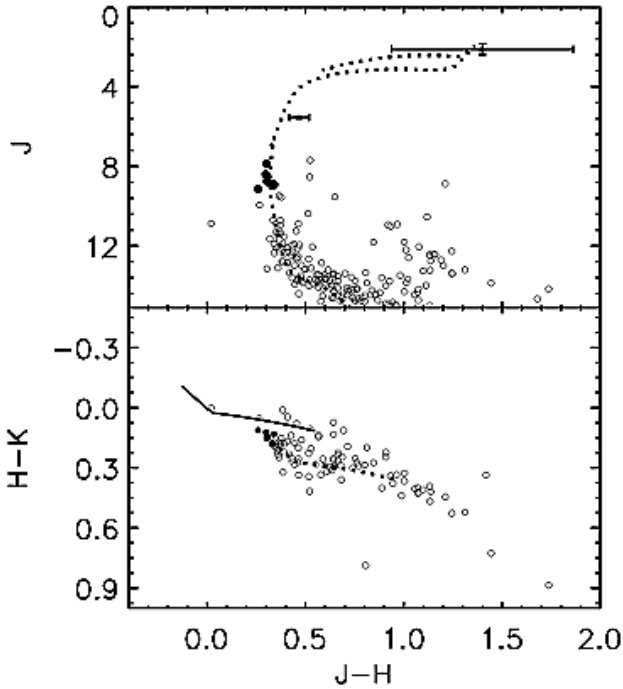
Figure 9. A color-color diagram (lower) and color-magnitude diagram (upper) for Berkeley 87 constructed from 2MASS data. The intrinsic color-color relation for the 2MASS system (Turner unpublished) is depicted as a solid line, as well as reddened by $E_{J-H} = 0.42 \pm 0.04$ ($E_{B-V} \simeq 1.36$) as a dotted line (lower). Filled circles correspond to stars likely to be cluster members. An isochrone fit (upper) is provided to highlight the assumed evolution (see text). The variable stars HDE 229059 ($J = 5.551$) and BC Cyg ($J = 2.117$) are provided with photometric error bars (BC Cyg is near saturation).

Infrared Passbands for Precise Photometry of Variable Stars by Amateur and Professional Astronomers

Eugene F. Milone

Department of Physics and Astronomy, University of Calgary, 2500 University Drive, NW, Calgary, AB T2N 1N4, Canada

Andrew T. Young

Astronomy Department, San Diego State University, PA-210 5500 Campanile Drive, San Diego, CA 92182-1221

Abstract   The infrared (IR) spectral region is a rich one for variable star work, especially of cooler stars, but it is hard to do IR photometry because of high, variable background, and specialized telescopic equipment that is usually required to obtain meaningful data. Typically, telescopes with IR detectors are at high elevations, to minimize water vapor absorption. Nearly all the filters produced for astronomical work at observatories around the world have not been optimized for use at anything other than the highest and driest of observatories. This has made it difficult for amateur astronomers to contribute to this field. Now, however, this is no longer the case. The IAU's Infrared Working Group (IRWG) has designed and tested a set of IR filters less sensitive to water vapor, permitting observations at any site where precise optical photometry can be carried out. Data acquired with these filters can be corrected easily for atmospheric (water vapor) extinction, unlike the situation with the older IR filters. We demonstrate this with data from the University of Calgary's Rothney Astrophysical Observatory.

1. Introduction

Infrared radiation was discovered in the light of the Sun by William Herschel (1738–1822). Herschel (1800) used thermometers to quantify the heat that passed through each of the colors. The highest temperature was found just beyond the reddest color. Despite this promising beginning, it took a while before IR detectors were sufficiently sensitive to permit other objects to be observed. Charles Piazzi Smyth discovered lunar IR radiation in 1856 with a thermocouple at Tenerife. In 1880, Lord Rosse observed the Moon through its phase cycle to determine its temperature.

Bolometers for wavelengths longer than ~2.5 micrometers, and lead sulfide (PbS) detectors with relatively low sensitivity and long time constant in the near IR (~1 to 2.5 micrometers), were used up to the 1960s to observe bright stars and planets. In the 1970s newer detectors became available, and a wider

range of objects could be observed. Currently, InSb and HgCdTe detectors and imaging arrays are widely used for infrared detection. One manufacturer has now produced a relatively inexpensive infrared detector for use by amateur astronomers, which we discuss below. Consequently, infrared photometry can be done by any dedicated observer, if the conditions under which it can be carried out are understood and practiced carefully. We will discuss these shortly. First, however, we consider why one should observe in the IR and what kinds of objects can be observed optimally.

2. Interesting astronomical targets in the infrared

Currently, objects that can be studied include:

- Binary stars
- Eclipsing binaries
- Pulsating stars
- Eruptive stars (novae and SN ejecta)
- Occultations of extrasolar planets
- Interstellar and circumstellar dust
- Earliest galaxies

Because this is not a treatise on the infrared emission characteristics of these objects, for a few cases we give just a brief sketch of why they can be observed usefully in the infrared. Any systematic study of an object should be started only after fully reviewing its properties and potential limitations of photometry to reveal them.

The infrared colors of visible binary components provide important clues to their natures. For the very cool objects known as brown dwarfs, for example, the colors help to identify temperatures and their intrinsic brightnesses indicate ages. Often, IR spectroscopy is called on to refine our knowledge of these and other cool objects.

For eclipsing binaries, the UV is sensitive mainly to blue companions and plage regions, whereas the IR is sensitive to red companions and can help model cool star spots. Broad passbands covering the entire spectral region therefore provide better constraints on the temperatures of both components and high and low temperature regions on both stars than do passbands covering only a small spectral region. Such capability will be essential to study the ground-based light curves and radial velocity curves that will be needed to follow up millions of eclipsing binary discoveries made by existing and planned surveys, such as that from the space-based GAIA mission scheduled to be launched in 2011. Specific examples of the IR advantage can be seen in the *B* and *K* simulated passbands of the Algol system DM Persei, plotted with an earlier version of BINARY MAKER than the currently marketed version, 3.0 (Bradstreet and Steelman 2004) in Figure 1. These data, based on the observed light curves of Hilditch *et al.* (1992) and simulations of Terrell *et al.* (1992), show

the relative depth changes of the primary and secondary eclipses (where the hotter and cooler stars are eclipsed, respectively). In passing, we note that a new solution for this system has just been published by Van Hamme and Wilson (2007), who have a different set of parameters, including the temperatures of both components. They found temperatures of 18,000 and 7816 K (giving a ratio of 2.3 in temperature, and of 28 in surface brightness), corresponding to spectral types B2.5 and A1.5 for stars 1 and 2, respectively. Note that the secondary is not a cool star, but it is far cooler than its companion.

Among pulsating stars, amplitudes of Cepheids depend strongly on temperature variation and so are larger in the ultraviolet (UV); in infrared passbands, on the other hand, the amplitudes are smaller. As the temperature changes during a cycle, the flux increase due to this cause is proportionately less in the infrared, so the IR flux is more sensitive to size variation. Photometry is always welcome, if even over a single cycle and in a limited number of passbands (but two or three are much more helpful than one), if carefully done. Let us say that if one desires to obtain the radius of a regularly pulsating star, one needs to obtain radial velocities around the same time that the optical and IR photometry are carried out. For such details and the reduction and analysis procedures, one can read any of many sources. One close at hand is that of Milone *et al.* (1999); additional references are found therein.

Eruptive objects such as novae and supernovae develop dust shells that are studied optimally in the infrared. Generally, any object with a dust shell can be studied photometrically in the IR to find the shell's composition as well as its temperature.

On the other hand, the dimming of starlight due to the scattering effects of interstellar dust is minimal in the infrared; this fact provides important clues to the intrinsic brightness and reddening at shorter wavelengths.

Thus, there are many potential and interesting infrared targets available for study, and too few astronomers to study them all. Moreover, they can be studied to a greater accuracy and precision than previously, thanks to new filter designs.

3. The challenges of infrared photometry

Infrared photometry is beset by difficulties, but most of these afflict mainly the thermal infrared (beginning at the *K*-band window of the atmosphere, roughly the region between 2 and 3 micrometers, or 20,000 to 30,000 Å). If the temperature of the telescope and observing site is 20° C, the environment is radiating most strongly at ~10 micrometers. Therefore, the telescope and photometer must be configured to minimize the effect of this local radiation. First, the optics must be pristine so that dust and other material on the mirror surfaces do not radiate onto the detector. Next, the optics should be of high quality so that only the intended radiation is focused onto the detector. If the telescope is of a Cassegrain design, for example, such that the primary mirror

has a central hole to pass the radiation to the detector from a secondary mirror suspended above it on the optic axis, it is important that only the desired stellar radiation reach the detector. To accomplish this, the secondary mirror must not reflect into the detector any part of the warm primary mirror cell structure, so a stop must be used in the system if it does, to crop the radiation from outside the edge of the primary mirror itself. If a single-detector photometer is to be used to observe at wavelengths longer than 3.5 micrometers, a bolometer may be used, and this requires liquid helium as a coolant, a cryogen that is cooled to at most a few degrees above absolute zero (–273° C). The cooler the detector, the less thermal noise that it produces, and the greater its sensitivity. Usually the detector is mounted within a double-walled dewar with liquid nitrogen in an external jacket and liquid helium in an inner jacket. The outer jacket keeps the inner container and the detector cool through slow evaporation, a cooling process; it must be refilled periodically. The transfer of liquid helium is, itself, an art and the procedure can be dangerous if mistakes are made. Very warm work gloves must be used to handle transfer lines and dewars because of the extreme cold. Water vapor may freeze in the narrow neck of the dewar, blocking evaporation of the helium, and as the liquid helium warms up it will evaporate well before the water, nitrogen, and oxygen ices sublime, potentially resulting in a catastrophic explosion.

Even when the optics are pristine, and all transfer tasks are handled properly, the photometry must be done with great care for the results to be meaningful. For example, the bright warm sky background surrounding the star image must be subtracted from the stellar observation, so, even in this day of multi-detector arrays, the secondary mirror must be "chopped" (made to oscillate at some frequency between 10 and 50 Hz, typically), so that a star-free field can be subtracted from the field containing the star and the difference co-added to create a star-only image. Because the chopping is done to one side of the star, a further precaution is to "nod" the telescope (move the entire telescope) by a distance equal to the chop amplitude, so that the starless and star-containing apertures are both 180° different in phase, and the sky that is sampled is on the other side of the star along the chopping line. This periodic nodding, done at a much lower frequency than the chopping, averages and smooths-out variations of background infrared sources across the region of the target. It helps to be able to change the orientation of the chopping and nodding line so that hot spots on the sky can be avoided altogether. In this way, the constantly varying sky background can be subtracted as quickly as possible and asymmetries in the background near the target can be minimized. When an extended object such as a star cluster, or a nebula, rather than a single star, is to be observed, the precautions must be similar. Typically, the secondary mirror is under-sized in the sense that when the secondary is tilted it still does not pick up radiation from beyond the edge of the primary mirror.

In all circumstances, the filters to be used must also be as free as possible from radiation from the atmosphere; they should not, for example, include

water-vapor emission. Yet, this is commonly the case with the previous, and almost all of the present, generation of infrared filters.

For the so-called "non-thermal" infrared, at wavelengths shorter than about 2.5 microns, the observing situation is less formidable, because the telescope and environment are not radiating strongly at wavelengths near the radiation to be measured, but nevertheless can be daunting. In this spectral region, the preferred coolant has been liquid nitrogen, typically, and both the inner and outer jackets are filled with this cryogen, which is certainly easier to handle than liquid helium, but of course still hazardous because of its extreme cold (~77 K or –196° C, or less). Infrared arrays do not require the chopping and nodding that is done in the thermal IR, but they do require flat-fielding, dark current, and bias treatment as for CCDs, with the added requirement that several images be "dithered" (images taken of fields differing by a few arc-seconds or more in position) and then median-combined so that a star-less image of the background can be obtained and removed from the target field. Of course, if the detector is not an array but a single detector of InSb, HgCdTe, or other substrate, the same nodding and chopping techniques as for bolometers must be used.

The infrared dewar and lock-in amplifier for single-channel photometry at the Rothney Astrophysical Observatory at the University of Calgary can be seen in Figures 2a and 2b, respectively. Cryogenic dewars such as that of Figure 2a (manufactured by Infrared Labs in Tucson) are expensive, but contain all the necessary optics for detection. In this case, it contains a single detector cooled to liquid nitrogen temperatures. The lock-in amplifier obtains a signal that is modulated at the chopping frequency of the secondary mirror (hence the "lock-in"); the signal is then rectified and integrated for a specified interval.

Even for the near IR, the telescope optics must be clean, and sources of stray light and heat minimized. The availability of a thermoelectrically cooled IR-sensitive photodiode is an important new development and deserves special attention, because LN2 dewars and the detectors within them are very expensive, even if only the *z, J,* and *H* windows can be explored (the windows are described and discussed in the next section). Henden (2002) suggests how amateur astronomers can make use of such a photometer (an Optec, Inc. SSP-4 photometer with an InGaAs PIN photodiode detector), and we echo his suggestions for careful observational procedures with this non-chopping system; we recommend, however, a change of filters for use with this photometer.

Even within these two atmospheric windows, the filters that are available have not been optimized for most observing sites to pass the extra-atmosphere radiation and exclude that from the atmosphere alone. The best of these non-optimal filters, the "Mauna Kea" set, was not produced after extensive optimization experiments in both placement and width within the windows but apparently selected to merely butt up against the atmospheric windows as modeled for the Mauna Kea Observatory, one of the highest and driest

sites in the world. At less favorable sites, the atmospheric windows are narrower and the passbands will be defined by the edges of the atmospheric windows (discussed in the next section). This is not the way to achieve the best photometry! Consequently, it is not surprising that our tests have shown (Milone and Young 2005; 2007) that even at Mauna Kea itself, the Mauna Kea set do not appear to be optimal, generally, and those filters are, at best, only nominally useful at intermediate elevation sites (~2 km) such as Kitt Peak and Cerro Tololo, primarily because of the variability of the water vapor content of the atmosphere; moreover, our tests indicate that they are inadequate for the lower altitude sites (~1 km and lower) at which most university and amateur observatories are located. Therefore, we strongly advise astronomers, both amateur and professional, to seek the most suitable passbands with which to carry out their infrared photometry.

It is precisely the optimization of filters that we now wish to discuss so that optimal infrared photometry can be carried out by all astronomers, whatever their astronomical targets.

4. The IRWG passbands and how they improve infrared photometry

Figure 3 shows the simulated transmission of the Earth's atmosphere for a standard model atmosphere normalized to 1 and computed for an observatory site at 2.1 km elevation, typical of large multi-user observatories such as the Kitt Peak National Observatory near Tucson, Arizona. The lower abscissa scale is in wavenumbers, with equivalent micrometers on the upper scale. The spectral windows of the atmosphere, where some light is transmitted, are indicated by the designations z (for the 1 micron region), *J, H, K, L, M,* and *N* (for the 10 micron region). Except for "*z*" and "*H*," these are the designations of the original Johnson (1965; 1966) passbands which, however, were not optimally placed within these windows, and hence, provided relatively poor photometry because the boundaries and even transmission within the windows varies strongly with water vapor content of the atmosphere. Although the filters have been manufactured many times with differing central wavelengths and spectral widths, they have been designated usually the same way, according to which window they were mainly designed to cover. Consequently, it seems reasonable to refer to these "windows" with those designations.

In the late 1980s a joint commission meeting on infrared photometry was held at the General Assembly of the International Astronomical Union held in Baltimore, Maryland. The meeting explored the reasons for the problems of lack of reproducibility in infrared data and an overall limitation of about 3% in precision (from comparisons of near-infrared photometry from different observatory sites and even at the same site at different instants. See Milone (1989)). The result was the creation of an infrared working group (IRWG) of Commission 25 (Photometry and Polarimetry) which, among other tasks, was to redesign the broadband infrared photometry system by placing and shaping

a new set of passbands within the atmospheric windows optimally. This it has done (Young *et al.* 1994; Milone and Young 2005, 2007). We now call the passbands corresponding to these filters *iz, iJ, iH, iK, iL, iL'* (in a slightly longer wavelength part of the *L* window), *iM, iN, in* (for a narrower passband in a branch of the *N* window), and *iQ*, where the "*i*" indicates "improved."

However, most amateur astronomers will most likely work in the near-infrared, where a commercial photometer, Optec, Inc., SSP-4, with a Hamamatsu photodiode is available. Therefore, we will confine our comments to the non-thermal region, which includes the *z, J,* and *H* windows. The references given above can be consulted for the improved passbands in the other windows.

A comparison of a measure of the signal to noise ratio and the atmospheric (water vapor) extinction coefficient for all of the IRWG improved filters has been made for all existing passbands and these have been compared to the IRWG simulated and manufactured filter sets. We show annotated plots of these relations in Figures 4 and 5 for the *z* and *J* windows and for the *H* window, respectively, for a particular atmospheric model atmosphere. The passbands with the highest signal-to-noise and lowest atmospheric extinction characteristics lay in the upper left parts of these diagrams. For further discussion of our S/N statistic, see Milone and Young (2005). In Figure 4, the designations "*sj*" is for a Mauna Kea filter, and "*sJn*" is a very narrow filter in a clean part of the window devised for calibration purposes. In Figure 5, Note that the Mauna Kea filter "*sh*" lies very close to the older RAO "*H*" filter, designated "*rH*."

One of the problems with conventional filter photometry in the IR is that water vapor causes great amounts of light to be absorbed from the light contained within those filters in the beam from the star to the telescope. This causes a curvature in the extinction curve between 0 and 1 air mass (0 air mass is that at the top of the atmosphere; an air mass of 1 is the path of light impinging vertically on the observer at the observing site; 2 air masses is the path length for a zenith angle of 60°, and 3 air masses is that at an angle of about 75°). This curvature is known as the "Forbes effect" (Forbes 1842) and is not easily measurable from the ground (where we cannot see to air masses less than 1). Hence, the loss due to water vapor absorption in the atmosphere is not known precisely, but it *is* variable at all time scales! The IRWG passbands minimize the extinction and the Forbes effect; even the extinction between 1 and 3 air masses is lessened. This is the reason these passbands are improved. At the highest and driest sites, they will likely pass less infrared flux than will older filters, but, as we have argued, the tradeoff is better signal-to-noise and more reproducible results, from hour to hour, and day to day, and site to site! This is the answer to the 3% problem (a typical upper limit of agreement among different data sets) that has plagued previous generations of IR passband photometry. For more readily accessible details about the Forbes effect, consult Young *et al.* (1994). A summary is also provided in Milone and Young (2005). Details of the atmospheric modeling software, MODTRAN, can be found in Berk *et al.* (1989).

The extinction curves between 1 and 3 air masses for the *iz, iJ, iH,* and *iK* passbands for two standard stars can be seen in Figures 6 and 7. The extinction data in Figure 7 were obtained on the same date as the data obtained in older *JHK* passbands *rJ, rH, rK,* shown in Figure 8. The current practice in the literature is to place primes on the *JHK* designations to indicate narrower passbands which may or may not be repositioned within the windows so one occasionally sees a *K'* passband mentioned in the literature. In any case, none of these and none of the "*r*" filters have been optimized to the same extent as the IRWG passbands. Therefore it is not surprising that we see much larger extinction between 1 and 3 air masses with the *rJ, rH,* and *rK* filters than with the IRWG near-infrared set. What is not shown here is simulated behavior of these filters between 0 and 1 air mass. In fact, there is a strong Forbes effect (strongly curved extinction between 0 and 1 air mass) for these older passbands, and a near absence of a Forbes effect for the IRWG passbands (many simulations can be seen in Young *et al.* 1994; Milone and Young 2005, 2007). This means that the true extinction and therefore the true outside-atmosphere magnitudes are not revealed by a linear extrapolation to zero air mass in the extinction curves of the older filters. The extinction lines for the IRWG passbands, on the other hand, do permit outside-the-atmosphere magnitude determination with a linear extinction approximation. Simulations reveal that in the *iz* and *iH* passbands, there is effectively no curvature in the extinction line for a mid-summer, mid-latitude model at the elevation of the RAO (1.27 km), and even in the *iJ* and *iK* passbands it is small enough to result in only a small offset from a direct linear extrapolation to zero air mass. Note that Figures 4 and 5 indicate that infrared passbands that produce lower extinction curves tend to be those with higher signal-to-noise characteristics. It therefore follows that because the manufactured IRWG filters approximate the designed passbands well-enough that data obtained with them have lower extinction, they also have higher signal-to-noise characteristics.

5. A note about nomenclature of the *iz* passband

There is a need to keep nomenclature as precise and meaningful as possible, so we make the following comment about the passband notation we have been using since the early 1990s.

The proliferation of photometric systems has made any unambiguous nomenclature of passbands impossible. For example, the "*z*" window has been given a variety of names, and the letters *z* and *Z* have been applied to a variety of different wavelengths. Although wide passbands near 1 micron wavelength go back to the six-color photometry of Stebbins and Whitford in the 1940s, the first use of a narrow passband in this window seems to have been by Walker (1969), who denoted the passband by *W*; he also used a passband called *Z*, but its effective wavelength was 2.2 microns. The first association of the letter *Z* with the 1-micron passband was made by asteroid photometrists in the late

1970s (see Gradie *et al.* 1978; and Tedesco *et al.* 1982), who used the letter *Z* for it. However, the Vilnius system introduced in the 1960s already used a *Z* band near 516 nm, and many other workers have used something similar, sometimes denoted by *z* instead of *Z*. Shortly after the asteroidal *Z* band was introduced, Schneider *et al.* (1983) introduced a broad band they called *z*, extending from about 840 nm to beyond 1 micron but truncated on the IR side by the rapidly decreasing sensitivity of the detector they used; unfortunately, it is badly mutilated by the water-vapor absorptions just longward of its centroid wavelength. Passbands descended from this so-called "Gunn *griz*" system have continued to be used since then in galaxy photometry. On the other hand, Hillenbrand *et al.* (2002) used a narrow passband at 1.035 microns that resembles our *iz* band, but named their band *Y*, in conflict with the *Y* passband of the Vilnius system in use for some forty years. Clearly this is an issue that needs to be considered by Commission 25 of the IAU in the first instance.

6. How to obtain the filters

As we have intimated, infrared astronomers have tended to tinker with the original Johnson passbands instead of abandoning them, even though the precision and accuracy of transformations of data obtained with those filters and their improved but still not optimal passbands is sharply limited. This practice continues to the present due to both economic and perhaps sociological reasons which have little to do with the best scientific practice. Nevertheless, hope springs eternal, so we are making knowledge of the availability of an optimized set of filters to a wider body of interested observers, in the hope that the new system will be sought by many, a circumstance that, we are assured, will bring down the cost of the filters, which are prohibitively expensive when produced in small batches. The sole supplier of the IRWG filters to date has been Custom Scientific of Phoenix, Arizona, but the costs of manufacturing these filters has increased greatly over the past decade. Apparently the only way to do this economically at present is to amass a large number of orders for a batch run. Therefore, all interested parties should encourage filter manufacturers to make, and photometer manufacturers to market with their photometers, the IRWG set.

We now describe some of the specifications for the near IRWG filter set. The filter spectral profiles are triangular, but experience has shown that if these have a flat spectral region at peak transmission so that the profile is in the form of a trapezoid, this does not hurt the reproducibility very much, and for some passbands, can even improve them. In Table 1, we give the central wavelength, the width at 80% relative transmission, and half-power full widths, in Ångströms (divide by 10,000 for micro-meters). We also include here the *iK* passband, for astronomers who have access to detectors sensitive to longer wavelengths.

These are the specifications for the passbands at the operating temperature of the filters and detector. For good photometric practice, the transmission

outside of these limits should be strongly blocked, to better than about one part in a million. It is always a good idea to obtain transmission traces of the filters once they are obtained to check on the transmission both within and outside the specified passband.

For further details on the background and method of experimentation that led to these passbands, see the previously mentioned references, especially Young *et al.* (1994).

7. Conclusions

We have discussed some of the programs to which infrared photometry can contribute as well as some of the problems with infrared photometry as currently practiced and the solutions to them; in particular, we demonstrate the advantages of an optimally designed set of infrared filters to permit improved photometric precision and accuracy. We urge astronomers who have not yet attempted infrared astronomy because of past limitations to approach the manufacturers of photometers and filters to ask for the IRWG set of filters with which improved IR photometry can be carried out. In this way, and perhaps only in this way, given sufficient care in both observational techniques and reduction and analyses, can substantial progress in IR photometry be achieved, and with it, improved accuracy and precision in all appropriate infrared investigations (i.e., ground-based, broad-band) in which these passbands are used. This is No. 75 in the *Publications of the RAO* series.

References

Berk, A., Bernstein, L. S., and Robertson, D. C. 1989, MODTRAN: *A Moderate Resolution Model for* LOWTRAN *7,* (GL-TR-89-0122), Air Force Geophysics Laboratory, Bedford, MA.

Bradstreet, D. H., and Steelman, D. P. 2004, BINARY MAKER *3.0*, Contact Software, Norristown, PA.

Forbes, J. D. 1842, *Philos. Trans. Roy. Soc. London*, **132**, 225.

Gradie, J., Tedesco, E., and Zellner, B. 1978, *Bull. Amer. Astron. Soc.*, **10**, 595.

Henden, A. A. 2002, *J. Amer. Assoc. Var. Star Obs.*, **31**, 11.

Herschel, W. 1800, *Philos. Trans. Roy. Soc. London*, **90**, 255.

Hilditch, R. W., Skillen, I., Carr, D. M., and Aikman, G. C. I. 1992, *Mon. Not. Roy. Astron. Soc.*, **222**, 167.

Hillenbrand, L. A., Foster, J. B., Persson, S. E., and Matthews, K. 2002, *Publ. Astron. Soc. Pacific*, **114**, 708.

Johnson, H. L. 1965, *Astrophys. J.*, **141**, 923.

Johnson, H. L. 1966, *Ann. Rev. Astron. Astrophys.*, **4**, 193.

Milone, E. F., ed. 1989, *Infrared Extinction and Standardization,* Lecture Notes in Physics, Vol. 341, Springer-Verlag, Berlin.

Milone, E. F., and Young, A. T. 2005, *Publ. Astron. Soc. Pacific*, **117**, 485.

Milone, E. F., and Young, A. T., 2007, in *The Future of Photometric Spectrophotometric and Polarimetric Standardization,* ASP Conference Series, Vol. 364, C. Sterken, ed., Astron. Soc. Pacific, San Francisco, 387.

Milone, E. F., Wilson, W. J. F., and Volk, K. 1999, *Astron. J.*, **118**, 3016.

Schneider, D. P., Gunn, J. E., and Hoessel, J. G. 1983, *Astrophys. J.*, **264**, 337.

Tedesco, E. F., Tholen, D. J., and Zellner, B. 1982, *Astron. J.*, **87**, 1585.

Terrell, D., Mukherjee, J., and Wilson, R. E. 1992, *Binary Stars: A Pictorial Atlas*, Krieger Publ. Co., Melbourne, FL.

Van Hamme, W., and Wilson, R. E. 2007, *Astrophys. J.*, **661**, 1129.

Walker, R. G. 1969, *Philos. Trans. Roy. Soc. London, Ser. A*, **264**, 209.

Young, A. T., Milone, E. F., and Stagg, C. R. 1994, *Astron. Astrophys., Suppl. Ser.*, **105**, 259.

Table 1. IRWG Near IR Passbands.

Passband	*Central Wavelength*	*FW 80% Transmission*	*HPFW*
iz	10,320 Å	310 Å	730 Å
iJ	12,400	290	790
iH	16,280	870	1,520
iK	21,960	990	1,880
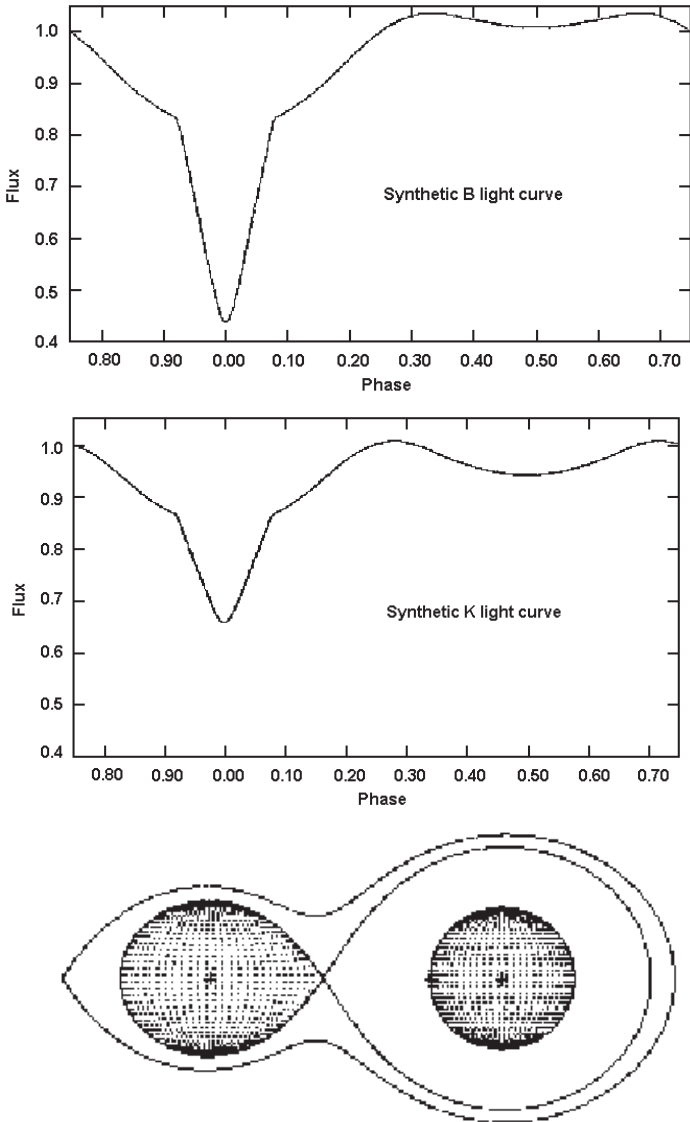
Figure 1. Top. A simulated B light curve for the Algol eclipsing binary DM Persei, from the elements of Hilditch *et al.* (1992), produced with Binary Maker software (Bradstreet and Steelman 2004), as were the lower panels. Middle. A simulated *K* light curve for DM Persei. Bottom. A Lagrangian surface plot for the semi-detached eclipsing system DM Persei, again from the elements of Hilditch *et al.* (1992). For a later model that incorporates third light from a third component, see Van Hamme and Wilson (2007).
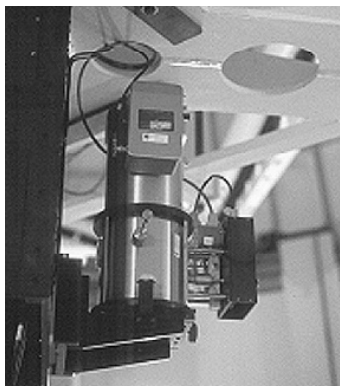
Figure 2a. An infrared dewar, with filters enclosed and kept at cryogenic temperatures, attached to a side port of the Cassegrain focus of the Rothney Astrophysical Observatory's 1.8-m Alexander R. Cross Telescope (ARCT). The light was conveyed from the telescope optics through a right-angle front-silvered diagonal mirror. Such a double dewar is used conventionally to keep the noise of the detector to a minimum.
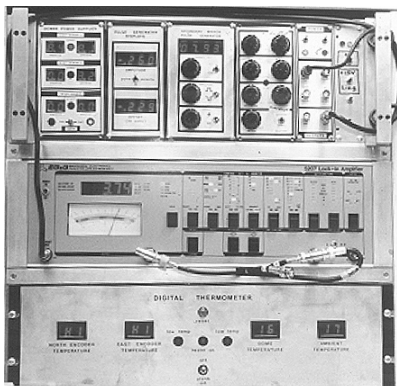
Figure 2b. A bank of electronics in the control room of the ARCT that controls the chopping of the secondary mirror (top panel) and detection of infrared radiation synchronized to it, through a Lock-in Amplifier (middle panel). The lowest panel displays temperatures at this alt-alt telescope's motor-encoders.
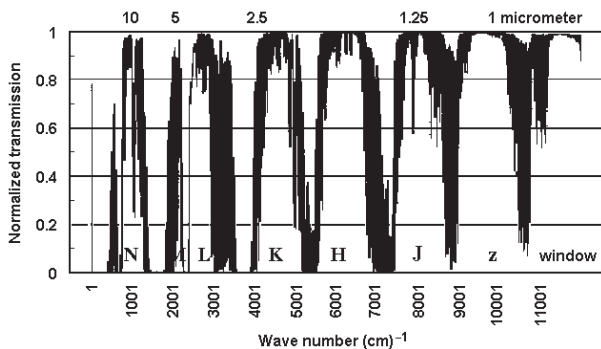
Figure 3. Infrared atmospheric transmission computed for a U.S. Standard Atmosphere model for a site at 2.1 km elevation, appropriate for such sites as the Kitt Peak National Observatory in Arizona. The wavelength in micro-meters corresponding to some of the wavenumbers on the abscissa is indicated and the atmospheric "windows" where the transmission is highest, are marked with letters. These should not be confused with passband or filter names, which often have the same designations, but often are not confined to the individual windows.
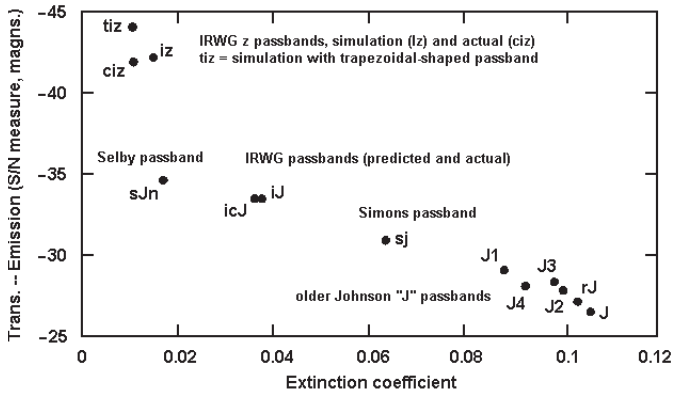
Figure 4. A plot of quality of a number of passbands for use in the *z* and *J* windows, in current use by astronomers, in the form of a computation of a measure of the signal-to-noise vs. the computed extinction coefficient. The original Johnson passband is marked with a "J" and others similar to it, have a numbered suffix, except for "rJ," which is an older passband used at the RAO. The "Simons passband" indicates the Mauna Kea passband as sent to us for testing by D. Simons in 1997. The *iJ* and *icJ* passbands indicate the IRWG passband as designed and manufactured, respectively. The *z*-window passbands of the IRWG set are similarly marked. The *tiz* designation is for a flat-topped, trapezoidally shaped passband instead of the triangular shaped for all the other IRWG passbands. The highest signal-to-noise values are at the top of the diagram. Note that there is a tendency for the passbands with the highest signal-to-noise ratio to be associated with the smallest extinction coefficients. This alone shows that the newer passbands are less sensitive to atmospheric extinction.
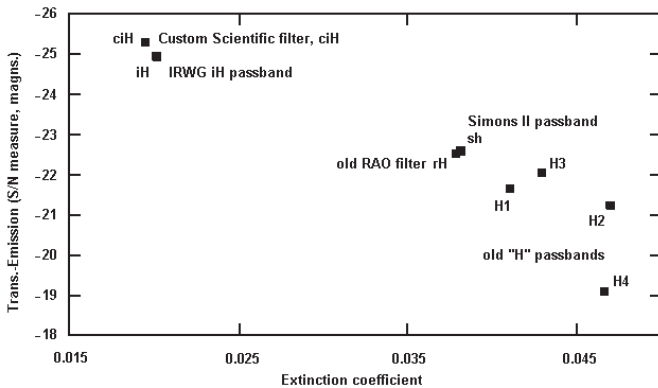
Figure 5. A quality plot for a number of passbands used for photometry in the *H* window of the atmosphere. The passbands are denoted as for Figure 4. Again, the IRWG passbands show the highest signal-to-noise ratio and the lowest atmospheric extinction. The model atmosphere used for the tests that produced the results of Figures 4 and 5 is for a summer, mid-latitude site at 1 km elevation.
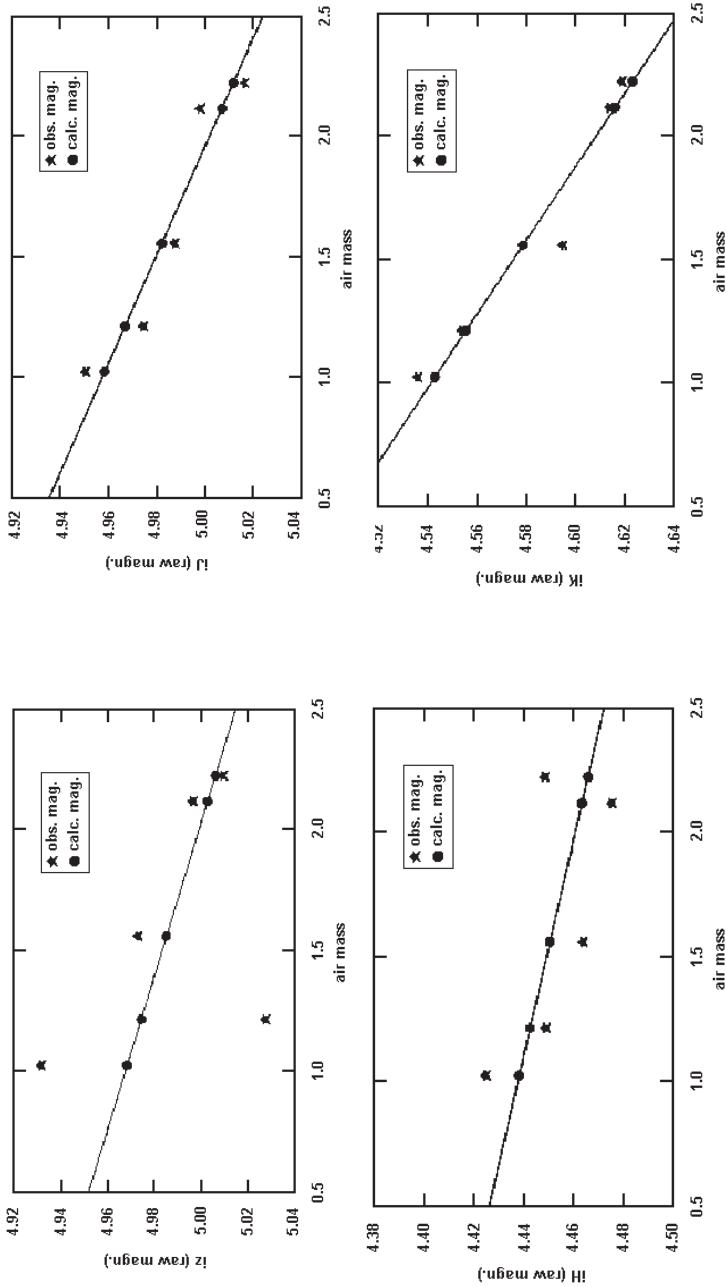
Figure 6. Observed extinction plots for the night of July 13, 2000, for the IRWG passbands, made on the RAO's 1.8-m ARCT. Linear fitting to the data may be extrapolated to give a close approximation to outside-the-atmosphere magnitudes. The extinction star was χ Herculis; k' = ~0.03, 0.04, 0.02, and 0.03 magn./airmass for *iz, iJ, iH,* and *iK,* respectively.
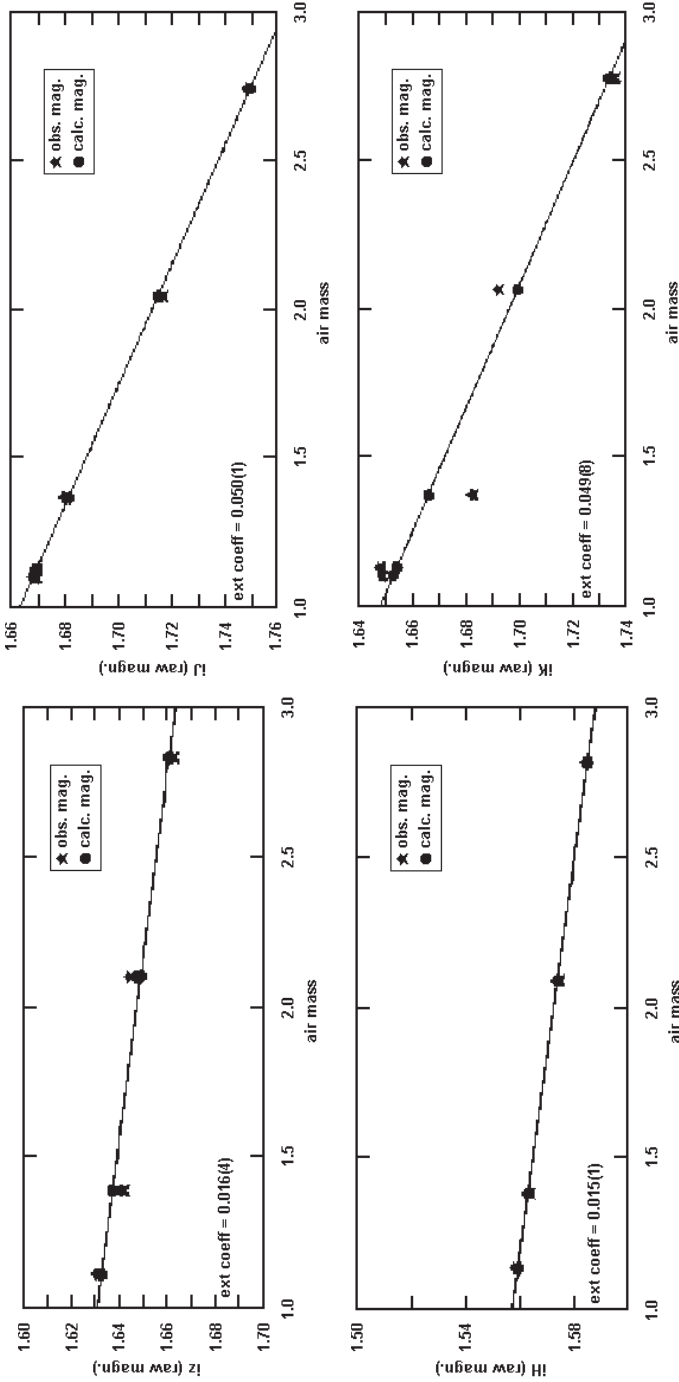
Figure 7. Observed extinction plots for the night of Sept. 26, 2000, for the IRWG passbands, made on the RAO's 1.8-m ARCT. Linear fitting to the data may be extrapolated to give a close approximation to outside-the-atmosphere magnitudes. The extinction star was Vega. The derived linear extinction coefficients and their uncertainties, in units of the last decimal place (in parentheses) are given in the lower left corners of the plots, viz., about 0.02, 0.05, 0.02, and 0.05 magn./airmass for the *iz*, *iJ*, *iH*, and *iK* passbands, respectively.
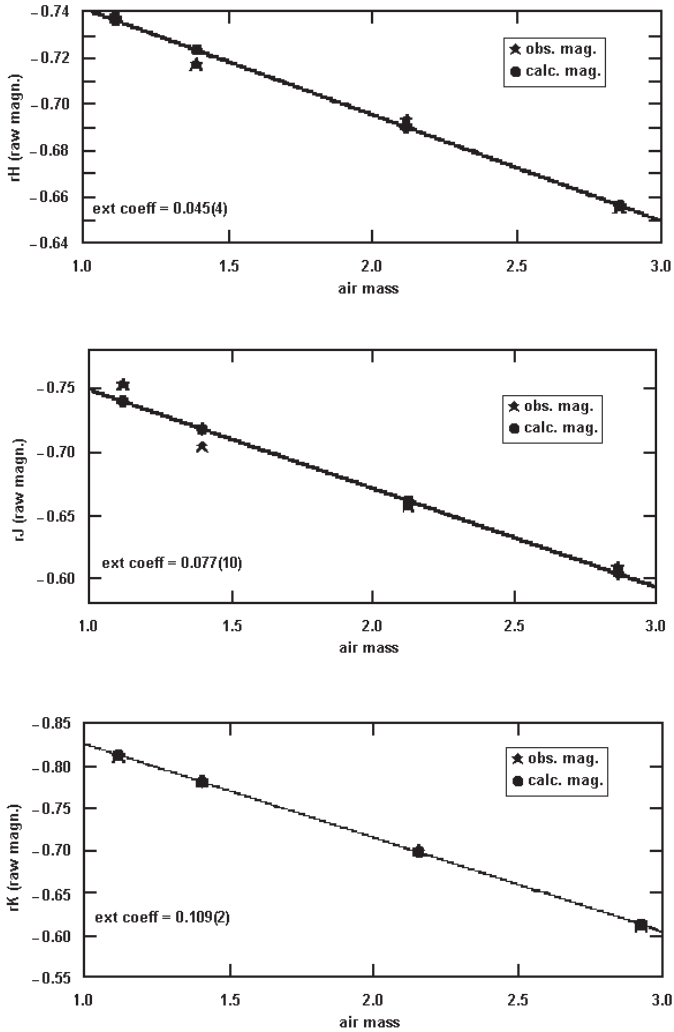
Figure 8. Observed extinction plots for the same night in which the IRWG passbands were used, and for the same extinction star, Vega, but obtained with an older set of passbands. The derived linear extinction coefficients and their uncertainties are again indicated. Note that they are systematically higher than for the IRWG passbands, about 0.05, 0.08, and 0.11 magn./airmass for the *rH, rJ,* and *rK* passbands, respectively.

Adventures in *J*- and *H*-Band Photometry of Evolved Stars

Aaron J. Bradley
Robert E. Stencel
University of Denver, Department of Physics and Astronomy, Denver, CO 80208

Abstract   Among the classes of objects optimized for angular diameter measurements by current generation astronomical interferometers are nearby red giant stars. Precision diameters can help constrain atmospheric and evolution models thereof, but many of these stars are intrinsically variable and thus must be monitored during intervals when interferometry is planned. Using an Optec SSP-4 photometer, we obtained the *J*- and *H*-band magnitudes of a sample of such stars being studied by the Palomar Testbed Interferometer, and report results here.

1. Introduction

Van Belle and Hart (2007) have proposed measuring the angular diameters of a selection of evolved stars and unresolved comparators using the Palomar Testbed Interferometer (PTI, Colavita *et al.* 1999). In order to realize milli-arcsecond angular accuracy, the brightness of each star at or near the time of PTI observation needs to be monitored, ideally in or near the 2.2 micron *K*-band wavelengths used by PTI. Our photometric targets were selected on the basis of priority for PTI observation and accessibility during summer 2007. The comparison stars reported here serve as unresolved point sources for PTI to use to calibrate angular diameters of the target stars.

2. Procedure

Our instrumentation involved the south 0.72-m telescope of the University of Denver's Meyer-Womble Observatory atop Mt. Evans (Stencel 1999), as well as an Optec (http://www.optecinc.com) SSP-4 photometer (Optec 2007; Henden 2002). The data collection was performed in a differential manner following a method described by Hopkins (2006). This method requires determining the brightness of the PTI Target stars and PTI Calibrator Stars, as well as Near-IR Primary Standard Stars (Standard Stars), in both the near infrared 1.2-micron *J*-band and the 1.6-micron *H*-band.

The instrumental magnitude in both the *J*- and *H*-bands is determined for a Standard Star, by star minus sky subtraction, and $-2.5 \log$ (net counts). The Standard Star has a known magnitude in the two bands, from catalog sources discussed below. Next, the instrumental magnitude of a PTI Target star and/or

a PTI calibrator star is determined in both the *J*- and *H*-bands. Finally, the instrumental magnitude of the Standard Star is re-observed. This provides a bracketing of the PTI Target or PTI calibrator with known Standard Stars. This method can also be adapted to include multiple PTI Targets and PTI Calibrator Stars between Standard Stars.

Table 2 shows the measurements for the Standard Stars. First, a correction factor was found from all of the Standard Stars observed on a given night. This correction factor was used to convert instrumental magnitudes to the known, catalog values. One problem with this approach is that the night sky conditions change, both spatially and temporally. Because we are using a differential method, these changes have a large impact on our data analysis. Therefore, we modified this approach to bracket the PTI Target stars and PTI Calibrator Stars between Standard Stars in right ascension, declination, and time, which yielded the results reported below. By doing so, we could minimize the changes in the atmosphere, thereby achieving more reliable results.

One area of interest was the effect of air mass on the observed counts of Standard Stars. Air mass refers to the line of sight column of air that varies with angle from zenith. Most magnitude measurements were taken as close to the meridian as possible, at air mass values between 1.00 and 1.15. Henden (2002) suggests typical extinction values of 0.10 magnitude per unit airmass in the *J*-band, and 0.06 magnitude per unit airmass in the *H* -band. One would expect airmass correction of less than 0.01 magnitude over the majority of our observed range of airmasses, which is less than our quoted errors (see below). Therefore, no air mass corrections have been applied to the results from the data analysis. As a check, a few large airmass readings were made and the extinction found to be consistent with Henden (2002).

Dark counts are used as an offset and are recorded when there is no light incident on the detector. According to Optec, the electrometer amplifier may drift slightly, and if the offset drops below zero, the unit will not display any value for the counts. Thus a positive dark count is necessary (Optec 2007). In general, we found that the dark count tends to decrease as the night goes on, consistent with the cooling of the detector. The dark counts decrease ~5% in the first few minutes of the detector being on, and then slowly recover on a scale of hours. For this reason, we did not take data during the first 15–30 minutes. Because the dark counts are small relative to the counts from the stars, there has been no correction made for the drift.

Any cloud cover or atmospheric disturbance will affect the readings on the SSP-4. It has been found that visible cloud cover will decrease the counts of a star from what would have been seen without the clouds. Light leak has also been a possible source of error in the SSP-4—either having a light shining directly on the SSP-4 casing, or not moving a bright star sufficiently far out of the field of view when taking a sky reading. Additionally, the gain setting on the photometer might not provide a perfectly linear multiplication of the signal.

When going from a gain of 10 to a gain of 100 for the same target, the counts increase more than 10 times, which is less than a 1% effect. The high amplification is the root cause of the nonlinearity in the gain setting (Hopkins 2007).

3. Results

The list of stars that were observed is found in Table 1. Standard Star instrumental and catalog magnitudes are found in Table 2, while the observed magnitudes for the PTI Target and PTI Calibrator Stars are in Table 3. In Table 1, the columns reflect the category of star reported, HD number and spectral type from SIMBAD (Centre de Données astronomiques de Strasbourg 2007), catalog value for *J*- and *H*-magnitudes from Henden (2002), or 2MASS (Skrutskie 1999). The columns in Tables 2 and 3 include star identifier, Reduced Julian Day observed (RJD is JD – 2,450,000), air mass at time of observation, instrumental magnitudes in the *J*- and *H*-Bands, and the conversion factor to calculate the catalog magnitude in both the *J*- and *H*-Bands. Table 3 also includes two columns that contain the calculated catalog values for the PTI Targets and the PTI Calibrator Stars.

It is important to note that Henden claims approximately 0.050 magnitude all-sky accuracy is possible using these Standard Stars. Since we are working in a very limited air mass region, we have assumed an accuracy of 0.025 magnitude on all catalog values for the magnitudes of the Standard Stars used (Henden 2002).

During 2007 July, the 0.72-m mirrors in both tubes of the Meyer Womble Binocular Telescope were resilvered. The mirrors were removed from the telescope on RJD 4293, and were back in service by RJD 4335. Because we used a differential procedure, the subsequent change in instrumental magnitude due to the resilvered mirrors was accounted for by the change in correction factor, as can be seen, for example, with HD 172167 in Table 2.

This particular observational sample does not feature any large amplitude variables, and that is consistent with the measurements and the errors derived here. These measurements provide a baseline against which parallel interferometric observations can be calibrated. In this paper we have demonstrated the utility of the SSP-4 photometer in support of this and other ground based astronomical measurements.

4. Acknowledgements

This publication makes use of data products from the AAVSO International Database contributed by observers worldwide, and the Two Micron All Sky Survey, which is a joint project of the University of Massachusetts and the Infrared Processing and Analysis Center/California Institute of Technology, funded by the National Aeronautics and Space Administration and the National Science Foundation. This research also has made use of the SIMBAD database, operated at CDS, Strasbourg, France.

References

Centre de Données astronomiques de Strasbourg 2007, SIMBAD Astronomical Database, http://simbad.u-strasbg.fr/simbad/

Colavita, M. M., *et al.* 1999, *Astron. J.,* **510**, 505.

Henden, A. A. 2002, *J. Amer. Assoc. Var. Star Obs.*, **31**, 11.

Hopkins, J. L. 2006, private communication.

Hopkins, J. L. 2007, private communication.

Optec Inc. 2007, *Model SSP-4 Solid State Photometer Technical Manual for Theory of Operation and Operating Procedures,* 11, http://www.optecinc.com

Stencel, R. 1999, *J. Amer. Assoc. Var. Star Obs.,* **27**, 61.

Skrutskie, M. F., *et al.* 2006, *The Two Micron All Sky Survey* (2MASS), *Astron. J.*, **131**, 1163.

van Belle, G. T., and Hart, A. 2007, private communication.

Table 1. A list of stars observed. PTI Target Stars and PTI Calibrator Stars from van Belle and Hart (2007), Near-IR Primary Standard Stars from Henden (2002).

Object Type[1]	HD	Spectral Type	J_{cat} / σ_{cat}	H_{cat} / σ_{cat}	Notes[2]
Standard	358	B8 IVmnp...	2.30 ±0.025	2.33 ±0.025	H, α And
Standard	886	B2 IV	3.50 ±0.26	3.64 ±0.20	2M, γ Peg
Standard	1013	M2 III	1.63 ±0.025	0.81 ±0.025	H, χ Peg
PTI Cal	1364	M3.5 IIIa	3.16 ±0.24	2.16 ±0.19	2M
PTI Cal	3268	F7 V	5.34 ±0.02	5.16 ±0.04	2M
Standard	6860	M0 III	−0.92 ±0.025	−1.73 ±0.025	H, β And
Standard	34085	B8 Iab:	0.23 ±0.025	0.22 ±0.025	H, Rigel
Standard	121370	G0 IV	1.71 ±0.025	1.41 ±0.025	H, η Boo
Standard	124897	K1 III	−2.21 ±0.025	−2.90 ±0.025	H, α Boo
Standard	128167	F3 Vwvar	3.70 ±0.025	3.51 ±0.025	H, σ Boo
PTI Target	133208	G8 IIIa	1.80 ±0.31	1.27 ±0.12	2M, β Boo
PTI Target	139153	M1.5 III	2.00 ±0.23	1.14 ±0.14	2M, μ CrB
PTI Cal	139761	K0	4.33 ±0.24	3.85 ±0.21	2M
PTI Cal	142908	F0 IV	4.69 ±0.037	4.48 ±0.036	3, λ CrB

Table 1. A list of stars observed. PTI Target Stars and PTI Calibrator Stars from van Belle and Hart (2007), Near-IR Primary Standard Stars from Henden (2002), cont.

Object Type[1]	HD	Spectral Type	J_{cat} / σ_{cat}	H_{cat} / σ_{cat}	Notes[2]
Standard	147394	B5 IV	4.20 ±0.025	4.27 ±0.025	H, τ Her
Standard	156014	M5 Ib	−2.29 ±0.025	−3.14 ±0.025	H, α Her
Standard	164136	F2 II	3.46 ±0.025	3.25 ±0.025	H, ν Her
PTI Cal	166229	K2.5 III	3.65 ±0.30	3.05 ±0.26	2M
PTI Target	168775	K2 III	2.58 ±0.28	1.99 ±0.16	2M, κ Lyr
PTI Cal	169702	A3 IVn	4.92 ±0.04	4.95 ±0.04	2M, μ Lyr
PTI Target	170970	M8+...	3.56 ±0.26	2.69 ±0.20	2M, V530 Lyr
Standard	172167	A0 V	0.00 ±0.025	0.00 ±0.025	H, Vega
PTI Cal	173417	F1 III–IV	4.90 ±0.04	4.84 ±0.04	2M
PTI Cal	174368	A0	8.46 ±0.03	8.43 ±0.03	2M
PTI Cal	184385	G5 V	5.57 ±0.02	5.25 ±0.04	2M
PTI Target	186675	G7 III	3.45 ±0.27	2.94 ±0.22	2M, 15 Cyg
PTI Target	186776	M4 III	2.72 ±0.25	1.85 ±0.20	2M, V973 Cyg
PTI Cal	187013	F7 V	4.05 ±0.3	3.98 ±0.3	2M
Standard	188947	K0 III	2.16 ±0.025	1.70 ±0.025	H, η Cyg
PTI Cal	190771	G5 IV	4.92 ±0.3	4.74 ±0.3	2M
PTI Target	192004	K3 Iab:	3.27 ±0.30	2.59 ±0.26	2M, 19 Vul
Standard	197345	A2 Iae	0.99 ±0.025	0.91 ±0.025	H, Deneb
Standard	197989	K0 III	0.73 ±0.025	0.19 ±0.025	H, ε Cyg
PTI Cal	200527	M4s...	2.27 ±0.33	1.41 ±0.18	2M, Vl981 Cyg
PTI Cal	200723	F3 IV	5.55 ±0.02	5.40 ±0.04	2M
PTI Target	205435	G8 III	2.49 ±0.26	2.01 ±0.26	2M, ρ Cyg
PTI Target	206330	M1 III	2.14 ±0.24	1.23 ±0.16	2M, 75 Cyg
PTI Cal	206749	M2 III	2.52 ±0.31	1.70 ±0.19	2M
Standard	217906	M2.5 II–III	−1.19 ±0.025	−2.05 ±0.025	H, β Peg
PTI Target	339034	K3 Iab:	3.25 ±0.27	2.14 ±0.22	2M, NR Vul

[1]*Targets and comps from van Belle and Hart (2007), Primary Standard Stars from Henden (2002).* [2]*H indicates that the magnitudes were taken from Henden (2002), and 2M indicates that the magnitudes were taken from the* 2Mass All Sky Catalog. *Where no uncertainty was given, a maximum value is assumed.* [3]*For HD 142908 (λ CrB), no 2Mass magnitudes were available, so we report our Table 3 result here.*

Table 2. Results for the near-IR primary standard stars.

HD	RJD*	Air Mass	$J_{inst} \pm \sigma_{inst}$	ΔJ	$H_{inst} \pm \sigma_{inst}$	ΔH
358	4334.8472	1.03	−8.17 ±0.003	10.47 ±0.025	−8.33 ±0.005	10.66 ±0.025
6860	4334.8819	1.02	−11.43 ±0.006	10.51 ±0.026	−12.42 ±0.006	10.69 ±0.026
121370	4270.6631	1.09	−8.74 ±0.003	10.45 ±0.025	−9.20 ±0.004	10.61 ±0.025
121370	4270.7326	1.23	−8.72 ±0.010	10.43 ±0.027	−9.16 ±0.003	10.57 ±0.025
121370	4271.6562	1.09	−8.73 ±0.005	10.44 ±0.025	−9.18 ±0.003	10.59 ±0.025
124897	4270.6458	1.08	−12.70 ±0.004	10.49 ±0.025	−13.57 ±0.005	10.67 ±0.025
124897	4270.7430	1.22	−12.67 ±0.030	10.46 ±0.039	−13.54 ±0.011	10.64 ±0.027
124897	4271.6319	1.08	−12.70 ±0.005	10.49 ±0.025	−13.57 ±0.005	10.67 ±0.025
124897	4271.6666	1.08	−12.68 ±0.005	10.47 ±0.025	−13.55 ±0.005	10.65 ±0.025
124897	4271.7708	1.36	−12.64 ±0.008	10.43 ±0.026	−13.51 ±0.011	10.61 ±0.027
128167	4271.6770	1.02	−6.68 ±0.001	10.38 ±0.025	−7.09 ±0.002	10.60 ±0.025
147394	4271.7256	1.01	−6.19 ±0.001	10.39 ±0.025	−6.35 ±0.003	10.62 ±0.025
147394	4272.7430	1.01	−6.17 ±0.003	10.37 ±0.025	−6.35 ±0.003	10.62 ±0.025
156014	4270.9027	1.40	−12.69 ±0.030	10.40 ±0.039	−13.80 ±0.013	10.66 ±0.028
156014	4271.6458	1.52	−12.66 ±0.010	10.37 ±0.027	−13.76 ±0.020	10.62 ±0.032
156014	4271.6944	1.22	−12.66 ±0.013	10.37 ±0.028	−13.77 ±0.011	10.63 ±0.027
156014	4271.7326	1.14	−12.69 ±0.005	10.40 ±0.025	−13.79 ±0.004	10.65 ±0.025
156014	4272.7604	1.11	−12.66 ±0.005	10.37 ±0.025	−13.75 ±0.009	10.61 ±0.027
156014	4335.6562	1.16	−12.77 ±0.009	10.48 ±0.027	−13.84 ±0.005	10.70 ±0.025
164136	4271.7430	1.07	−6.90 ±0.002	10.36 ±0.025	−7.35 ±0.003	10.60 ±0.025
164136	4272.7708	1.03	−6.86 ±0.002	10.32 ±0.025	−7.29 ±0.008	10.54 ±0.026
164136	4272.8055	1.02	−6.88 ±0.001	10.34 ±0.025	−7.33 ±0.002	10.58 ±0.025

(Table 2 continued on following pages)

Table 2. Results for the near-IR primary standard stars, cont.

HD	RJD*	Air Mass	$J_{inst} \pm \sigma_{inst}$	ΔJ	$H_{inst} \pm \sigma_{inst}$	ΔH
164136	4277.8159	1.03	−6.87 ±0.002	10.33 ±0.025	−7.33 ±0.002	10.58 ±0.025
164136	4290.7500	1.02	−6.83 ±0.005	10.29 ±0.025	−7.29 ±0.007	10.54 ±0.026
172167	4270.8819	1.02	−10.38 ±0.002	10.38 ±0.025	−10.60 ±0.005	10.60 ±0.025
172167	4271.7013	1.22	−10.34 ±0.001	10.34 ±0.025	−10.58 ±0.001	10.58 ±0.025
172167	4271.7812	1.03	−10.36 ±0.005	10.36 ±0.025	−10.59 ±0.006	10.59 ±0.026
172167	4271.8159	1.00	−10.38 ±0.006	10.38 ±0.026	−10.61 ±0.003	10.61 ±0.025
172167	4272.7916	1.01	−10.35 ±0.001	10.35 ±0.025	−10.58 ±0.004	10.58 ±0.025
172167	4277.8055	1.00	−10.36 ±0.002	10.36 ±0.025	−10.59 ±0.002	10.59 ±0.025
172167	4277.8437	1.02	−10.35 ±0.006	10.35 ±0.026	−10.58 ±0.005	10.58 ±0.025
172167	4277.8819	1.06	−10.32 ±0.016	10.32 ±0.030	−10.57 ±0.004	10.57 ±0.025
172167	4280.9062	1.14	−10.34 ±0.004	10.34 ±0.025	−10.56 ±0.006	10.56 ±0.026
172167	4290.7812	1.00	−10.33 ±0.004	10.33 ±0.025	−10.56 ±0.006	10.56 ±0.026
172167	4333.7083	1.02	−10.45 ±0.004	10.45 ±0.025	−10.67 ±0.002	10.67 ±0.025
172167	4333.7500	1.11	−10.45 ±0.003	10.45 ±0.025	−10.66 ±0.003	10.66 ±0.025
172167	4335.6944	1.02	−10.44 ±0.013	10.44 ±0.028	−10.67 ±0.008	10.67 ±0.026
172167	4335.7013	1.03	−10.44 ±0.005	10.44 ±0.025	−10.66 ±0.003	10.66 ±0.025
172167	4335.7152	1.05	−10.45 ±0.006	10.45 ±0.026	−10.67 ±0.013	10.67 ±0.028
172167	4335.7222	1.07	−10.44 ±0.004	10.44 ±0.025	−10.66 ±0.005	10.66 ±0.025
172167	4343.6875	1.04	−10.45 ±0.008	10.45 ±0.026	−10.66 ±0.006	10.66 ±0.026
172167	4343.7361	1.15	−10.41 ±0.007	10.41 ±0.026	−10.65 ±0.005	10.65 ±0.025
188947	4272.8159	1.06	−8.17 ±0.010	10.33 ±0.027	−8.87 ±0.006	10.57 ±0.026
188947	4272.8750	1.00	−8.20 ±0.003	10.36 ±0.025	−8.89 ±0.010	10.59 ±0.027

(Table 2 continued on following page)

Table 2. Results for the near-IR primary standard stars, cont.

HD	RJD*	Air Mass	$J_{inst} \pm \sigma_{inst}$	ΔJ	$H_{inst} \pm \sigma_{inst}$	ΔH
188947	4277.8888	1.01	−8.20 ±0.002	10.36 ±0.025	−8.89 ±0.003	10.59 ±0.025
188947	4277.9236	1.05	−8.18 ±0.006	10.34 ±0.026	−8.88 ±0.002	10.58 ±0.025
188947	4290.8437	1.01	−8.15 ±0.010	10.31 ±0.027	−8.85 ±0.005	10.55 ±0.025
188947	4291.8125	1.01	−8.17 ±0.002	10.33 ±0.025	−8.87 ±0.002	10.57 ±0.025
188947	4333.7916	1.07	−8.30 ±0.008	10.46 ±0.026	−8.97 ±0.007	10.57 ±0.026
188947	4335.7534	1.03	−8.30 ±0.003	10.46 ±0.025	−8.99 ±0.004	10.59 ±0.025
188947	4335.7673	1.05	−8.30 ±0.004	10.46 ±0.025	−8.99 ±0.006	10.59 ±0.026
197345	4272.8958	1.01	−9.39 ±0.004	10.38 ±0.025	−9.69 ±0.004	10.60 ±0.025
197345	4291.8750	1.01	−9.34 ±0.013	10.33 ±0.028	−9.65 ±0.007	10.56 ±0.026
197345	4333.8229	1.07	−9.50 ±0.006	10.49 ±0.026	−9.78 ±0.003	10.69 ±0.025
197345	4335.7708	1.02	−9.51 ±0.006	10.50 ±0.026	−9.79 ±0.005	10.70 ±0.025
197345	4335.7777	1.02	−9.50 ±0.003	10.49 ±0.025	−9.77 ±0.004	10.68 ±0.025
197345	4343.7138	1.00	−9.47 ±0.009	10.46 ±0.027	−9.76 ±0.002	10.67 ±0.025
197345	4343.7569	1.02	−9.49 ±0.004	10.48 ±0.025	−9.76 ±0.004	10.67 ±0.025
197345	4343.7812	1.05	−9.48 ±0.007	10.47 ±0.026	−9.76 ±0.002	10.67 ±0.025
197345	4343.8055	1.09	−9.47 ±0.010	10.46 ±0.027	−9.76 ±0.004	10.67 ±0.025
197989	4272.8854	1.01	−9.68 ±0.005	10.41 ±0.025	−10.40 ±0.004	10.59 ±0.025
197989	4291.9097	1.04	−9.66 ±0.005	10.39 ±0.025	−10.40 ±0.003	10.59 ±0.025
197989	4335.7812	1.02	−9.78 ±0.007	10.51 ±0.026	−10.50 ±0.005	10.69 ±0.025
217906	4333.9166	1.03	−11.74 ±0.004	10.55 ±0.025	−12.79 ±0.006	10.74 ±0.026
217906	4334.8090	1.03	−11.74 ±0.005	10.55 ±0.025	−12.78 ±0.009	10.73 ±0.027

*RJD = JD − 2,450,000

Table 3. Results for the PTI Target and PTI Calibrator stars.

HD	RJD*	$J_{inst} \pm \sigma_{inst}$	ΔJ	$J \pm \sigma J$	$H_{inst} \pm \sigma_{inst}$	ΔH	$H \pm \sigma H$
1364	4334.8611	−7.62 ±0.002	10.46 ±0.036	2.84 ±0.036	−8.64 ±0.002	10.66 ±0.036	2.02 ±0.036
3268	4334.8715	−5.08 ±0.001	10.41 ±0.036	5.33 ±0.036	−5.53 ±0.001	10.62 ±0.036	5.09 ±0.036
133208	4270.6806	−8.50 ±0.004	10.41 ±0.037	1.91 ±0.037	−9.11 ±0.042	10.60 ±0.036	1.49 ±0.055
133208	4271.6875	−8.49 ±0.006	10.38 ±0.038	1.89 ±0.038	−9.14 ±0.004	10.60 ±0.037	1.46 ±0.037
139153	4270.7014	−8.38 ±0.002	10.41 ±0.037	2.03 ±0.037	−9.42 ±0.004	10.60 ±0.036	1.18 ±0.036
139153	4271.7153	−8.38 ±0.005	10.38 ±0.036	2.00 ±0.036	−9.41 ±0.004	10.61 ±0.036	1.20 ±0.036
139761	4270.6909	−6.08 ±0.001	10.39 ±0.037	4.31 ±0.037	−6.82 ±0.003	10.57 ±0.036	3.75 ±0.036
139761	4270.7083	−6.08 ±0.001	10.39 ±0.037	4.31 ±0.037	−6.82 ±0.003	10.57 ±0.036	3.75 ±0.036
142908	4270.7153	−5.70 ±0.003	10.39 ±0.037	4.69 ±0.037	−6.08 ±0.002	10.56 ±0.036	4.48 ±0.036
166229	4270.7813	−6.82 ±0.001	10.40 ±0.046	3.58 ±0.046	−7.55 ±0.001	10.58 ±0.037	3.03 ±0.037
166229	4335.6875	−6.89 ±0.003	10.49 ±0.039	3.60 ±0.039	−7.62 ±0.004	10.69 ±0.037	3.07 ±0.037
166229	4335.6924	−6.89 ±0.004	10.49 ±0.039	3.60 ±0.039	−7.63 ±0.009	10.69 ±0.037	3.06 ±0.038
168775	4270.7881	−8.01 ±0.002	10.31 ±0.046	2.30 ±0.046	−8.76 ±0.003	10.55 ±0.037	1.79 ±0.037
168775	4271.7500	−8.02 ±0.005	10.41 ±0.036	2.39 ±0.037	−8.77 ±0.006	10.60 ±0.037	1.83 ±0.038
168775	4277.8299	−7.98 ±0.003	10.35 ±0.036	2.37 ±0.036	−8.73 ±0.006	10.58 ±0.036	1.85 ±0.036
168775	4290.7569	−7.95 ±0.001	10.21 ±0.036	2.26 ±0.036	−8.70 ±0.003	10.45 ±0.036	1.75 ±0.037
168775	4333.7222	−8.08 ±0.004	10.45 ±0.036	2.37 ±0.036	−8.80 ±0.006	10.66 ±0.036	1.86 ±0.036
168775	4335.7083	−8.07 ±0.009	10.48 ±0.036	2.41 ±0.037	−8.82 ±0.007	10.68 ±0.038	1.86 ±0.038
169702	4270.8056	−5.48 ±0.001	10.39 ±0.046	4.91 ±0.046	−5.74 ±0.001	10.56 ±0.037	4.82 ±0.037
169702	4271.7916	−5.47 ±0.001	10.36 ±0.036	4.89 ±0.036	−5.72 ±0.001	10.58 ±0.036	4.86 ±0.036
169702	4277.8542	−5.47 ±0.001	10.30 ±0.039	4.83 ±0.039	−5.74 ±0.001	10.44±0.036	4.70 ±0.036

(Table 3 continued on following pages)

Table 3. Results for the PTI Target and PTI Calibrator stars, cont.

HD	RJD*	$J_{inst} \pm \sigma_{inst}$	ΔJ	$J \pm \sigma J$	$H_{inst} \pm \sigma_{inst}$	ΔH	$H \pm \sigma H$
169702	4290.7917	−5.39 ±0.001	10.28 ±0.037	4.89 ±0.037	−5.63 ±0.002	10.53 ±0.036	4.90 ±0.036
170970	4270.7986	−6.87 ±0.001	10.40 ±.0.46	3.53 ±0.046	−7.90 ±0.024	10.58 ±0.037	2.68 ±0.044
170970	4271.7569	−6.89 ±0.002	10.37 ±0.036	3.48 ±0.036	−7.91 ±0.001	10.60 ±0.037	2.69 ±0.037
170970	4272.7847	−6.86 ±0.002	10.35 ±0.035	3.49 ±0.003	−7.89 ±0.004	10.58 ±0.036	2.69 ±0.037
170970	4277.8368	−6.85 ±0.002	10.32 ±0.036	3.47 ±0.036	−7.88 ±0.003	10.54 ±0.036	2.66 ±0.036
170970	4290.7708	−6.83 ±0.002	10.29 ±0.036	3.46 ±0.036	−7.86 ±0.004	10.54 ±0.036	2.68 ±0.037
170970	4333.7396	−6.96 ±0.003	10.43 ±0.036	3.47 ±0.036	−7.97 ±0.002	10.64 ±0.036	2.67 ±0.036
170970	4335.7083	−6.95 ±0.005	10.49 ±0.036	3.54 ±0.036	−7.97 ±0.016	10.69 ±0.038	2.72 ±0.041
170970	4343.6979	−6.94 ±0.012	10.56 ±0.037	3.62 ±0.039	−7.97 ±0.004	10.71 ±0.036	2.74 ±0.036
173417	4270.8368	−5.42 ±0.001	10.39 ±0.046	4.97 ±0.046	−5.80 ±0.001	10.56 ±0.037	4.76 ±0.037
173417	4271.8090	−5.40 ±0.002	10.36 ±0.036	4.96 ±0.036	−5.79 ±0.001	10.58 ±0.036	4.79 ±0.036
173417	4277.8750	−5.44 ±0.001	10.30 ±0.039	4.86 ±0.039	−5.79 ±0.002	10.44 ±0.036	4.65 ±0.036
173417	4291.7778	−5.36 ±0.002	10.44 ±0.037	5.08 ±0.037	−5.77 ±0.001	10.68 ±0.035	4.91 ±0.035
174368	4270.8159	−1.86 ±0.001	10.36 ±0.046	8.50 ±0.047	−2.15 ±0.001	10.51 ±0.037	8.36 ±0.037
184385	4343.7292	−4.83 ±0.002	10.64 ±0.037	5.81 ±0.037	−5.39 ±0.001	10.77 ±0.036	5.38 ±0.036
186675	4270.8472	−7.14 ±0.002	10.40 ±0.046	3.26 ±0.046	−7.80 ±0.007	10.58 ±0.037	2.78 ±0.038
186675	4272.8229	−7.09 ±0.004	10.35 ±0.037	3.26 ±0.037	−7.73 ±0.006	10.58 ±0.037	2.85 ±0.038
186675	4290.8125	−7.08 ±0.005	10.30 ±0.037	3.22 ±0.037	−7.74 ±0.003	10.54 ±0.036	2.80 ±0.036
186675	4291.7986	−7.07 ±0.003	10.39 ±0.038	3.32 ±0.038	−7.73 ±0.005	10.61 ±0.036	2.88 ±0.036
186675	4333.7674	−7.20 ±0.002	10.43 ±0.036	3.23 ±0.036	−7.84 ±0.001	10.64 ±0.036	2.80 ±0.036
186675	4335.7396	−7.21 ±0.003	10.49 ±0.036	3.28 ±0.036	−7.85 ±0.003	10.69 ±0.036	2.84 ±0.036

Table 3. Results for the PTI Target and PTI Calibrator stars, cont.

HD	RJD*	$J_{inst} \pm \sigma_{inst}$	ΔJ	J ± σJ	$H_{inst} \pm \sigma_{inst}$	ΔH	H ± σH
186675	4343.7014	−7.17 ±0.007	10.55 ±0.037	3.38 ±0.038	−7.82 ±0.004	10.72 ±0.036	2.90 ±0.036
186776	4270.8542	−7.85 ±0.002	10.40 ±0.046	2.55 ±0.046	−8.91 ±0.002	10.60 ±0.037	1.69 ±0.037
186776	4272.8333	−7.80 ±0.004	10.35 ±0.037	2.55 ±0.037	−8.86 ±0.005	10.58 ±0.037	1.72 ±0.038
186776	4277.9063	−7.79 ±0.004	10.33 ±0.036	2.54 ±0.036	−8.85 ±0.005	10.58 ±0.036	1.73 ±0.036
186776	4291.8194	−7.78 ±0.022	10.37 ±0.038	2.59 ±0.044	−8.84 ±0.009	10.58 ±0.036	1.74 ±0.037
186776	4333.7812	−7.93 ±0.003	10.45 ±0.036	2.52 ±0.036	−8.96 ±0.002	10.66 ±0.036	1.70 ±0.036
186776	4335.7431	−7.93 ±0.007	10.48 ±0.036	2.55 ±0.036	−8.97 ±0.005	10.68 ±0.036	1.71 ±0.036
186776	4343.7049	−7.89 ±0.007	10.53 ±0.037	2.64 ±0.038	−8.94 ±0.003	10.69 ±0.036	1.75 ±0.036
190771	4270.8681	−5.40 ±0.002	10.39 ±0.046	4.99 ±0.046	−5.90 ±0.002	10.56 ±0.037	4.66 ±0.037
190771	4277.9236	−5.35 ±0.002	10.30 ±0.036	4.95 ±0.036	−5.86 ±0.002	10.44 ±0.036	4.58 ±0.036
190771	4335.7604	−5.46 ±0.001	10.51 ±0.036	5.05 ±0.036	−5.96 ±0.001	10.69 ±0.036	4.73 ±0.036
192004	4272.8681	−7.21 ±0.002	10.35 ±0.037	3.14 ±0.037	−8.06 ±0.003	10.58 ±0.037	2.52 ±0.037
192004	4334.8125	−7.31 ±0.002	10.44 ±0.037	3.13 ±0.037	−8.14 ±0.002	10.65 ±0.036	2.51 ±0.036
192004	4335.7639	−7.31 ±0.004	10.49 ±0.036	3.18 ±0.036	−8.15 ±0.006	10.69 ±0.036	2.54 ±0.037
200527	4335.7917	−8.47 ±0.006	10.48 ±0.036	2.01 ±0.037	−9.51 ±0.008	10.68 ±0.036	1.17 ±0.037
200527	4343.7625	−8.43 ±0.005	10.51 ±0.036	2.08 ±0.037	−9.49 ±0.004	10.68 ±0.036	1.19 ±0.036
200723	4335.7951	−4.86 ±0.002	10.64 ±0.036	5.78 ±0.036	−5.28 ±0.001	10.70 ±0.036	5.42 ±0.036
205435	4272.9062	−7.92 ±0.005	10.35 ±0.036	2.43 ±0.036	−8.58 ±0.004	10.58 ±0.036	2.00 ±0.036
205435	4291.8889	−7.90 ±0.014	10.37 ±0.038	2.47 ±0.040	−8.56 ±0.004	10.59 ±0.036	2.03 ±0.036
205435	4335.7882	−8.04 ±0.006	10.48 ±0.036	2.44 ±0.037	−8.68 ±0.004	10.68 ±0.036	2.00 ±0.036
206330	4272.9132	−8.35 ±0.007	10.36 ±0.036	2.01 ±0.037	−9.34 ±0.006	10.58 ±0.036	1.24 ±0.036

(Table 3 continued on following page)

Table 3. Results for the PTI Target and PTI Calibrator stars, cont.

HD	RJD*	$J_{inst} \pm \sigma_{inst}$	ΔJ	$J \pm \sigma J$	$H_{inst} \pm \sigma_{inst}$	ΔH	$H \pm \sigma H$
206330	4291.9028	−8.35 ±0.002	10.36 ±0.038	2.01 ±0.038	−9.32 ±0.016	10.56 ±0.036	1.24 ±0.040
206330	4333.8646	−8.46 ±0.011	10.46 ±0.036	2.00 ±0.038	−9.43 ±0.005	10.67 ±0.036	1.24 ±0.036
206330	4335.7986	−8.46 ±0.010	10.48 ±0.036	2.02 ±0.038	−9.43 ±0.010	10.68 ±0.036	1.25 ±0.037
206749	4335.8035	−8.18 ±0.011	10.48 ±0.036	2.30 ±0.038	−9.16 ±0.007	10.68 ±0.036	1.52 ±0.037
206749	4343.7778	−8.16 ±0.004	10.52 ±0.036	2.36 ±0.036	−9.14 ±0.004	10.69 ±0.036	1.55 ±0.036
339034	4272.8611	−7.29 ±0.002	10.35 ±0.037	3.06 ±0.037	−8.43 ±0.001	10.58 ±0.037	2.15 ±0.037
339034	4291.8541	−7.27 ±0.002	10.39 ±0.038	3.12 ±0.038	−8.39 ±0.004	10.59 ±0.036	2.20 ±0.036
339034	4343.7083	−7.36 ±0.011	10.55 ±0.038	3.19 ±0.039	−8.47 ±0.001	10.70 ±0.036	2.23 ±0.036

*RJD = JD − 2,450,000

Abstracts of Papers Presented at the 96th Spring Meeting of the AAVSO, Held in Calgary, Alberta, Canada, June 26–July 3, 2007

Period Change Behavior of the Algol-type Eclipsing Binary LS Persei

Gary Billings
2320 Cherokee Drive NW, Calgary, Alberta T2L 0X7, Canada

Abstract   LS Persei is an Algol-type eclipsing binary, known to exhibit period change due to mass loss or transfer. Timings of its minima have been extended back to 1892 by archival observations in the Harvard College Observatory Photographic Plate Collection, and forward to 2007 by CCD observations. Over this interval, LS Per has undergone significant period decrease ($\Delta P/P = -\ 2.6 \times 10^{-4}$, $dP/dt = -2.0 \times 10^{-8}$). Small period changes are hard to document due to the relatively large uncertainty of minima timings from plates and visual observations, but recent, higher precision, CCD timings establish at least one small period increase ($\Delta P/P = +1.5 \times 10^{-5}$). The magnitude of this change, and the spectral type of the system, are compatible with the Applegate mechanism of periodic changes in the oblateness of the star which change the orbital period of the system. The ease with which high-precision minima timings can be obtained with a small telescope and CCD camera will allow early detection and close monitoring of future period changes

Long-Term Photometric Variability of 13 Bright Pulsating Red Giants

John R. Percy
Cristina O. Nasui
University of Toronto, Department of Astronomy, Erindale Campus, Mississauga, ON L5L 1C6, Canada

Gregory W. Henry
Tennessee State University, Center of Excellence in Information Systems, 3500 John A. Merritt Boulevard, Box 9501, Nashville, TN 37209

Abstract   Red giant stars cooler than 4000 K are unstable to pulsation; pulsating red giants make up ten per cent of all the bright stars. We have merged long-term (typically twenty years or more) photoelectric *V* photometry of thirteen bright pulsating red giants (TV Psc, EG And, RZ Ari, η Gem, V614 Mon, RS Cnc, VY UMa, FS Com, SW Vir, R Lyr, EU Del, V1070 Cyg, and W Cyg),

from a robotic telescope, and from the photoelectric photometry program of the American Association of Variable Star Observers (AAVSO), and analyzed each merged dataset using Fourier and self-correlation techniques. Several of the stars show two or more pulsation periods, and we have derived improved values of these. We have also derived improved values of the enigmatic long secondary periods which are present in several of the stars, and whose cause is unknown. Most of the stars also show very slow, small variations in amplitude and mean magnitude on time scales of thousands of days, whose cause is also unknown. We will also discuss, briefly, the nature and value of this project as an undergraduate research experience.

A Multicolor Photometric and Fourier Study of New Field RR Lyrae Variables

Michael Koppelman
University of Minnesota, Department of Astronomy, 116 Church Street SE, Minneapolis, MN 55455

Richard Huziak
127 Maple Street, Saskatoon, SK S7N 0A2, Canada

and

University of Saskatchewan Variable Star Research Group

Walter Cooney
1927 Fairview Drive, Port Allen, LA 70767

Vance Petriew
3 Noonan Road, Regina, SK S4V 0J5, Canada

Abstract   We present precision, multicolor light curves, new or updated ephemerides and Fourier components for four new or recently discovered RR Lyrae stars. We utilize $[Fe/H] - \phi - P$ relations to determine the metallicity, with separate relations for the RRab and RRc stars. Where possible we use a second method for determining $[Fe/H]$ such as the amplitude in the Johnson B bandpass (A_B). The metallicities are then used to calculate a second-order determination of the absolute magnitude (M_V) and hence the distance (D).

Research Breakthroughs From Pro-Am Collaborations

David G. Turner
Department of Astronomy and Physics, Saint Mary's University, Halifax, NS B3H 3C3, Canada

Abstract Professional-amateur collaborations are proving to be an exciting means of pursuing vital observing projects in areas where regular professional monitoring has declined or disappeared in recent decades. Such is the case for RT Aur, a bright Cepheid well established from a century of observation to exhibit a steady decrease in pulsation period. That is, until observations by AAVSO and Belarus observers revealed that it is actually undergoing a steady period increase superposed upon a sinusoidal trend! Or the case of a newly identified Cepheid variable with a smaller light amplitude than Polaris (!), studied with the aid of regular monitoring from RASC'er Dave Lane's automated backyard observatory. Other examples include an eclipsing system that is not what it was long thought to be, and other cases of an ongoing nature. In an era where large-scale surveys are dominating fields once covered by dozens of individual observers, there is a growing need for links with keen observers of every stripe to fill the "discovery void" occasioned by the benign neglect of professionals.

Slowly Pulsating B Stars: A Challenge for Photometrists

Robert J. Dukes, Jr.
Laney Mills
Melissa Sims
The College of Charleston, Department of Physics and Astronomy, Charleston, SC 29424

Abstract Slowly Pulsating B Stars (SPBs), which are mid- to late-B stars, are some of the most difficult of the bright pulsating variables to observe, are some in the most need of observation, and are some which would benefit greatly from being placed on a regular observing program by a single observer. They have characteristic periods on the order of 1–3 days with very small amplitudes (<0.03 magnitude in Stromgren *v*). These characteristics present the challenge and as well as an opportunity since there are very few groups currently observing these stars. While more rapid pulsators, such as the δ Scuti and β Cephei stars, benefit from multi- longitude campaigns the SPBs do not lend themselves to this type of approach because of their relatively long pulsation periods which require observations spanning months rather than weeks over several years to adequately describe. Our work with SPBs is supported by NSF grants.

One Little Telescope, So Many Stars

Jaymie Matthews
University of British Columbia, Department of Physics and Astronomy, 6224 Agricultural Road, Vancouver, BC V6T 1Z1, Canada

Abstract   This meeting coincides with a Canadian space astronomy milestone, marking four years that the MOST space telescope has been in orbit. In that time, MOST has more than lived up to its acronym by making major discoveries through ultraprecise photometry of the *M*icrovariability and *O*scillations of *ST*ars. Hundreds of stars. MOST has discovered new classes of pulsating stars among the hot massive B stars and nonradial oscillations in red giants which challenge theoretical expectations. By monitoring the acoustic beats of pre-main sequence stars, MOST is literally performing "ultrasound" on stellar embryos to test our models of star formation. MOST has measured the surface rotation profile of a young solar-type star, giving insights into what the magnetic field and spot activity of our own Sun may have been like when life first appeared on Earth. MOST asteroseismology of magnetic stars has resulted in the first direct tests of how magnetic fields interact with the stellar plasma, making such stars as magnetohydrodynamic laboratories. MOST measurements of the optical eclipse of an extrasolar planet lead to the albedo of a "hot Jupiter" and an understanding of its atmosphere, clouds, and even weather. MOST has begun the search for Earth-mass and -size planets around other stars. Not bad for a mission that was intended to last one year and study ten stars.

Suspected Variables in AAVSO Star Fields

Richard Huziak
127 Maple Street, Saskatoon, SK S7N 0A2, Canada

Abstract   The master listing of stars observed by the AAVSO is listed in the "Validation File". The file lists commonly observed variable stars but also lists many "obscure" stars within the fields of view that observers over the years have suspected of being variable. Over the century-long history of the AAVSO over 1,200 such suspects have been added, but this population has never been investigated in detail. Our project first identified each suspect with a catalogue name and position, then using CCD cameras we are now sorting out the true variables from non-variable stars. A small but significant percentage of these stars turn out to be variable, sometimes of surprisingly large range. Unfortunately, some of these variables have been used as comparison stars by visual observers over the years. And now with the fields being explored by CCD camera users, even small-range unrecognized variables stars can cause confusion and skewed data. It is thus important to identify the field suspects and eliminate them as comparison stars.

The AAVSO Standard Star Database (VSD) and the Variable Star Plotter (VSP)

Vance Petriew
3 Noonan Road, Regina, SK S4V 0J5, Canada

Michael Koppelman
University of Minnesota, Department of Astronomy, 116 Church Street SE, Minneapolis, MN 55455

Abstract   The AAVSO is refining its electronic chart plotting system in order to eliminate the manual task of creating paper-based charts. We will demonstrate the system, discuss the status and to-do list and show a technical peek into the inner-workings of the system.

Automated Variable Star Observing and Photometric Processing at the Abbey Ridge Observatory (ARO)

David J. Lane
P.O. Box 31013, Halifax, NS B3K 5T9, Canada

Abstract   In the second half of 2006, the author's backyard observatory began observing (mainly Cepheid) variable stars in collaboration with David Turner and Daniel Majaess of Saint Mary's University. This paper will describe the automated variable star observing and photometric processing software (Abbey Ridge Auto-Pilot and accompanying scripts) developed for and in use at Abey Ridge Observatory. This software completely automates observing the fields, taking calibration frames at night's end, calibrating the images, combining sequentially-taken images, astrometrically solving the images, and doing the aperture photometry of the selected stars. At the end of the night, the resulting calibrated images and EXCEL-compatible photometric data are automatically uploaded to an internet server and human-readable summary emails are sent to the observer. As input to the software, the observer provides two types of text files. The first type contains the list the fields to be observed on a given night. The second type is a simple database of information about the fields, including such things as: the equatorial coordinates of the field; the exposure details in each filter; the equatorial positions of the target, reference, and check stars; and the aperture photometry settings.

NOTES